TECHNISCHE
UNIVERSITÄT
DARMSTADT

Physik

Self-propulsion of Janus Particles near Polymer-Functionalized Substrates

Dem Fachbereich Physik
der Technischen Universität Darmstadt

zur Erlangung des Grades
eines Doktors der Naturwissenschaften (Dr. rer. nat.)

genehmigte Dissertation von
M. Sc. Mojdeh Heidari
aus Esfahan, Iran

Erstgutachterin: Prof. Dr. Regine von Klitzing
Zweitgutachterin: Prof. Dr. Annette Andrieu-Brunsen

Darmstadt 2021
D 17

Heidari, Mojdeh: Self-propulsion of Janus Particles near
Polymer-Functionalized Substrates
Darmstadt, Technische Universität Darmstadt
Jahr der Veröffentlichung der Dissertation auf TUprints: 2021
Tag der mündlichen Prüfung: 02.06.2021

Prüfungskommission:

Referentin: Prof. Dr. Regine von Klitzing
Korreferentin: Prof. Dr. Annette Andrieu-Brunsen
Prüfer: Prof. Dr. Thomas Halfmann
Prüfer: Prof. Dr. Benno Liebchen

Tag der wissenschaftlichen Aussprache: 02.06.2021

TECHNISCHE
UNIVERSITÄT
DARMSTADT

Physik

Erklärung gemäß §9 Promotionsordnung

Hiermit versichere ich, dass ich die vorliegende Dissertation selbstständig angefertigt und keine anderen als die angegebenen Quellen und Hilfsmittel verwendet habe. Alle wörtlichen und paraphrasierten Zitate wurden angemessen kenntlich gemacht. Die Arbeit hat bisher noch nicht zu Prüfungszwecken gedient.

_____

Datum und Unterschrift

To my Mum

Notice how each particle moves.
Notice how everyone has just arrived here from a journey.
Notice how each wants a different food.
Notice how the stars vanish as the sun comes up,
and how all streams stream toward the ocean.

Look at the chefs preparing special plates
for everyone, according to what they need.
Look at this cup that can hold the ocean.
Look at those who see the face.
Look through Shams'eyes
into the Water that is
entirely jewels.

–Rumi–

Acknowledgements

I would like to express my deepest gratitude to the people who helped and encouraged me during these years at TU Berlin and TU Darmstadt.

First of all, I would like to thank Prof. Dr. Regine von Klitzing for allowing me to do research in her group and providing invaluable and sincere guidance throughout this research. Apart from her continuous supervision and scholarly advice which helped me accomplish this task, I learned fairness and professionalism from her.

My cordial gratitude to Dr. Rene Straßnik not only because our birthdays matched, but also for his cheerful spirit and motivational talks during the time that my setup was "under construction". I deeply appreciate the valuable script that he wrote for my setup.

I would like to thank all my colleagues at TU Berlin and TU Darmstadt, especially those who moved from Berlin to Darmstadt. Despite the fact that "Ich hab noch einen Koffer in Berlin", this move made us closer to each other. Special thanks to all my dear officemates, Dr. Samantha Micciulla, Dr. Adrian Carl, Larissa Braun, Sandra Forg, Dr. Dikran Boyacian, and Franziska Jakob for the enjoyable scientific and non-scientific discussions. I would like to thank Sebastian Stock whose friendship and kind soul brightened up my days at work, Dr. Amin Rahimzadeh for all the pleasant chats on and off campus, and Dr. Hacer Yalcinkaya for all the mutual Persian/Turkish words that we used during our conversations which made it spectacular. You all have a special place in my heart.

My great appreciation to the Youtuber, Sydney Cummings, for her free online workout sessions and her inspirational words that helped me take care of me during the pandemic, physically and mentally.

I am wholeheartedly grateful to my parents and my siblings for their support and patience. There are no words that describe my gratitude to my mum, Mahshid. If I have achieved anything in my life it is all because of her.

Finally, I'm the most grateful to my dear husband, Sepehr, who simply is a pure joy to be around. His endless love and encouragement together with his sense of humor made the unbearable days bearable.

Abstract

This thesis presents the self-propulsion of Janus particles near the substrates functionalized with polymer brushes. The self-propulsion is based on self-thermophoresis which is a common mechanism to drive the autonomous motion of particles. Despite recent efforts to understand the mechanism governing the self-propulsion of thermophoretic particles, the interaction of particles with the substrate underneath the particle has remained unclear. However, the interfacial properties of the substrate/fluid interface might influence the interaction between the substrate and the particle, hence altering the particle velocity, orientation, etc. Therefore, it is crucial to achieve in-depth knowledge about the characteristics of the entire system to optimize the active motion of the particle.

In the first part of this thesis the impact of substrates with various wettabilities on the active motion of Au-PS Janus particles is analyzed: bare glass, POEGMA brush substrate, and hydrophobic glass. The results reveal that the slip length of the substrate has no significant impact on the particle velocity. In fact, the particle reaches its maximum velocity near the POEGMA brush substrate, which emphasizes the impact of the thermo-osmotic flow at the substrate and how it hinders the particle motion.

The second part of this thesis presents the impact of PNIPAM brush substrate on the active motion of the Janus particles and compares the results with the motion near a bare glass. Ellipsometry measurements display the thermo-responsiveness of the PNIPAM brush substrate, whereas combining atomic force microscopy and contact angle measurements allows to characterize the morphology, roughness, and wettability of the substrates. The results suggest an enhanced particle velocity near the PNIPAM-functionalized substrate which is governed by the no thermo-osmotic flow at the brush/water interface. This observation encouraged the synthesis of the PNIPAM brush with two different thicknesses. The higher velocity of the particle near the thin brush reveals an unprecedented impact of the brush thickness on the particle motion, where roughness and friction of the brush outermost layer come into play.

The third part is devoted to the self-propulsion of the Janus particle near POEGMA and PHEMA brush substrates with various thicknesses. Extensive characterization of the substrates enables a deeper understanding of the interfacial as well as mechanical properties of the substrates. The thermophoretic velocities exhibit a surprising behavior: particle velocity increases upon increasing the thickness of the brush until it reaches a maximum. However, further increasing the brush thickness leads to a decrease in particle velocity. This trend has been observed for both brush systems, which demonstrates an intrinsic dependence of the particle velocity on the flow boundary conditions and the thermo-osmotic slip at the brush/water interface.

Zusammenfassung

In dieser Arbeit wird die Fortbewegung von Janus-Partikeln in der Nähe von mit Polymerbürsten funktionalisierten Substraten vorgestellt. Der Selbstantrieb basiert auf der Selbst-Thermophorese, die ein häufig beobachteter Mechanismus ist, der die Fortbewegung der Partikel beschreibt. Trotz jüngster Bemühungen, den Mechanismus zu verstehen, der die Fortbewegung von thermophoretischen Partikeln steuert, bleibt die Wechselwirkung der Partikel mit dem Substrat unter dem Partikel ungeklärt. Die Grenzflächeneigenschaften der Substrat/Fluid-Grenzfläche könnten jedoch die Wechselwirkung zwischen dem Substrat und dem Partikel beeinflussen und somit unter anderem die Partikelgeschwindigkeit verändern. Daher ist es von entscheidender Bedeutung, ein tiefgehendes Wissen über die Eigenschaften des gesamten Systems zu erlangen, um die aktive Bewegung des Partikels zu optimieren.

Der erste Abschnitt dieser Arbeit beschäftigt sich mit Substraten mit verschiedenen Benetzbarkeiten und wie sie die aktive Bewegung von Au-PS Partikel beeinflussen: blankes Glas, POEGMA-Bürsten und hydrophobes Glas. Die Ergebnisse zeigen, dass die Slip-Länge des Substrats keinen signifikanten Einfluss auf die Partikelgeschwindigkeit hat. Tatsächlich erreichen Partikel ihre maximale Geschwindigkeit in der Nähe der POEGMA-Bürsten, was den Einfluss des thermo-osmotischen Flusses am Substrat und dessen Behinderung der Partikelbewegung betont.

Der zweite Abschnitt dieser Arbeit beschreibt den Einfluss der PNIPAM-Bürsten auf die aktive Bewegung von Janus-Partikel und vergleicht die Ergebnisse mit der Bewegung in der Nähe eines blanken Glases. Ellipsometrische Messungen zeigen die Thermoreaktivität der PNIPAM-Bürsten, während die Kombination von Rasterkraftmikroskopie und Kontaktwinkelmessungen eine Charakterisierung der Morphologie, Rauheit und Benetzbarkeit der Substrate ermöglicht. Die Ergebnisse deuten auf eine erhöhte Partikelgeschwindigkeit in der Nähe des PNIPAM-funktionalisierten Substrats hin, die durch den fehlenden thermo-osmotischen Fluss an der Bürsten/Wasser-Grenzfläche bedingt ist. Diese Beobachtung motivierte die Synthese der PNIPAM-Bürste mit zwei verschiedenen Dicken. Die höhere Geschwindigkeit der Partikel in der Nähe der dünnen Bürste zeigt einen bisher unbekannten Einfluss der Bürstendicke auf die Partikelbewegung, die durch Rauheit und Reibung der äußersten Bürstenschicht bestimmt wird.

Der dritte Abschnitt widmet sich der Fortbewegung der Janus-Partikel in der Nähe von POEGMA- und PHEMA-Bürsten mit unterschiedlichen Dicken. Eine umfangreiche Charakterisierung der Substrate ermöglicht ein tieferes Verständnis ihrer Grenzflächen- und der mechanischen Eigenschaften. Die thermophoretischen Geschwindigkeiten zeigen ein unerwartetes Verhalten: Die Partikelgeschwindigkeit nimmt mit zunehmender Bürstendicke zu bis sie ein Maximum erreicht. Eine weitere Zunahme der Bürstendicke führt jedoch zu einer Abnahme der Partikelgeschwindigkeit. Dieser Trend wurde für beide Bürstensysteme beobachtet, was eine intrinsische Abhängigkeit der Partikelgeschwindigkeit von den Strömungsrandbedingungen und dem thermo-osmotischen Schlupf an der Bürsten/Wasser-Grenzfläche demonstriert.

Contents

Chapter 1

Introduction

Movement on micro and nanoscale has been an intriguing yet mysterious topic for a very long time. Enzyme-based nanomotors undergo conformational changes to perform biological tasks.[1] They consist of a catalytic active region that sequentially opens up to bind to specific moieties, closes itself to let the reaction occur, and opens up itself again to release the product. Protein complexes as molecular motors[2,3] use chemical or potential energy and transduce it into physical, chemical, or mechanical forces to perform various tasks such as reproduction and cell differentiation. Microswimmers propel themselves autonomously at low Reynolds number regime, where viscosity dominates over inertia.

Nature hosts various types of biological microswimmers whose locomotion on a microscale has allowed them to search for food, fertilize and survive over the course of evolution. Flagellated bacteria,[4–6] sperm cells,[7–9] eukaryotic organisms,[10] certain algae,[11] as well as amoebae[12] and protozoa are some examples of biological microswimmers. Unicellular microorganisms such as sperm and Escherichia coli owe their propulsion to the synchronized motion of their single polar flagellum or several rotary flagella, respectively. The flagellum is attached to the rear end of the cell body and it generates a propulsive force and a torque that makes the bacterial cell body move and eventually rotate.[13]

Multicellular microorganisms such as Paramecium contain hair-like structures, the so-called cilia, all over their body, Figure 1.1. Cilia beat in two distinct fashion, power stroke and recovery stroke. The former is when the cilium is

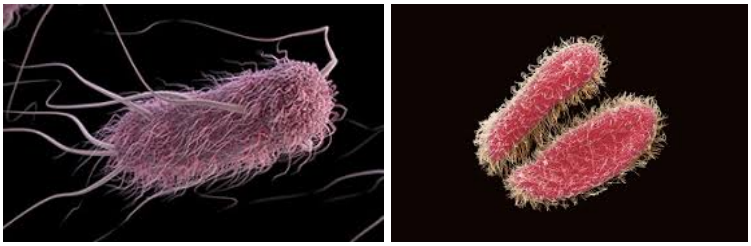

Figure 1.1: left) E.coli bacteria (adapted from www.cdc.gov), right) Paramecium (courtesy of Science Photo Library)

stretched out straight and it moves in one direction, whereas in the latter case cilium bends itself while it slowly retracts.[12,14]

Inspired by biological microswimmers, scientists started to build analogous artificial microswimmers at the beginning of the 21st century.[15] Ever since, this field has attracted significant attention in the last decade and extensive theoretical,[16,17] simulation,[18–20] and experimental[21–24] studies have been devoted to this ever-expanding field. These involve manufacturing active particles,[25–27] novel methods to induce the self-propulsion, and unraveling the mechanism behind the self-propulsion. This field holds promises for various applications such as cargo transport,[28–30] healthcare,[31–33] motion-based contaminant sensing,[34] and environmental remediation.[35]

A variety of active particles has been developed over the past decade based on different propulsion mechanisms such as self-diffusiophoresis,[36–38] light-driven diffusio-osmosis,[24,39] self-thermophoresis,[40–43] bubble propulsion,[44,45] biohybrid,[14,29,46,47] and self-acoustophoresis.[48]

Owing to their simplicity in design and preparation, Janus particles with at least one metal cap (platinum or gold) have been the most studied case in this field.[49–51] Janus particles are particles with two various hemispheres and they are named by Casagrande and de Gennes after the roman mythology god. Anisotropy of Janus particles has enabled them to generate an out-of-equilibrium condition around the particle under the right environment, which is a prerequisite requirement to induce self-propulsion.

Active colloidal particles are often tracked near a substrate and under partial confinement. This avoids the loss of particle observation into the 3rd dimension, hence particle tracking is achievable. However, the presence of a substrate is

likely to alter the dynamics of active particles[52–54]. The choice of the substrate as well as its cleaning procedure prior to the measurement could be the reason for the large discrepancies reported in the self-propulsion speeds of certain Janus particles.[36,55–57] Therefore, the aim of this thesis is to shed light on the active motion of self-thermophoretic particles in the close vicinity of a substrate functionalized with polymer brushes. This investigation could also provide a route to control the speed of microswimmers via the underlying substrate, which could be applied in the future e.g. to design complex motility landscapes by patterning substrates with polymer brushes.

This thesis is divided into three main parts. After giving a scientific background (Chapter 2) and introducing the experimental methods (Chapter 3), Chapter 4 focuses on the impact of surface wettability of the substrate on the velocity of Au-PS Janus particles with a diameter of 2.4 µm. It has been reported that increasing the slip length of the substrate would potentially increase the velocity of the particle. In that regard, three substrates with various hydrophilic properties were prepared, where the wetting of the substrates was evaluated using static contact angle measurements. This study highlights the role of the nanobubbles at the surface of the hydrophobic substrate and explains how it influences the particle velocity.

Chapter 5 explores the impact of poly(N-isopropylacrylamide) (PNIPAM)-functionalized substrate with various chain lengths on the active motion of Au-PS Janus particles with a diameter of 1 µm. Ellipsometry and X-ray reflectometry (XRR) were employed to determine the thickness of the brushes in air and water. The knowledge of the thermo-osmotic flow at the glass/water interface is the key to understand the velocity profile of the particle.

Chapter 6 presents the self-propulsion of the Au-PS Janus particles with a diameter of 2.4 µm near POEGMA and PHEMA brush substrates with various thicknesses. The physicochemical properties of the brush substrates are thoroughly investigated by using numerous methods. The effect of brush thickness, grafting density, as well as chemical structure on the self-propulsion of the particle are discussed. Furthermore, it is shown that small variations in the physicochemical properties of the brush substrate could alter the particle velocity accordingly.

Chapter 2

Scientific Background

2.1 State of the Art

2.1.1 Active particles

Active colloidal particles move autonomously by converting the energy of their environment into directed motion under out-of-equilibrium conditions.[58] Self-propulsion occurs in the low Reynolds number regime and it requires some sort of asymmetry in the particle's structure, surface functionalization, environment, etc. The energy can be injected into the system either by external fields, e.g. magnetic or electric fields or internally, e.g. by light, chemical reactions, etc. In the former situation, the external field exerts forces on the colloidal particle, whereas in the latter situation the generation of local force dipoles governs the self-propulsion. Phoretic transport mechanisms such as self-diffusiophoresis and self-thermophoresis belong to the internally driven active particles.

The first experimental realization of active microswimmers in bulk was conducted by Paxton *et al.* in 2004.[59] The Rod-shaped particles of platinum-gold (Pt-Au) move autonomously in aqueous hydrogen peroxide solutions by catalyzing the oxygen at the Pt end. The phoretic mechanism is based on **self-electrophoresis** which involves coupled reduction and oxidation of H_2O_2 at the surface of the swimmer. This causes an electric current through the swimmer which subsequently leads to the generation of a flux of protons around the

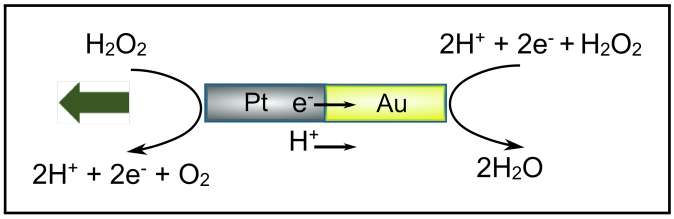

Figure 2.1: Schematic of the self-electrophoresis at bimetallic microswimmers

swimmer.[60,61] As a result, the swimmer moves with its oxidizing head forward, Figure 2.1.

Later in 2007, dielectric colloidal particles half-coated with Pt were introduced by Howse *et al.*[55] The self-propulsion of these particles is goverend by the **self-diffusiophoresis**. This relies on the decomposition of hydrogen peroxide at one side of the particle (often Platinum) which leads to the generation of oxygen bubbles at that side. As a result, a concentration gradient along the surface of the particle is generated which makes the particle self-propel.[62–64] Downsizing the particle to micrometer range has led to the disappearance of oxygen bubbles, despite the self-propulsion. Therefore, the origin of self-diffusiophoresis is still a controversial topic.

The focus of this thesis is on **self-thermophoretic** microswimmers. Janus particles of polystyrene particles half-coated with gold (Au-PS) could be potentially exploited to generate self-thermophoretic propulsion.[40,65] When a Au-PS particle gets illuminated with laser light (λ=532 nm), heat will be generated only at the gold side of the particle due to the surface plasmon excitation of the gold cap. As a result, a local temperature gradient is generated along the surface of the particle which perturbs the equilibrium conditions in the surrounding medium and finally leads to particle self-propulsion, Figure 2.2.[16]

Although self-diffusiophoretic mechanism is the most studied case in the field of synthetic microswimmers, it has a few disadvantages. It mostly relies on the catalytic decomposition of invasive hydrogen peroxide, which limits their application in biological fields. Self-propulsion stops as well when the fuel is consumed. However, in the case of self-thermophoresis, the particle is propelled via conversion of light into heat and the active motion can be switched on and off on demand.

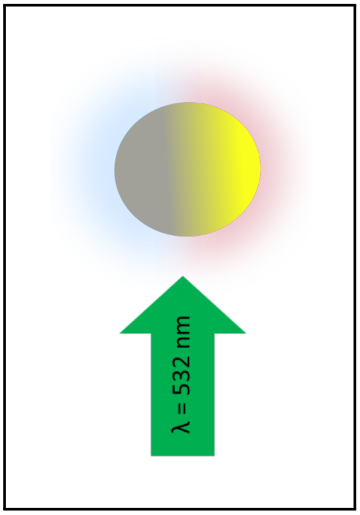

Figure 2.2: Temperature gradient along the surface of the particle generated due to the Plasmon resonance excitation of the gold cap

A novel method is introduced by Qian *et al.* to steer individual thermophoretic Janus particles .[20] The "photon nudging" method utilizes rotational random walks to reorient the Janus particle and the self-propulsion is turned on only when the swimmer has the correct orientation towards its target. This method enhances the directed motion of self-propelled particles in the lab frame and it can be achieved by the optically switchable photophoretic propulsion mechanism in combination with a feedback control system. Photon nudging is further employed by Bregulla *et al.* to navigate Au-PS particles of different sizes.[22]

Self-thermophoresis is not restricted only to Janus particles. Landin *et al.* proposes a mechanism in which gold nanoparticle coated melamine resin particles self-propel upon laser illumination.[42] However, the whole particle is not illuminated with light, but rather only a small part of the particle interacts with it. Therefore, an asymmetric temperature gradient is generated at the surface of the particle which leads to its self-propulsion.

Self-thermophoresis requires sufficiently strong laser intensity. Gomez-Solano *et al.* unveiled a novel method to induce self-propulsion using low laser intensities.[21,66] They experimentally investigated the dynamics of silica particles half coated with carbon in a viscoelastic fluid. The particles are suspended in a binary mixture of water and propylene glycol propyl ether (PnP), with the

lower critical point of $31.9°$C. 0.05% poly-acrylamide (PAAm) is added to the mixture to make it viscoelastic. The suspension is illuminated with light which leads to demixing of the fluid at the particle surface. Thus, the self-propulsion is governed by the local concentration gradient which causes a self-diffusiophoretic motion.

The generated flow field around a self-thermophoretic active particle has been the subject of numerous theoretical studies. Bickel *et al.* studied the flow pattern in the vicinity of a heated metal-capped Janus particle.[67] They discovered that if the thickness of the cap exceeds 10 nm, the cap forms an isotherm and the flow pattern comprises a quadrupolar term which decays with the square of the inverse distance $\sim r^{-2}$.

2.1.2 Self-propulsion near walls

In most of the above-mentioned examples, the motion of active colloids has been studied under partial confinement near a glass substrate in 2 dimensions.[37] The theoretical literature of self-propelling particles near walls is rather rich and mainly based on catalytically active particles near charged substrates. Whereas, only a few experimental studies have taken the influence of the substrate into account. The following sections review the recent theoretical and experimental studies in that regard.

Theoretical studies

The dynamics of a self-propelled Janus particle near a wall is studied by Ibrahim and Liverpool.[53] They introduce a mechanism called "wall-induced-diffusiophoresis" which is the result of wall impermeability to the solute molecules. This mechanism governs the migration of particles either towards or away from the nearby planar wall depending on whether the swimmer is a global source or sink. They categorize swimmers in two classes: *inert-face-forward* and *active-face-forward*. In the former case, the swimmers achieve an enhanced parallel propulsion along the wall before they are scattered away due to a combination of hydrodynamic repulsion and wall-induced-diffusiophoresis. The latter deals with swimmers which are strongly attracted to the wall.

In a study by Uspal *et al.* self-propulsion of a catalitically active particle near a planar wall is further refined.[68] They demonstrate that the dynamics of an active particle can be altered by varying certain particle design parameters such as the proportion of catalyst coverage, and the attractive or repulsive character of the solute-particle interactions. In particular, the particle slides along the wall at a fixed height and orientation, when the particle exhibit high catalyst coverage and identical repulsive interactions. However, at very high catalyst coverage and repulsive interactions, the particle reaches a stable hovering state in which it acts as a stationary micropump. Their developed quantitative model elucidates the physical mechanisms governing these steady states.

Chiang *et al.* showed that the interactions between a bimetallic colloidal motor and a nearby wall generate a localized electroosmotic (LEO) flow underneath the particle, i.e. along the substrate, which could significantly alter the speed of the particle.[69] According to their developed model, particle velocity slows down once it moves near a wall that has a zeta potential with the same sign as the particle.

Experimental studies

Ketzetzi *et al.* recently reported that the diffusiophoretic velocity of a catalytic colloidal swimmer is influenced by the hydrodynamic slip at the wall.[70] Their findings indicate that the propulsion speed of the particle increases with increasing the slip length and hydrophobicity of the substrate. These experimental findings prove that the impact of the substrate is non-negligible.

The motion of patchy active particles near a wall was studied by Jalilvand *et al.*[71] They demonstrated that the self-propelled activity of the particles can be tailored by varying the size of the active area. Moreover, it was shown that the vicinity of a solid boundary leads to preferential rotational motion of the particles around their swimming axis. This is explained by the distortion of the solute gradient near the wall that alters the hydrodynamic interactions between the particle and the wall. Hence, particle reorientation occurs.

The important impact of the substrate on the velocity of bimetallic catalytic motors has been further demonstrated by Wei *et al.*, where the role of surface charges, released ions, and morphology was examined extensively.[72] The glass substrates were functionalized with negatively and positively charged

polyelectrolyte multilayers (PEMs) and the dynamics of the bimetallic microrods near the modified substrates were studied. It turned out that upon increasing the number of bilayers, particle velocity decreases substantially. Such a decrease in velocity is assumed to originate from the ions which diffuse out of the PEMs into the solution and contribute to the electroosmotic flow at the substrate, which in turn reduces the particle velocity.

A study by Wang *et al.* revealed that the efficiency of bimetallic catalytic nanorod motors increases by 60% upon coating the glass substrate with polyethyleneglycol (PEG).[30] This finding was attributed to the reduced charge density of the wall upon modification.

Despite the numerous theoretical and experimental studies focusing on the influence of walls and confinements on the active motion of catalytic particles,[68,70,73,74] only little is known about the interactions between thermophoretic particles and nearby walls.

In an experimental study combined with analytical theory and numerical calculations, Bregulla *et al.* investigated the velocity field caused by thermo-osmotic flow due to a heated gold nanoparticle fixed at the surface of a glass/pluronic-coated glass.[75] They discovered that the slip velocities tend to be much stronger at interfaces covered with nonionic block copolymers compared to charged glass. Therefore, the particle velocity is enhanced near the pluronic-coated substrate.

In the present thesis the substrates are functionalized with polymer brushes. Polymer brushes are promising candidates to tailor the physicochemical properties of the substrates[76,77] such as surface free energy, surface charges, wettability, stiffness, topography, responsiveness to external stimuli, etc. Thanks to their exquisite anti-biofouling and lubrication properties,[78,79] they serve as a useful strategy for self-propel measurements as they reduce the interfacial drag.[80,81] Such properties underlie the numerous application of polymer brushes over the past few decades, especially in the fabrication of microfluidic devices.[82,83]

2.2 Theoretical Background

2.2.1 Passive Brownian motion

Diffusion, known as the transport phenomenon, is a physical phenomenon that describes the tendency of two or more substances to reach an equilibrium. Diffusion occurs in all states of matter and it plays a significant role in chemical, physical, and biochemical processes. Fick's law provides a macroscopic description of diffusion.[84] It relates the macroscopic diffusion flux $\boldsymbol{J}$ to the local concentration gradient $\nabla c(\mathbf{x}, t)$:

$$\boldsymbol{J} = -D\nabla c(\mathbf{x}, t) \tag{2.1}$$

where D is the diffusion coefficient of the solute. The solute molecules migrate from regions of higher concentration to regions of lower concentration. In 1827 the British botanist Robert Brown discovered the erratic motion by observing a random motion of small pollen grains of the Clarkia Pulchella plant suspended in water under a microscope. In 1905 Albert Einstein[85] considered the particle movement observed by Brown[86] and he showed that it can be described by a diffusion coefficient of a Brownian particle, assuming the movement is temporally and spatially homogeneous:[87]

$$D = \frac{k_{\mathrm{B}}T}{f} \tag{2.2}$$

where k_{B} is the Boltzmann constant, T is the ambient temperature, and f is the friction coefficient. The friction coefficient describes the linear response $\mathbf{u}$ to an applied external force $\mathbf{f}$, $\mathbf{u} = \mathbf{f}/f$. The friction coefficient is generated by the random collision of particles with solvent molecules which leads to thermal fluctuations. The friction coefficient of a random particle with radius R, suspended in an incompressible fluid can be obtained by considering the Navier-Stokes-equation[88]

$$\rho\left(\frac{\partial \mathbf{v}}{\partial t} + (\mathbf{v}.\nabla)\mathbf{v}\right) = -\nabla p + \eta\nabla^2\mathbf{v} + \mathbf{f} \tag{2.3}$$

where ρ is the fluid density, **v** the position- and time-dependent fluid velocity, p the hydrostatic pressure, η the dynamic viscosity of the fluid, and **f** the external body force. The first term on the left-hand side is the driving pressure gradient, and $\eta\nabla^2\mathbf{v}$ is the viscous dissipation. The first term on the right-hand side corresponds to the time-dependent inertial component, whereas the second term is the non-linear inertial term.

Scaling the various terms in the equation using characteristic length L and characteristic velocity υ and considering the stationary case where no volume forces act on the liquid,

- $\mathbf{v} \propto \upsilon$
- $\nabla \propto 1/L$
- $t \propto L/\upsilon$

Implies the following to the Navier-Stokes equation:

- The viscous term is proportional to $\eta\upsilon/L^2$
- Non-linear inertia and unsteady inertia is of the order of υ^2/L

Therefore, the ratio of inertial terms to viscous terms is

$$Re = \frac{\rho\upsilon L}{\eta} \tag{2.4}$$

where Re is the Reynolds number. The Stokes equation can be obtained by further simplifying the Navier-Stokes equation by omitting the inertial term $\rho(\mathbf{v}.\nabla\mathbf{v}) = 0$. It describes the situation where inertia no longer plays a role and viscous forces dominate.

$$\nabla p - \eta\nabla^2\mathrm{v} = \mathbf{f}. \tag{2.5}$$

The Stokes equation and low Reynolds number regime have exquisite properties which will be discussed in section 2.2.2.

The friction coefficient for the translational displacement of a sphere with radius *R* in the low *Re* number regime is called the Stokes coefficient and is

$$f_{\mathrm{Stokes}} = 6\pi\eta R. \tag{2.6}$$

As a result, the translational diffusion coefficient of a particle undergoing a Brownian motion is the so-called Stokes-Einstein relation:

$$D = \frac{k_{\mathrm{B}}T}{6\pi\eta R}. \tag{2.7}$$

The rotational diffusion coefficient D_{R} can be obtained through the Debye-Stokes-Einstein equation, where D_{R} is related to the rotational friction coefficient f_{R}. For a spherical particle under the no-slip boundary condition $f_{\mathrm{R}} = 8\pi\eta R^3$. Therefore,

$$D_{\mathrm{R}} = \frac{k_{\mathrm{B}}T}{8\pi\eta R^3}. \tag{2.8}$$

The rotational timescale τ_{R} is the inverse of the rotational diffusion coefficient and that is the time a spherical particle needs to rotate and change its orientation.

$$\tau_{\mathrm{R}} = \frac{8\pi\eta R^3}{k_{\mathrm{B}}T}. \tag{2.9}$$

Translational and rotational diffusions are the results of the collision of the suspended particle with the fluid molecules, which exerts a torque on the particle and disturbs its motion. Overdamped Langevin equation describes the translational dynamics of a particle suspended in a fluid, where inertia is negligible:[89]

$$\mathbf{F}_{\mathrm{th}} = -f_{\mathrm{t}}\mathbf{v}. \tag{2.10}$$

$\mathbf{F}_{\mathrm{th}}$ is the stochastic thermal force and $-f_{\mathrm{t}}\mathbf{v}$ is the viscous friction force. Langevin equation can be rewritten as

$$d\mathbf{r} = \sqrt{2D}d\mathbf{W} \tag{2.11}$$

where $d\mathbf{W}$ is the derivative of a Wiener process, with zero average and variance 1. Equation (2.11) in 2D can be written as:

$$\begin{cases} \Delta x = \sqrt{2D\Delta t}W_{\mathrm{x}} \\ \Delta y = \sqrt{2D\Delta t}W_{\mathrm{y}}. \end{cases} \tag{2.12}$$

Mean square displacement *MSD*, an important parameter for characterizing the

motion of particles in 2D can be calculated as follows:

$$MSD = \Delta x^2 + \Delta y^2 = 4D\Delta t. \tag{2.13}$$

2.2.2 Low Reynolds number

Microorganisms and bacteria live in a fluid environment where the viscous forces that they experience are many orders of magnitude stronger than the inertial forces. Their motility is due to the low Reynolds number regime, where the flow of the fluid is always laminar. A bacterium swimming at $0.01\mathrm{mms}^{-1}$ has the Reynolds number of 10^{-5} ($Re \ll 1$), whereas a whale swimming at $10\,\mathrm{ms}^{-1}$ has the $Re = 3 \times 10^8$. The low Re number regime enables the bacteria to stop instantaneously. Whereas the whale would "coast" for a while after it decides to stop swimming since the inertial effect dominate.

The Stokes equation describes the low Reynolds number regime, however, it has some consequences which were stated by Edward M. Purcell in 1976 in a paper called "Life at low Reynolds number".[90] Stokes equation has the following properties:

- Linear: Stokes flow is proportional to the applied force.
- Instantaneous: The fluid has no memory of the boundary condition in the past and the current flow is dominated by the present boundary conditions.
- Time-reversible: Under time-varying boundary conditions, the flow will get back to its original condition, if the opposite boundary conditions apply.

Time-reversibility is the major drawback of the Stokes equation. If a microorganism displays a reciprocal motion, where its forward stroke is identical to its backward stroke, it will end up again at the starting point, the so-called "Scallop theorem" stated by Purcell. A scallop cannot propel itself forward by only opening and closing its two shells.

To overcome the problem imposed by time-reversibility, the motion has to be non-reciprocal. Microorganisms break the time-reversed symmetry by asymmetrical flagellar motion, rotating helices, cilia's oar-like beats, etc.

Inspired by nature, various strategies have been applied to generate synthetic microswimmers. To break the reciprocity, the microswimmer displays either an asymmetry in its structure or the asymmetry is imposed by the fluid surrounding it, which drives the microswimmer to an out-of-equilibrium condition. Three linked spheres[91] and phoretic Janus particles[92] are a few examples of synthetic microswimmers.

2.2.3 Active Brownian motion

In contrast to passive Brownian motion, active Brownian motion enables the synthetic microswimmers to undergo a directed motion. An active particle takes the energy of its environmental conditions and converts it into directed motion under non-equilibrium conditions. Considering the particle at position *x*,*y*, and orientation θ, dynamics of an active colloid can be obtained as follows,[93,94]

$$\begin{cases} \dot{x} = v\cos\theta + \sqrt{2D_{\mathrm{T}}}\varsigma_{\mathrm{x}} \\ \dot{y} = v\sin\theta + \sqrt{2D_{\mathrm{T}}}\varsigma_{\mathrm{y}} \\ \dot{\theta} = \sqrt{2D_{\mathrm{T}}}\varsigma_{\theta} \end{cases} \tag{2.14}$$

where ς_x,ς_y and ς_θ are white Gaussian noise with zero mean and correlation $\delta(t)$. To gain more insights about the dynamics of an active particle in 2D, *MSD* can be calculated:[55]

$$MSD = \Delta r^2 = \langle (r_{\mathrm{t}} - r_0)^2 \rangle = 4Dt + \frac{\tau_{\mathrm{R}}^2 v^2}{2}\left[\frac{2t}{\tau_{\mathrm{R}}} + exp(-\frac{2t}{\tau_{\mathrm{R}}}) - 1\right] \tag{2.15}$$

which implies:

$$\begin{cases} MSD = 4Dt + t^2v^2 & t \ll \tau_{\mathrm{R}} \\ MSD = t(4D + v^2\tau_{\mathrm{R}}) & t \gg \tau_{\mathrm{R}}. \end{cases} \tag{2.16}$$

It indicates that for time scale well below the rotational diffusion time, the particle expresses a ballistic motion, whereas, at $t \gg \tau_{\mathrm{r}}$ the motion of particle displays an enhanced diffusive behavior as the translational diffusion time randomizes the direction of the particle over long times. Therefore, the effective

translational diffusion coefficient can be defined as:

$$D_{eff} = D + \frac{v^2 \tau_{\mathrm{R}}}{4}. \tag{2.17}$$

2.2.4 Phoretic motion

Several methods have been applied to generate an active Brownian motion. Mechanical deformation of the particle's body has been the most conventional case. Phoretic transport is a new generation of microswimmers which is the movement of colloidal particles by a field that interacts with the surface of the particle. This method deploys the surface flow generated by a gradient of temperature, concentration, or electrical potential.[95] The surface flow or the slip velocity across the interface is generated within the interfacial layer between the surface of the particle and the fluid. The interplay among surface chemistry, charge, fluid dynamics, and thermal energy influences the phoretic transport of the microswimmers.

When a particle moves due to a temperature gradient, this mechanism is called **thermophoresis**. The drift velocity is proportional to the applied temperature gradient:[96]

$$\mathbf{u} = -D_{\mathrm{T}} \nabla T \tag{2.18}$$

where D_{T} is the thermodiffusion coefficient and ∇T is the temperature gradient. D_{T} depends on the temperature and the electrolyte composition, where the thermoelectric field of the electrolyte solution often determines its sign and magnitude. Mass flux which is the result of such motion can be calculated as follows:[97]

$$\mathrm{J} = -D \nabla c - c D_{\mathrm{T}} \nabla T \tag{2.19}$$

where ∇c is the concentration gradient resulted by the mass flux. For a closed system at stationary state $\mathrm{J} = 0$, a uniform thermal gradient along z is formed:

$$\frac{dc}{dz} = -c S_{\mathrm{T}} \frac{dT}{dz} \tag{2.20}$$

where $S_{\mathrm{T}} = \frac{D_{\mathrm{T}}}{D}$ is the so-called Soret coefficient. The particle moves to the cold when $S_{\mathrm{T}} > 0$ and moves to the hot when $S_{\mathrm{T}} < 0$. The gradient could also be generated by the particle itself rather than being imposed by an external

force, this phenomenon is called self-phoresis. Self-phoresis often involves Janus particles, particles with two different hemispheres with various properties, along the surface of which the gradient is formed.

To understand the propulsion of thermophoretic particles systematically, it is important to gain a deeper insight into the interfacial interactions between the particle and the fluid. The boundary layer is defined as the layer at the particle/fluid interface within which the interfacial excess enthalpy decays to zero. Parameters such as surface chemistry and fluid type could influence the interfacial excess enthalpy. The temperature gradient across the particle surface could modify the interfacial layer and induces a surface slip velocity, v_{s}, which saturates at the interaction length B, Figure 2.3. The following section is devoted to the hydrodynamics within the boundary layer.

Boundary layer hydrodynamics

The boundary conditions are not negligible when a solid-fluid interface exists. At a microscopic scale, the slip is defined as the weak adherence of the solvent to the solid surface. As explained earlier, such a slip enhances the externally driven transport, therefore investigating the slip at the solid surface is of great importance. Naviers boundary condition relates the shear stress Σ_0 and the resulting slip velocity v_0:[43]

$$\eta v_0 = b\Sigma_0 \tag{2.21}$$

where η is the fluid viscosity and b is the material-specific constant or the so-called slip length. Figure 2.3 illustrates the fluid velocity field in the boundary layer with thickness B close to a particle with radius a. Such particle exerts an effective force density f_{x} on the surrounding fluid including the excess hydrostatic pressure. This pressure is finite close to the particle surface and vanishes at B. The boundary velocity v_{B} is the sum of the intrinsic slip velocity v_0 and the velocity change within the boundary layer Δv. The intrinsic velocity emerges when the fluid molecules do not fully adhere to the particle. Apparent slip or Δv arises by the surface forces on the fluid in the boundary layer.[43]

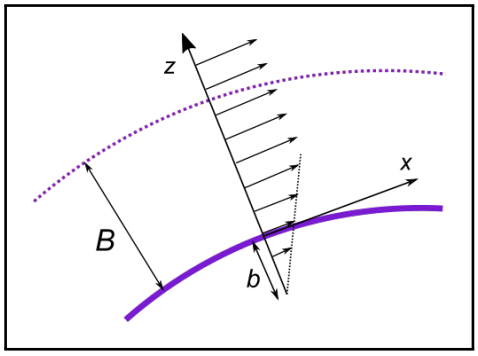

Figure 2.3: Schematic view of the fluid velocity field in the boundary layer close to a particle

$$v_{\mathrm{B}} = v_0 + \frac{1}{\eta}\int_0^B z f_{\mathrm{x}} \mathrm{d}z \equiv v_0 + \Delta v \tag{2.22}$$

Beyond the boundary layer, the normal and tangential components of the fluid flow vary as $v_r \propto [1 - ((\frac{a+B}{r}))^3]$ and

$$v_t = v_{\mathrm{B}} \left(\frac{2}{3} + \frac{(a+B)^3}{3r^3} \right). \tag{2.23}$$

As the normal velocity vanishes at $r = a + B$, the stress at the outer side of the boundary layer is

$$\Sigma_{\mathrm{B}} = -\frac{2\eta v_{\mathrm{B}}}{a}. \tag{2.24}$$

Considering equations (2.24) and (2.25), the boundary velocity can be rewritten as:

$$v_{\mathrm{B}} = \frac{\Delta v + b\Delta\Sigma/\eta}{1 + 2b/a}. \tag{2.25}$$

Upon transferring to the laboratory frame where the particle is mobile, the velocity of the particle is:[98]

$$u = -\frac{2}{3}\bar{v}_{\mathrm{B}}. \tag{2.26}$$

Thus, the speed of the fluid at the interface which moves in the opposite direction is $\frac{1}{3}\bar{v}_{\mathrm{B}}$. When the slip velocity v_s is generated by the temperature gradient, this could be also called thermo-osmotic velocity and it can be calculated by:[99]

$$v_s(r) = -\frac{1}{\eta}\int_0^\infty z\, h(z) \frac{\nabla T}{T} \mathrm{d}z = \mu(\mathrm{r})\nabla T \tag{2.27}$$

where $\mu(r)$ is defined as the mobility parameter.

The generated slip flow at the particle surface leads to a thermophoretic drift velocity in the opposite direction. The thermophoretic velocity is related to the slip velocity and can be obtained by[16]

$$v_{\mathrm{th}} = -\frac{1}{S}\int v_{\mathrm{s}}\mathrm{d}S = -\frac{1}{S}\int \mu(\mathrm{r})\nabla T\mathrm{d}S \tag{2.28}$$

where S is the particle surface.

Double layer forces of charged colloids

When a charged surface comes into contact with an electrolyte solution, it gives rise to attraction, repulsion, and subsequent accumulation of ions at the interface. This consists of two distinct regions.[100] First, the Stern layer is where the counter ions are attracted to the interface and form a compact and immobilized layer with a thickness of less than a nanometer.[101] The random thermal motion of the ions together with the electrostatic interactions between counter ions attracted towards the substrate and co ions repelled from it leads to the formation of the second layer, the so-called electrical double layer (EDL). Zeta potential is the potential at the shear plane, where the shear plane is assumed to be between Stern layer and Debye length, Figure 2.4.

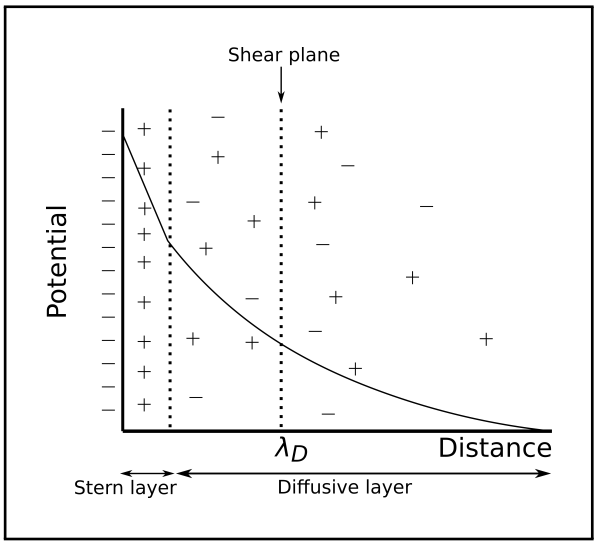

Figure 2.4: Electrostatic potential near a negatively charged surface

Thermophoresis measurements of colloidal particles are often carried out in aqueous solutions. These particles carry the charge density of $e\sigma$, which gives rise to the accumulation of mobile counterions available in the solution at the particle/water interface.[98] The Poisson-Boltzmann mean-field approximation describes the excess amount of monovalent ions within the electric double layer at the interface:

$$n_{\pm} = n_0 \left(e^{\mp \frac{e\psi}{k_{\mathrm{B}}T}} - 1 \right) \tag{2.29}$$

where n_0 is the bulk salinity and ψ is the electrostatic potential.

The charge density and the excess density of mobile ions n within the electric double layer are as follows:

$$\rho = e(n_+ - n_-), n = n_+ + n_-. \tag{2.30}$$

These quantities decay exponentially at larger distances, on a scale given by the Debye length

$$\lambda = (8\pi n_0 l_{\mathrm{B}})^{-0.5} \tag{2.31}$$

where l_{B} is the Bjerrum length, $l_{\mathrm{B}} = e^2/4\pi\varepsilon k_{\mathrm{B}}T$ and ε is the solvent permittivity.

In thermophoresis, the temperature gradient breaks the spherical symmetry, exerts lateral forces on the ions within the electric double layer, creates an out-of-equilibrium condition parallel to the surface, thereby moves the fluid with respect to the particle surface.

2.2.5 Interaction of light with the metal cap of Janus particles

Metallic nanoparticles (NPs) exhibit great potential in optical heating applications such as targeted therapy,[102] nanomedicine,[103,104] and cancer diagnosis.[105] These particles express unique photophysical properties, such that when they are exposed to light, the oscillating electromagnetic field of the light induces a coherent collective oscillation of the conduction band electrons at their interface creating an electric dipole. This dipole creates an electric field inside the NP which is opposite to the electric field of the light. The oscillating nature of the light creates a collective coherent oscillation of these electrons. Surface

plasmon resonance (SPR) is the maximum amplitude of the oscillation at a specific frequency.[106] The SPR can be measured with a UV-vis spectroscopy as it induces a strong absorption of light. Mie theory describes the impact of particle size, structure, shape, metal type, and dielectric constant of the surrounding medium on the electron charge density.

For particles below 50 nm in diameter, the electric field inside the NP can be considered as uniform, thereby the absorption cross-section is given as:[107]

$$\sigma_{\text{ext}} = \frac{24\pi^2 R^3 \varepsilon_m^{1.5} \varepsilon_2}{\lambda(\varepsilon_1 + 2\varepsilon_m)^2 + \varepsilon_2^2} \tag{2.32}$$

where σ_{ext} is the extinction cross-section, λ is the wavelength of the light, ε_1 and ε_2 are the real and imaginary part of the complex dielectric constant of the metal given by $\varepsilon = \varepsilon_1 + i\varepsilon_2$ and ε_m is the dielectric constant of the surrounding medium.

For larger particles, only a portion of the incident beam is absorbed by the particle ($\sigma \propto R^2$) as the electromagnetic wave is not able to penetrate the whole particle.

In the case of the Janus particles used in this thesis, the absorption cross-section of the gold cap is $\sigma_{\text{abs}} = P_{\text{abs}} I_{\text{inc}}$, where I_{inc} is the incident intensity of the beam and P_{abs} is the absorbed power. The absorbed power is dependent on the volume which the beam can penetrate. By considering a constant thickness of the gold cap (Δr) over the particle, the total volume of the cap can be written as:[56]

$$V_{\text{cap}} = \frac{2}{3}\pi(3\Delta r R_{\text{JP}}^2 + 3\Delta r^2 R_{\text{JP}} + \Delta r^3). \tag{2.33}$$

The absorbing volume can be approximated by replacing Δr with skin-depth, which is a thickness up to which electromagnetic waves could penetrate. Therefore, the absorbing volume scales with R_{JP}^2. Upon interacting of the light with the gold cap of the particle, the electrons in the conduction band get excited and they transfer their excitation energy to phonons. The generated heat is released into the surrounding environment. The resulting thermophoretic velocity is proportional to the temperature gradient across the particle $\nabla_{\parallel} T$ and the thermal mobility coefficient. The temperature gradient is proportional to the temperature increase of the gold cap ΔT divided by the particle radius,

$\nabla_{\|} T \propto \Delta T/R_{\mathrm{JP}}$. The temperature increase of the gold cap is proportional to the absorbed power by the gold cap, P_{abs}. Therefore, the temperature increase across the particle can be calculated as follows:[16]

$$\Delta_{\|} T \propto \Delta T/R_{\mathrm{JP}} = \frac{\sigma_{\mathrm{abs}} I_{\mathrm{abs}}}{4\pi\kappa_{\mathrm{T}} R_{\mathrm{JP}}^2} \tag{2.34}$$

where κ_{T} is the effective heat conductivity. Hence, this can be concluded that the propulsion velocity is proportional to the incident laser intensity, I_{abs}, if the absorption cross-section of the p square of the particle radius, $\sigma_{\mathrm{abs}} \propto R_{\mathrm{JP}}^2$.

2.2.6 Polymer brushes

Polymer brushes are polymer chains that are tethered with one chain end to a substrate through covalent bonding.[108] Such covalent bonds enable the brushes to exhibit a more stable polymer coating in comparison with methods relying on the physical adsorption of a polymer layer to a substrate. Therefore, polymer brushes are great candidates for surface functionalization where mechanical stability is of great importance. Polymer brushes' responsiveness to external stimuli such as pH, temperature, humidity, salt, etc. has also made them attract huge research interest.

A crucial parameter, apart from the environment, which determines the structure of a polymer brush is called grafting density and is the number of polymer chains per unit area of the grafted interface. The distance between two anchoring chains at the interface, d, determines the grafting density. Depending on d and R_{g} the radius of gyration of the polymer chain, various conformation of polymer brushes can be achieved, Figure 2.5.

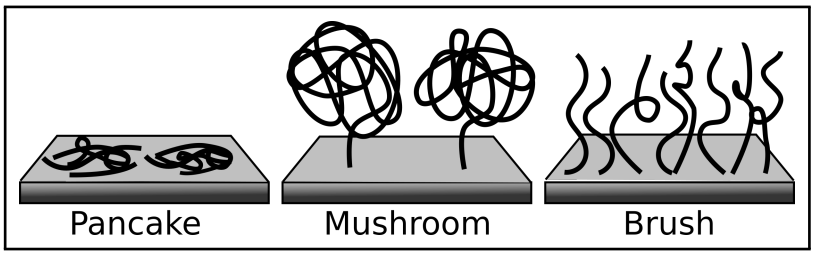

Figure 2.5: Schematic representation of brush with various grafting densities

Pancake regime is where $d > 2R_g$ and the attraction between the polymer chain and the substrate is high, or when the solvent quality is poor.

Mushroom regime is also where $d > 2R_g$, however here the attraction between the polymer chain and the substrate is weak, therefore polymer chains tend to form a coil, away from the substrate. This regime is often described for θ-solvents.

Brush regime is where $d < 2R_g$ and the polymer chain density is so high that they tend to overlap, however steric repulsion between the neighboring chains forces the chains to stretch away from the interface resulting in an extended conformation.

A parameter that describes the brush regime is the reduced tethered density, Σ, and is defined as[109]

$$\Sigma = \sigma \pi R_g^2 \tag{2.35}$$

where σ is the grafting density,

$$\sigma = \frac{d\rho \mathrm{N_A}}{M_\mathrm{n}} \tag{2.36}$$

with d the brush thickness, ρ the bulk mass density of the brush, $\mathrm{N_A}$ the Avogadro's number and M_n the number-average molecular weight of the brush.

Σ could be interpreted as the number of chains that occupy an area that a free non-overlapping polymer chain would occupy under the same experimental conditions. Therefore, $\Sigma < 1$ is the "mushroom" regime, where the interaction between polymer chains are weak, $\Sigma \approx 1$ is the transition from the "mushroom" to the brush regime, and $\Sigma > 1$ is the brush regime where the polymer chains are highly stretched. However, the fluctuations of the grafting density could cause an inhomogeneous distribution of the Σ across the grafted surface. Therefore, a true brush regime may occur where $\Sigma > 5$ or even in some cases $\Sigma > 12$.[110]

Preparation of polymer brushes

Depending on the desired application, polymer brushes can be synthesized via two approaches, the "grafting to" or the "grafting from" technique.[78,109] Each method has its unique characteristics.

Grafting to approach involves the attachment of a prefabricated polymer carrying a reactive end-group to a surface via covalent bond formation. Despite the fact that this method enables a precise characterization of the polymer prior to the surface attachment, it has many restrictions that limit its application. Achieving a high grafting density as well as a high thickness is limited due to the steric hindrance of the coiled polymer chains as the polymer chains need to diffuse through already attached chains to react with the substrate. Therefore, brushes synthesized by the grafting to approach are mostly in the pancake or mushroom regime.

Grafting from approach is a surface-initiated technique that starts from direct polymerization of the brush from the initiated surface. This method overcomes the low grafting density of the brush as the steric repulsion between the chains forces the chain to stretch out from the substrate to avoid the overlapping of chains and form a densely packed layer. This method allows an accurate control over brush thickness and architecture. In order to determine the brush molecular weight and hence its grafting density precisely, the polymer brush chains must be degrafted from the substrate. This procedure is done with the help of a cleavage agent, which hydrolyses the Si-O-Si bond which connects the polymer chain to the substrate. However, the side effect of this procedure is the hydrolysis of ester or amide bond, which might be presented in the polymer brush structure. Despite the fact that ester or amide bond hydrolysis is not expected to occur at neutral pH values, the mechanical stress which acts on these bonds imposed by the highly stretched polymer chains may lower the energy barrier for these reactions and lead to hydrolytic cleavage at neutral pH values.[111]

Surface initiated polymerization can be done via many polymerization techniques. However, living radical polymerization method is particularly attractive for the synthesis of polymer brushes due to its easy and accurate control over the thickness and grafting density of the polymer brush.

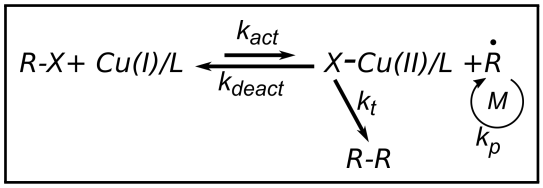

Figure 2.6: Reaction scheme of ATRP technique

Atom transfer radical polymerization (ATRP), introduced by Matyjaszewski and coworker in 1995, has been the most widely used technique for the synthesis of polymer brushes.[108] The mechanism of ATRP is displayed in Figure 2.6. The polymerization technique relies on the reversible redox activation of a dormant alkyl halide-terminated polymer chain end (R-X) by a halogen transfer (X) to a transition metal complex.[112] The homolytic cleavage of the carbon-halogen bond leads to the generation of a free and active carbon-centered radical species at the polymer chain end. This activation is achieved through a single electron transfer from the metal complex to the halogen atom, which subsequently leads to the oxidation of the transition metal complex. At the same time, the oxidized catalyst reconverts the propagating radical chain end to the halogen-capped dormant species (deactivation). ATRP is controlled by an equilibrium between active propagating radicals and dormant species, highly towards the dormant species, which leads to the generation of low propagating radicals and an increase over the control of polymerization.

Surface-initiated ATRP is a versatile method for functionalization of various substrates such as silicon, gold, metal, etc. with polymer brushes. It consists of a two-step process in which first the initiator gets immobilized on the substrate, next the chain growth from the initiator kicks off the polymerization. Due to the living character of this technique, ultrathin polymer films with low dispersities can be synthesized.[113]

Chapter 3

Experimental Section

3.1 Particle Tracking

3.1.1 Microscopy setup

The experimental setup is schematically shown in Figure 3.1. The setup is home-built and inspired by an analogous set up at the group of Prof. Cichos. It consists of a dark-field condenser (Olympus NA 1.2-1.4) to achieve a greater detection of the gold cap of particles. The scattered light of the particles is collected by an oil-immersion objective (Olympus 100x, adjustable NA 0.5-1.35) and imaged by a sCMOS camera (ANDOR, ZYLA 4.2). A laser (Pegasus, Pluto, 800 mW) with a wavelength of 532 nm is coupled to the microscope. To achieve a wide parallel beam at the objective, the laser beam passes through a beam expander (Thorlabs, 5-10x, 350-650 nm) and a lens subsequently. The beam expander widens the beam diameter and the lens focuses the beam to the back focal plane of the objective. As a result, a wide parallel laser beam will be formed at the objective.

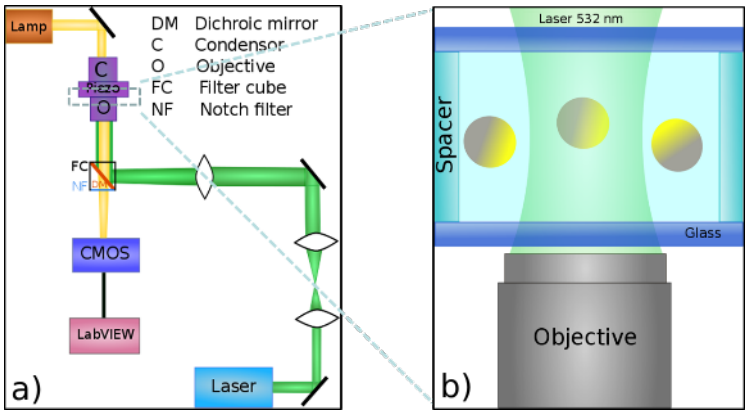

Figure 3.1: a) illustration of the dark-field setup, b) wide parallel beam at the objective

The following sections elaborate the function of the essential optical elements used in the setup in more details.

3.1.1.1 Dark-field condenser

The appearance of the stars in the sky at night is due to the high contrast between the black sky and the faint light of stars. The same principle can be applied in microscopy technologies to enhance the visibility of unstained specimens. This method is called dark-field microscopy which is a background free imaging method with a large signal-to-noise ratio and a high sensitivity.[114] The ideal candidates for this method are specimens with similar refractive index to that of their surroundings.

In contrast to bright-field microscopy which let the central light passes through and around the specimen, dark-field illumination technique blocks the central light and allows only the oblique rays to hit the specimen. To achieve this purpose, a dark-field condenser is equipped with a *dark-field patch stop* which is a disc placed on the light path that prevents the light to enter the condenser and leaves a circular ring of illumination. The illumination ring is collected by the condenser lens and is focused on the specimen. Figure 3.2 illustrates the bright-filed vs. dark-field illumination.

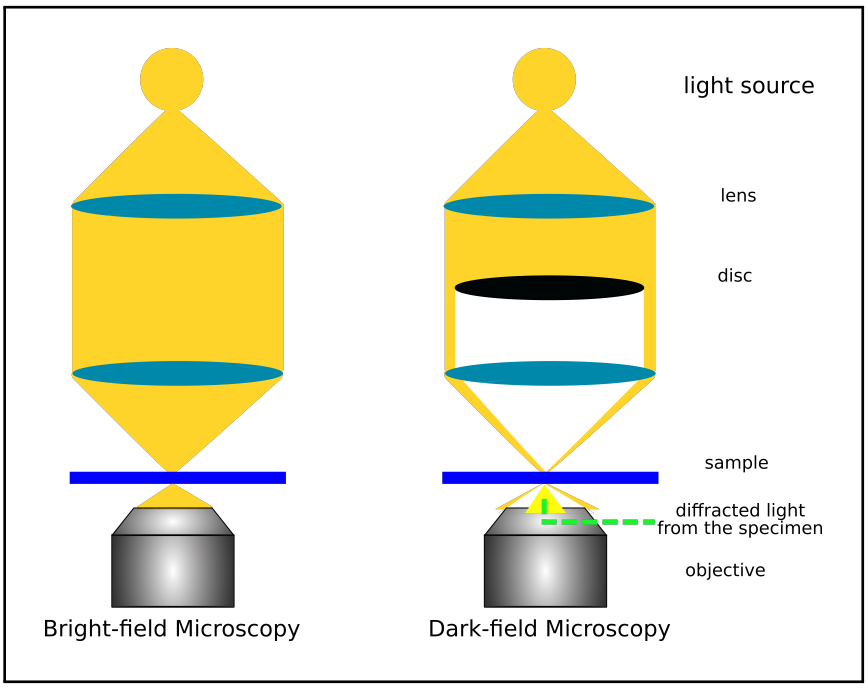

Figure 3.2: Bright-field vs. dark-field microscopy

3.1.1.2 Laser

The laser used in the experiments is a diode-pumped solid-state laser (DPSS), which delivers up to 800 mW optical power at 532 nm with near TEM00 quiality. The laser has a beam diameter of 2 mm and a power stability of $\pm$ 5 over 1 hour. The laser operates at wavelength of 532 nm to match the plasmonic properties of the gold cap of the Janus particles. In "stand alone" operation the laser can be controlled via a remote control panel to switch it on an off and to adjust its power. The dependence of the laser output power on the remote control display is shown in Figure 3.3.

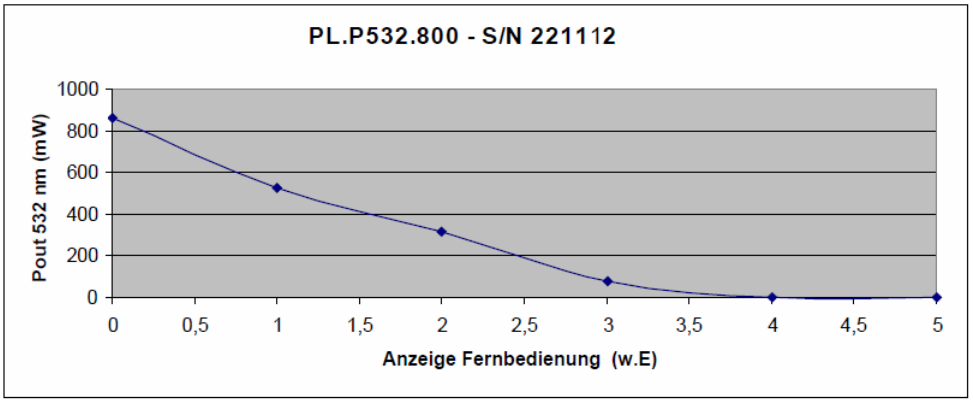

Figure 3.3: Dependence of the output power on the display Remote control, adapted from www.pegasus-lasersysteme.de

The laser beam passes through mirrors outside of the microscope and a dichroic mirror inside the microscope subsequently until it reaches the objective. The outcome is a focused beam, Figure 3.4. The objective used in the setup has a 100× magnification with a back focal length of 1.8 mm.

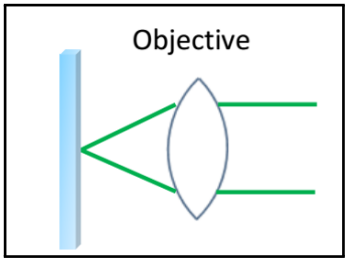

Figure 3.4: Generation of a focused laser spot at the sample

For the sake of self-propulsion measurements it is essential that instead of a focused laser spot, create an area of illumination in which the laser intensity is uniform. This was achieved by implementing a lens with the right focal length (250 mm) which yields a wide parallel beam with a diameter of 14.4 µm, Figure 3.5.

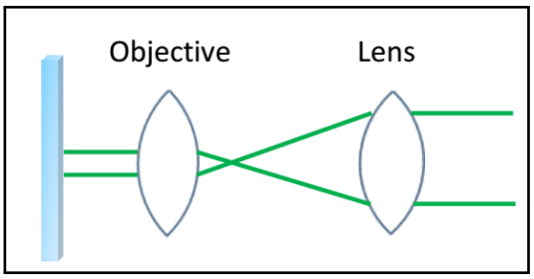

Figure 3.5: Generation of a wide parallel beam at the objective

To enlarge the laser beam at the objective a beam expander with a magnification of 5x is added to the setup. Considering the focal length of the lens, $f_3 = 250$ mm and focal length of the Olympus objective, $f_3 = 1.8$ mm, the diameter of the out-coming beam can be calculated according to the following formulas,[115]

$$M = \frac{f_2}{f_1} = \frac{D_2}{D_1} \quad , \quad \frac{f_3}{f_2} = \frac{D_4}{D_3} \tag{3.1}$$

where D, f, and M are beam diameter, focal length of a lens, and magnification of a beam expander, respectively. The combination of the lens and the beam expander leads to a beam with a diameter of $D_3 = 72$ µm, Figure 3.6.

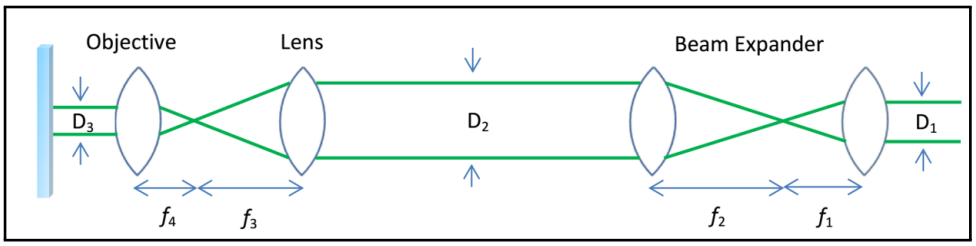

Figure 3.6: Layout of the wide field laser illumination setup

3.1.1.3 Dichroic mirror and notch filter

The dichroic mirror used in the setup is dichroic longpass filter with a cut-on wavelength of 600 nm. These mirrors are highly transmissive above their cut-on wavelength and highly reflective below it. Here, the mirror has a reflection wavelength of 450-570 nm to reflect the laser beam on to the objective, and a transmission wavelength of 625-1600 nm to transmit the microscopy light to the

camera. The reflection and transmission curves of the dichroic mirror are shown in Figure 3.7a,b. To protect the camera a notch filter OD4 532 nm is placed under the dichroic mirror to block the laser beam in case it passes through the dichroic mirror, Figure 3.8.

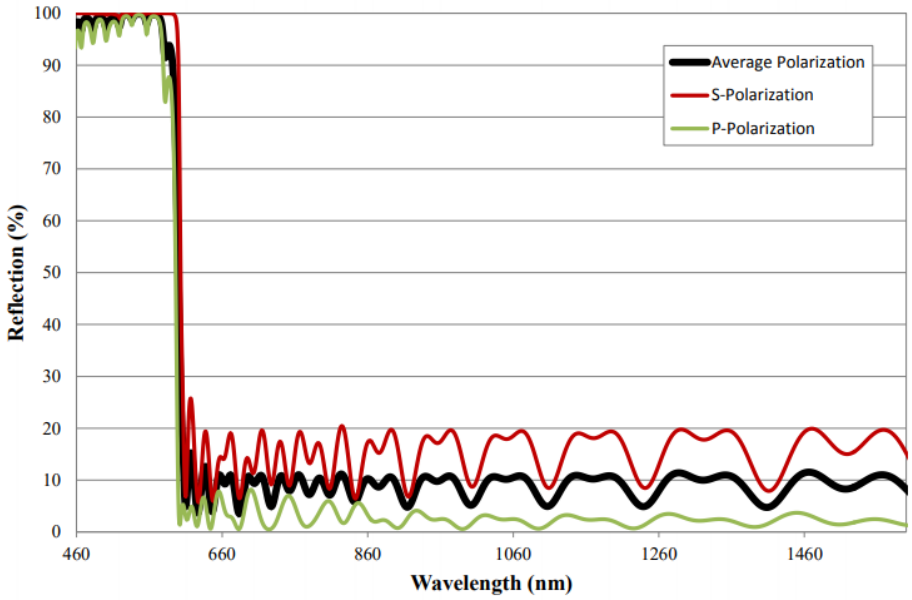

a)

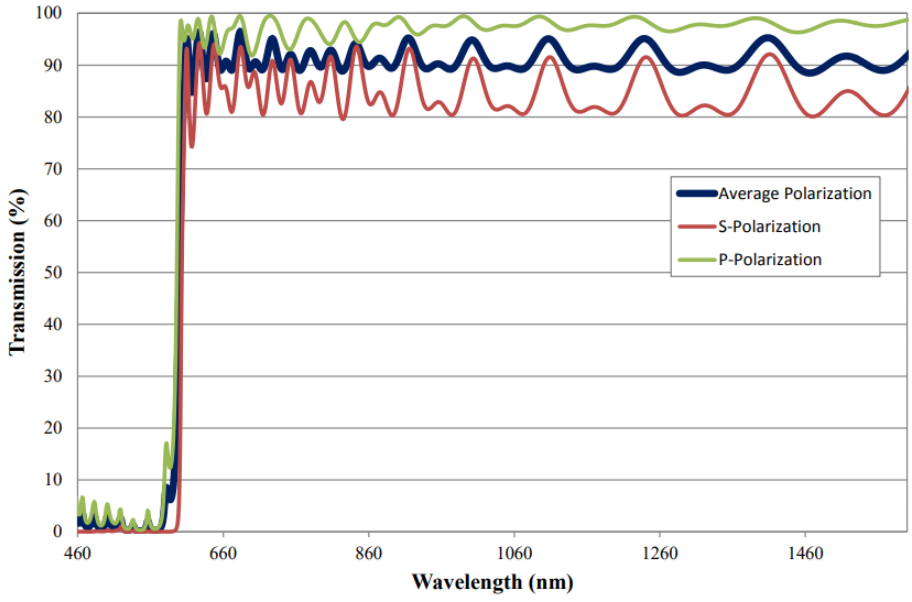

b)

Figure 3.7: a) Reflection and b) transmission curves of the dichroic longpass filter with a cut-on wavelength of 600 nm, adapted from www.edmundoptics.com

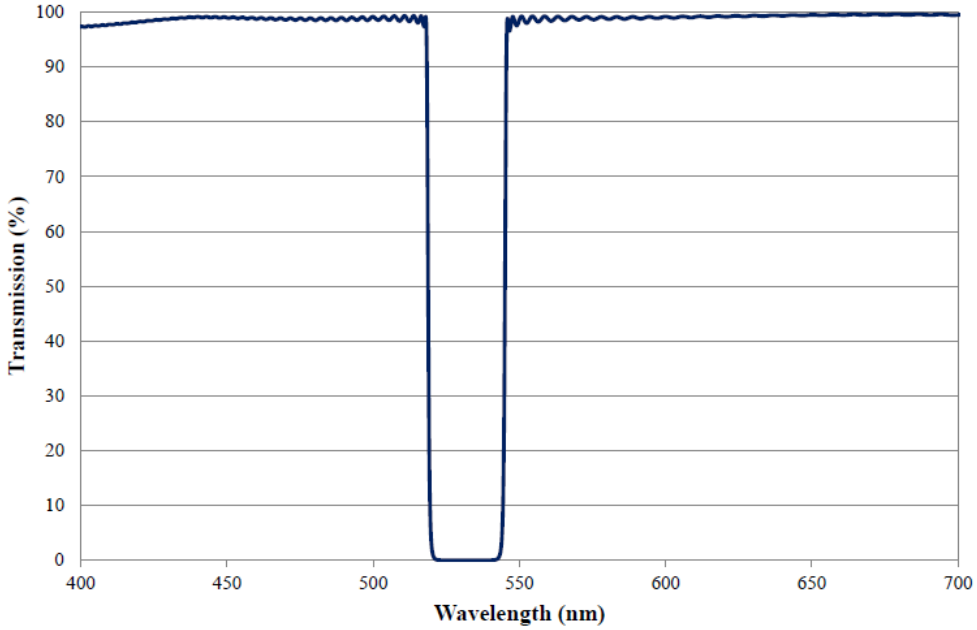

Figure 3.8: Transmission curve of the notch filter 532 nm, adapted from www.edmundoptics.com

3.1.1.4 Nano-positioning stage

An important aspect of the setup is the presence of a nano-positioning stage (P-545.2R7) which is designed for the fine positioning as well as the fast and precise motion of small objects. The piezo stage has the motion range of $200\,\mu\text{m} \times 200\,\mu\text{m}$ and it is mounted on a M-545.2MO which is an XY microscope stage with a 25 mm $\times$ 25 mm range of motion. The corresponding software identifies the position of the piezo stage, and it relocates the stage according to the defined target position and the step size. The P-545 is equipped with piezoresistive strain sensors which consist of a thin semiconductor foil attached to the piezo ceramic for enhanced precision.

3.1.1.5 Camera

Unlike the conventional camera equipped with charge coupled device (CCD) sensors, the camera used in the setup is based on the scientific complementary metal-oxide-semiconductor (sCMOS) technology. CCD and CMOS are both two different technologies for capturing images and each method offers unique

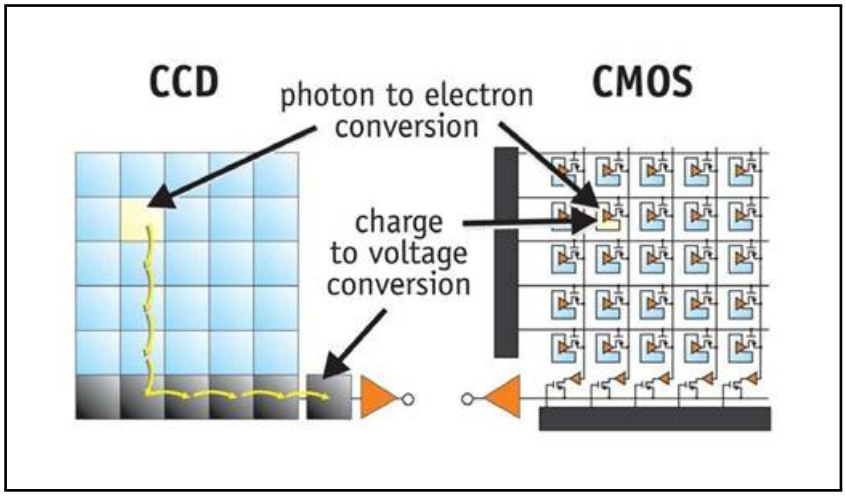

Figure 3.9: CCD vs. CMOS sensor, adapted from www.meroli.web.cern.ch

properties. Both CCD and CMOS sensors are consisting of thousands of light sensitive cells or pixels, arranged in a 2-dimensional grid, capable of converting light into electric charge. The difference lies on the readout process. In CCDs, each pixel's charge is transferred to the neighbouring pixel until all the charges are accumulated in a single pixel, where they convert into voltage. In CMOS sensors, due to the presence of transistors at every single pixel, the charge-to-voltage conversion takes place there, Figure 3.9. As each pixel often has amplifier the chip outputs digital bits. CMOS cameras are faster in processing signals than CCDs, therefore, they are ideal for fast image acquisition applications.[116,117] The setup is equipped with Zyla 4.2 which is a 4.2 megapixel camera and offers 100 frames per second (fps) at full resolution.

3.1.1.6 Sample preparation for self-propulsion measurements

To prepare the cell for the self-propulsion tests, 0.5 μL of the Au-PS Janus particle dispersion in water was deposited between two glass slides. The edges of the glass were covered with silicon paste as a spacer. The presence of a spacer is inevitable in order to keep the movement of particles in 2D. Moreover, it prevents the evaporation of water inside the cell. The cell was placed on top of the objective. Self-propulsion tests were started by switching on the laser. Figure 3.10 shows the sample cell. The thickness of the spacer is roughly 10 μm.

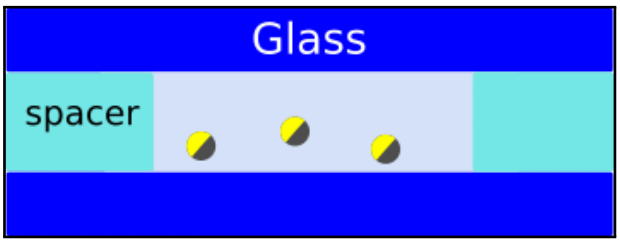

Figure 3.10: Schematic of the sample cell for self-propulsion measurements

3.1.2 Real-time particle tracking and data analysis

3.1.2.1 LabVIEW program

Labview is a visual programming language which is commonly used for data acquisition. It consists of two panels, a block diagram where all the codes are stored and all the processing occurs, and a front panel which is basically the user interface. The real-time particle tracking program written in LabVIEW controls the components of the setup, mainly the piezo stage and the image acquisition of the camera during the self-propulsion measurements. This program is written by Dr. Rene Straßnick at TU Berlin.

The block diagram of the program involves the labview drivers of the camera and the piezo stage. The program finds the particle by applying an intensity threshold such that it distinguishes the particle from its background. Next, the program determines the center of the mass of the particle in every single frame. The same procedure is applied to detect and track the gold cap of the particle. Once the particle is found its position in every single frame is stored in real-time. The program allows the user to define an area of interest (AOI) as well as the distance from the center of AOI where the particle moves freely without the piezo stage being involved. However, as soon as the particle moves beyond the allowed distance the piezo stage becomes active and moves itself such that the particle is again in the center of illumination. The outcomes of the program are time, frames, and the position of the particle and its cap in every frame. Figure 3.11 shows the front panel of the labview program.

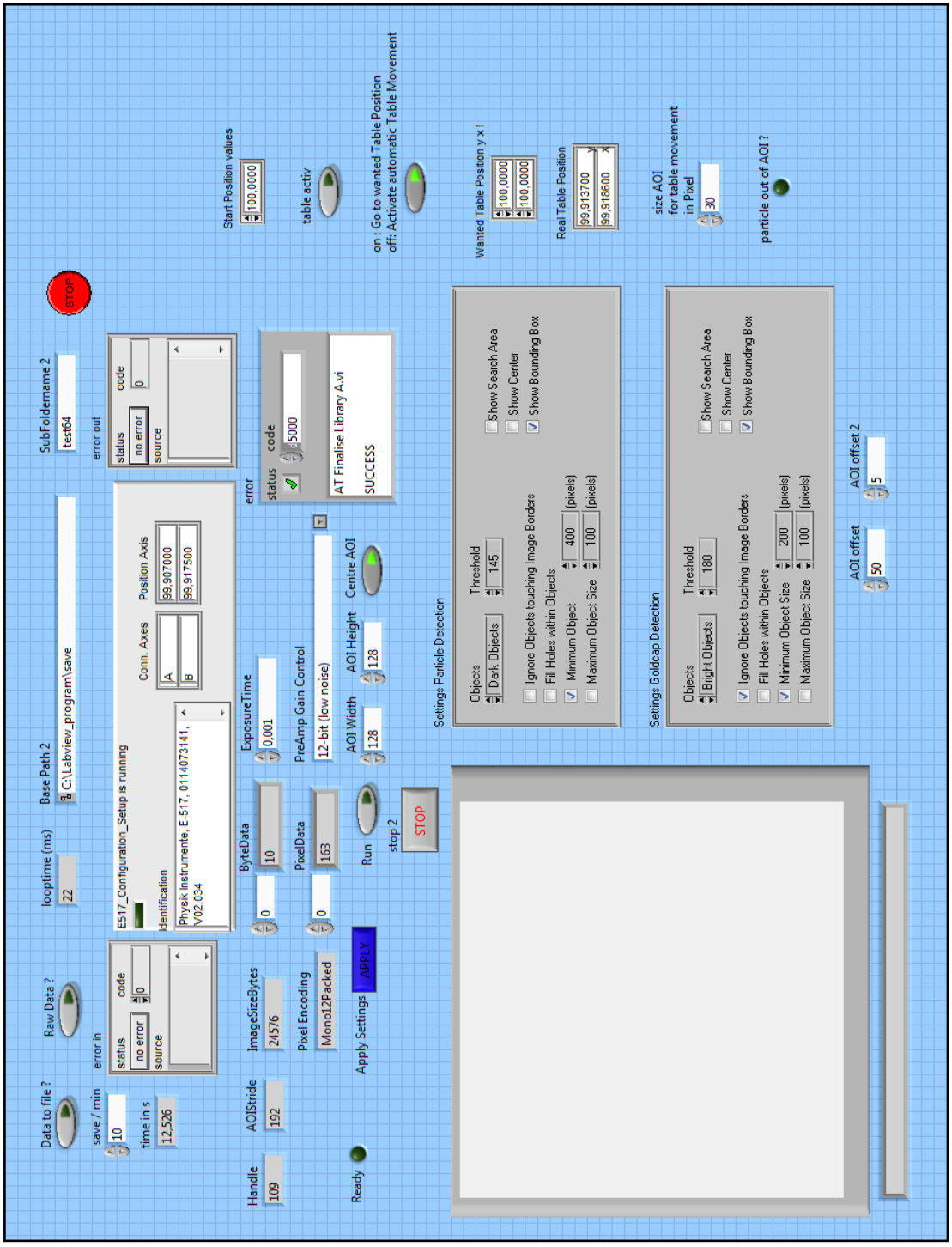

Figure 3.11: Front panel of the labview program

The current labview program has few limitations in terms of data acquisition. First, at a ROI of 128 $\times$ 128 pixels it generates only $\approx$ 40 fps. This number of frames is sufficient for measurements on particle with diameters above 2 µm, however, this limits its application when small particles with faster movements and lower rotational times are desired to investigate. Second, the number of frames per second further decreases when the raw images of the frames are saved simultaneously during the measurement. Therefore, no videos are recorded during the measurements. This drawback of the program is expected to be solved by changing the particle tracking system. The alternative method should create a binary image at a threshold above the background noise. Thereby, the center of mass of the particle is determined. Furthermore, by creating a binary image at high threshold the position of the gold cap of the particle can be identified. This methods allows a faster data acquisition during the measurement, hence the number of frames increases. Figure 3.12 shows the binary image of a particle.

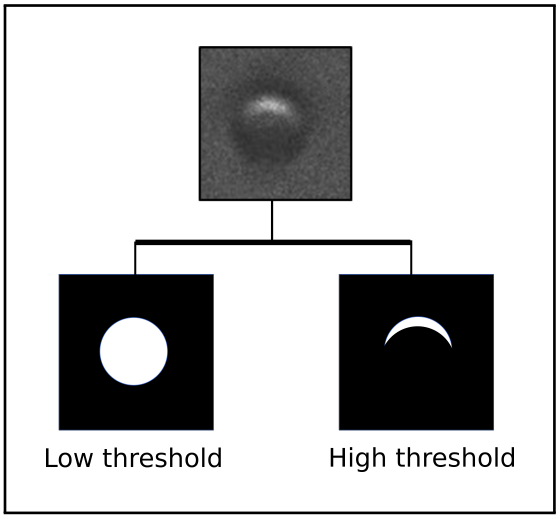

Figure 3.12: Determination of center of mass and gold cap of the particle by transforming every frame to a binary image

3.1.2.2 Data analysis

The data analysis is performed by a custom python script written by Dr. Straßnick at TU Berlin. The outcome of the script is trajectory and mean square displacement of the particles. Figure 3.13 represents the particle displacement

with respect to the time interval Δt. The time interval is the time needed to capture a frame. For sake of simplicity consider a frame rate of 1 s^{-1} and a movie of 30 frames. To calculate the mean square displacement (MSD) of a particle at $\Delta t = 1$, not only the difference in particle position between frames 1 and 2, but also the difference between frames 2 and 3, 3 and 4,... and 29 and 30 must be calculated. For obtaining the MSD at 2$\times\Delta$t the difference in particle position between frames 1 and 3, 2 and 4, 3 and 5,... and 28 and 30 must be calculated. At longer time intervals the number of data decreases. Therefore, to achieve a smooth MSD vs Δt, it is necessary to take at least $\sim$ 200 mean square displacements at every Δt and the total measurement time must be at least 10$\times$ longer than the largest time interval to be calculated.[118]

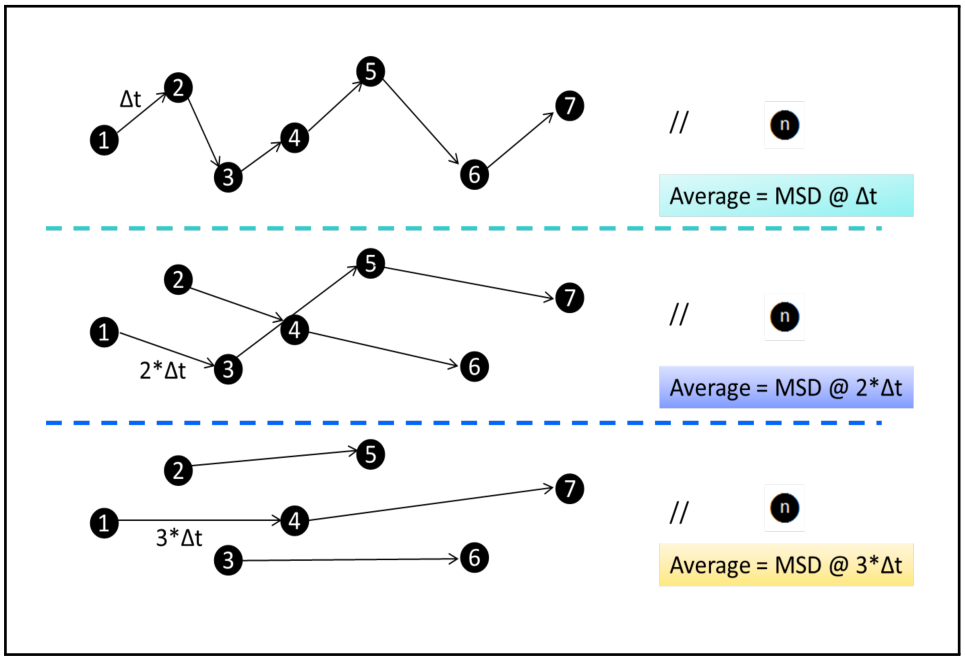

Figure 3.13: Particle displacement with respect to the time interval Δt, the black circles represents the position of particle in every single frame

The MSD of the particles is calculated according to the following equation.

$$\langle \Delta r^2 \rangle = \langle \Delta x^2 \rangle + \langle \Delta y^2 \rangle \tag{3.2}$$

3.2 Materials

2,2'-Bipyridine, Nile Blue A, N,N,N',N'',N''-pentamethyldiethylenetriamine (PMDETA), N-isopropylacrylamide (NIPAM), poly(ethylene glycol) methyl ether methacrylate (POEGMA), Cu(I)Cl, Cu(II)Cl were purchased from Sigma-Aldrich (Munich, Germany). 2-Hydroxyethyl methacrylate (HEMA), 97% stabilized with 4-methoxyphenol was purchased from Alfa Aesar. Cu(II)-bromide was purchased from Acros. The silicon wafers (thickness: $775 \pm 15\,\mu m$, dopant: boron, and crystalline orientation: [1 0 0]) were purchased from Siltronic AG (Munich, Germany). The Au-PS Janus particles were a kind gift from Prof. Cichos at the Institute of Experimental Physics, University of Leipzig. Polystyrene (PS) particles were purchased from Microparticles GmbH (Berlin, Germany). Coverslip glasses were purchased from Th. Geyer GmbH. co. KG. (Renningen, Germany). The initiators 2-bromo-2-methyl-N-(11-(trichlorosilyl)undecyl) propanamide (BMPUS) and 2-bromo-2-methyl-N-[3-(triethoxysilyl)-propyl]-propanamide (BTPAm) were synthesized according to the literature. All the reagents were used as received without any further purification.

3.3 Sample Preparation

3.3.1 Brush synthesis

PNIPAM brushes: The initiator BTPAm was synthesized according to the procedure reported by Laurent *et al.*[119] and was synthesized by Dr. Dikran Boyaciyan. Polymer brushes were synthesized via a grafting-from approach using surface initiated atom transfer radical polymerization (SI-ATRP). Prior to the initiation step, the silicon wafers were etched by Piranha solution (H_2SO_4: H_2O_2; 1: 1) for 30 minutes, then rinsed extensively with Milli-Q water and dried under a stream of nitrogen.

A monolayer of the initiator was deposited onto the silicon wafers using the self-assembly method. Therefore, the etched silicon wafers were placed into the solution of BTPAm in anhydrous toluene (0.4 mM). The reactor, Figure 3.14,

containing the initiation solution was sealed and kept in dark overnight (15h) at room temperature. Afterwards, the initialized silicon wafers were removed from the reactor, washed with toluene and ethanol consecutively, and dried under a stream of nitrogen.

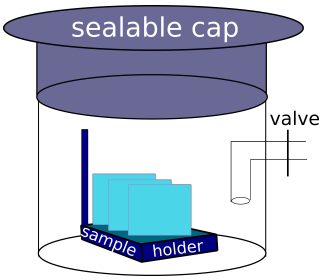

Figure 3.14: Scheme of the glass reactor developed for synthesizing polymer brushes on substrates. The teflon sample holder has 8 slots which allows simultaneous polymerization of up to 8 samples in one batch

The synthesis procedure of PNIPAM brushes was adopted from Fujie *et al.*[120] In brief, 2.0 g of NIPAM was dissolved in 35 mL of methanol/water mixture (1:1 v/v), degassed with nitrogen for 30 minutes, followed by adding 0.0195 g CuCl and 150 µL PMDETA and degassed for another 30 minutes. Then, initialized silicon wafers were placed into the polymerization solution. The polymerization reaction was carried out for a desirable time and terminated by removing the wafers from the solution. Subsequently, wafers were placed in Milli-Q water under sonication for 5 minutes to remove the excessive polymerization material. Finally, brush-functionalized wafers were dried under a stream of nitrogen.

POEGMA brushes: The initiation step is the same as the above-mentioned procedure for PNIPAM. The polymerization procedure is adopted from Zhuang *et al.*[121] To carry out the polymerization, initiated substrates were placed into a degassed solution containing 19.4 mL OEGMA (42 mmol) and 22 mL deionized water for 15 minutes, followed by adding 320 mg bipyridine (bpy) (2.0 mmol) and 82 mg CuCl 840 µL and stirring for 30 minutes. Afterwards, the initialized silicon wafers were immersed in the polymerization solution. The polymerization was terminated after the desired time by removing the substrates from the solution and placing them into Milli-Q water. The thickness of brushes can be tuned according to the given polymerization time, upon increasing the polymerization time brushes grow longer.

PHEMA brushes: The initiator BMPUS was synthesized according to literature.[108] The etched silicon wafers were placed into the solution of BMPUS in anhydrous toluene (10 mM), the reaction cell was sealed and kept in dark overnight at room temperature. The rinsing procedure is as mentioned above. The polymerization procedure is adopted from Fang *et al.*[122] The monomer solution was prepared by degassing 40 mL of HEMA/water (1:1 v/v) for 30 minutes, followed by adding 59.4 mg CuCl, 16.14 mg $CuCl_2$, and 187.42 mg bpy under a nitrogen atmosphere and degassed for an hour. Then the initiator-coated wafers were put into the polymerization solution and the polymerization was carried out at room temperature. The termination procedure is the same as the procedure described above.

3.3.2 Preparation of Janus particles

Initially, the coverslip glass was cleaned with acetone, ethanol, and Milli-Q water and further treated with an oxygen plasma for 2 minutes. 10 µl of polystyrene solution was spin-coated on the glass at 8000 rpm for 30 seconds. Afterwards, a 5 nm layer of chromium followed by a 50 nm layer of gold was deposited on the PS particles by vacuum evaporation. Chromium is added to enhance the adhesion of gold to the particles. Janus particles were synthesized by Santiago Muiños Landin at the University of Leipzig. In this thesis Au-PS Janus particles with diameters of 1 µm and 2.4 µm are used. The preparation procedure is the same for particles with various diameters.

3.3.3 Silanization of the glass substrate

Silanization of the glass substrate was achieved by inserting the coverslip glass into a 5% solution of dichlorodimethylsilan ($C_2H_6Cl_2Si$) in toluene for 20 minutes, followed by washing the coverslips with methanol for 15 minutes in an ultrasonic bath.

3.4 Particle/Brush Characterization Methods

3.4.1 Ellipsometry

Ellipsometry is a non-destructive, non-contact optical technique that measures the change of the state of polarization of light as it gets reflected or transmitted from the surface of interest. To describe these changes in the state of polarization two parameters are described: Δ and ψ.[123,124]

$$\Delta = (\delta_p^r - \delta_s^r) - (\delta_p^i - \delta_s^i) \tag{3.3}$$

$$\tan\psi = \frac{|E_p^r|/|E_p^i|}{|E_s^r|/|E_s^i|} \tag{3.4}$$

Here, E is the amplitude, δ is the phase of the light, p and s indicate the parallel and perpendicular components of the light, and i and r the incident and reflected beam. The reflectivity properties of a sample can be described by reflection coefficients r_p and r_s:

$$r_p = \frac{|E_p^r|}{|E_p^i|} e^{i(\delta_p^r - \delta_p^i)} \tag{3.5}$$

$$r_s = \frac{|E_s^r|}{|E_s^i|} e^{i(\delta_s^r - \delta_s^i)} \tag{3.6}$$

With these equations the fundamental equation of ellipsometry can be obtained, which relates Δ and ψ with the reflectivity properties of the sample.[123]

$$\tan^{i\Delta} = \frac{r_p}{r_s} \tag{3.7}$$

Considering the ellipsometric angles Δ and ψ and applying the right layer model, thickness and refractive index of a polymer layer can be obtained.

A schematic representation of a null-ellipsometer is presented in Figure 3.15. It consists of a monochromatic laser which passes through a quarter-wave plate to generate a circular polarized light. Subsequently, the laser beam passes through a polarizer and a compensator where the polarization state of the beam changes to elliptical. The laser beam reaches the sample, gets reflected from it, and hits

the analyzer. The analyzer rotates to minimize the intensity of the beam at the detector.

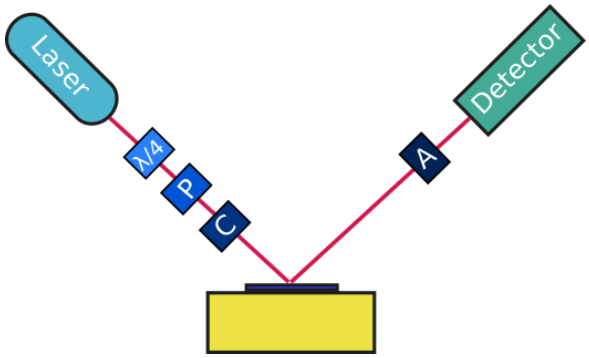

Figure 3.15: Schematic representation of a polarizer-compensator-sample-analyzer null-ellipsometer

Ellipsometry measurements were carried out using a null-ellipsometer from Optrel GbR (Sinzing, Germany) equipped with a He-Ne laser ($\lambda = 632\,\mathrm{nm}$, P = 2 mW). The measurements in a dry atmosphere were performed at the incident angle of 70° with respect to the surface normal, whereas the measurements in liquid were carried out at the incident angle of 60°. A stainless steel cell filled with the desired liquid was used for the measurements in liquid. The samples were equilibrated in the liquid for at least 30 minutes prior to measurement. Temperature controlled measurements were carried out by heating up/cooling down the water in the cell through a thermostat from 15 to 60°C with an incremental step of 5°C. Once the desired temperature was achieved, the temperature was kept constant for 10 minutes to let the sample equilibrate, and then the measurement was performed. Temperature variations were controlled through a script written in Pascal programming language.

3.4.2 Atomic force microscopy

Atomic force microscopy is a versatile tool to image the topography of surfaces with high resolution. It measures the forces between a probe and the surface of a sample. Figure 3.16 illustrates the principle of an AFM. A tip is mounted at the end of a cantilever, which scans over the surface of the sample. The laser beam gets reflected from the backside of the cantilever onto a detector, hence the position of the cantilever is detected. The force between tip and sample

makes the cantilever bend, subsequently, the position of the laser beam at the detector is shifted. The lateral resolution of an AFM is limited by the diameter of the tip. For scanning purposes, a sharp tip with a radius of a few nanometers is attached to the cantilever.[125]

The colloidal probe technique is a well-established method for studying surface forces.[126] A colloidal probe that is attached to the cantilever moves towards the substrate in the normal direction with the help of a z-piezo stage. The vertical position of the colloidal probe and the deflection of the cantilever is recorded and converted into force-distance curves. Upon applying the appropriate model to the curves, the elastic modulus of substrates can be obtained.

Scanning: AFM measurements were perfumed in the intermittent contact mode, in which the tip taps the surface while scanning, hence reducing the possible damage of the sample. The instrument Cypher Scanning Probe Microscope from Asylum Research (Santa Barbara, CA, USA) was used both in a dry and liquid environment. For the measurement in ambient condition AC160TS cantilevers from Olympus were used. These cantilevers are made of silicon coated with aluminum, designed for AC mode AFM in air, and has a tetrahedral tip on the exact end of the cantilever. The tip has a length and radius of 14 μm and 7 nm, respectively. The Spring constant of the cantilever is 42 N/m and has a resonance frequency of 300 kHz. The sample roughness was determined by root mean square deviation of the height σ.

$$\sigma = \sqrt{\frac{1}{m}\sum^{m}(z_i - \bar{z})^2} \tag{3.8}$$

AC240TS cantilevers with a spring constant of 2 N/m and resonance frequency of 70 kHz were used for the AC mode in a liquid environment. The tetrahedral tip has the same dimensions as AC160TS. This cantilever is suitable for observing surface topography and viscoelasticity of soft samples.

Colloidal Probe AFM: Elastic properties of brushes were characterized by force measurements and carried out using the MFP-3D instrument from Asylum research. A silica particle with a diameter of 6.62 μm was glued at a cantilever by using a micromanipulator under the control of an optical microscope. The samples were placed in a liquid cell in contact with water and equilibrated for

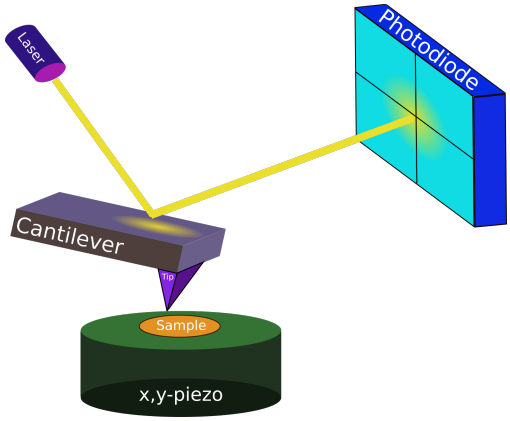

Figure 3.16: Schematic of an AFM Setup

30 minutes prior to measurement. Elastic properties of POEGMA and PHEMA brushes were characterized in water at room temperature. In general, the data acquisition was based on force mapping mode, each map consisting of 10×10 force curves over a scan size of 20×20 μm^2. The elastic modulus was obtained by fitting the force-distance curves with the Hertz model.

Full-indentation was conducted to obtain information about the thickness of the brush-functionalized substrates and to compare the results with the ones obtained through the AFM-scratch method as well as ellipsometry. An AFM force measurement setup was used for the indentation in the z-direction. An AC160TS cantilever was used and it was first calibrated against a clean silicon wafer. The measurements were performed at room temperature.

3.4.3 X-ray reflectometry

X-ray reflectometry (XRR) is a non-destructive scattering technique to characterize the internal structure of thin films. X-rays can be reflected or refracted similar to light, as they interact with a homogeneous medium. The refractive index of the medium which describes the propagation of the beam into the medium in the X-ray region can be described as following:[127]

$$n = 1 - \delta - i\beta \tag{3.9}$$

where, δ and β are dispersion and absorption terms of the material, respectively. δ and β can be defined as:

$$\delta = \frac{\lambda^2}{2\pi}\rho_e r_e \tag{3.10}$$

$$\beta = \frac{\lambda}{4\pi}\mu \tag{3.11}$$

where ρ_e is the electron density, r_e is the Thomson radius of a free electron, and μ is the linear absorption coefficient.

Figure 3.17 illustrates the total external reflection, where the incident beam is totally reflected below the critical angle and $\alpha_i = \alpha_r$. X-ray measurements are performed below the critical angle.

When a photon is reflected on a substrate its momentum changes. This momentum transfer, under the assumption of elastic scattering $|\overrightarrow{k_i}| = |\overrightarrow{k_r}|$, can be described as the difference between the incident beam ($\overrightarrow{k_i}$) and the reflected beam ($\overrightarrow{k_r}$):

$$\overrightarrow{q} = \overrightarrow{k_r} - \overrightarrow{k_i} \tag{3.12}$$

where $|\overrightarrow{k}| = 2\pi/\lambda$.

For a given wavelength in the z-direction, a momentum transfer can be described as:

$$q_z = \frac{4\pi}{\lambda}\sin\alpha_i. \tag{3.13}$$

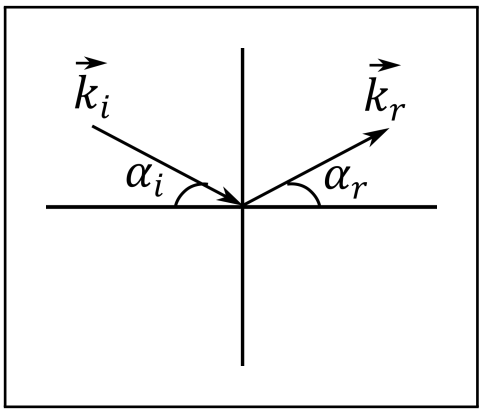

Figure 3.17: Total external reflection

Reflectivity is described as the reflected beam intensity divided by the intensity of the directed beam, $R = I_r/I_i$. Figure 3.18 shows a typical reflectivity curve

as a function of momentum transfer. Minima and maxima or the so-called "Kiessig fringes" are the results of the constructive and destructive interference of the reflected beam from an interface. Upon increasing the angle of incidence, the total reflected intensity decreases as the transmission through the material increases.

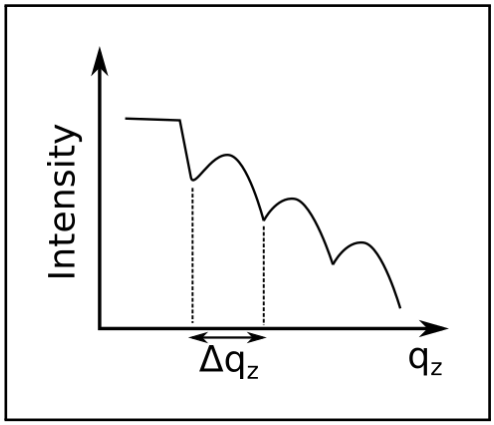

Figure 3.18: A typical reflectivity curve as a function of momentum transfer

According to Bragg's law, the thickness of a layer in real space is proportional to the length of an oscillation in the reciprocal space, therefore:

$$2d \sin \alpha = n\lambda \tag{3.14}$$

with eq. 3.13 leads to

$$d = \frac{2\pi}{\Delta q_z}. \tag{3.15}$$

The reflectometry measurements were carried out with the X-ray reflectometer D8 Discover (Bruker, Karlsruhe, Germany), using the Kα radiation source from a copper anode with the wavelength of $\lambda = 1.54\,$Å. The scan range varied from $2\theta = 0° - 5°$ with a step width of $0.01°$.

3.4.4 Zetasizer

Zeta potential measurement is a versatile method to measure the surface charges of colloidal particles in a suspension. It relies on electrophoresis, in which an

electric field is applied and the resulting particle velocity is determined by Doppler-velocimetry.[128]

The zeta potential of the Au-PS and PS particles were determined by using the Zetasizer Nano series Nano-ZS (Malvern Instruments, UK) at room temperature. A dilute suspension of particles in Milli-Q water was prepared for the zeta potential measurements.

3.4.5 Contact angle measurements

The contact angle of a liquid drop on a solid surface is described by the Young equation, where the drop is in a mechanical equilibrium of three interfacial tensions, as shown in Figure 3.19.[129]

$$\cos\theta = \frac{\gamma_{sv} - \gamma_{sl}}{\gamma_{lv}} \tag{3.16}$$

γ_{sv}, γ_{sl} andγ_{lv} are the solid-vapor, solid-liquid, and liquid-vapor interfacial tensions, respectively. θ is the contact angle.

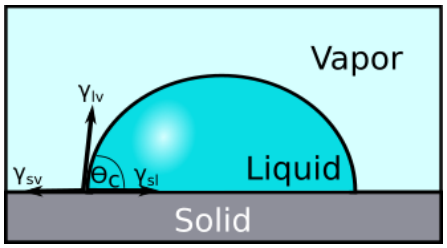

Figure 3.19: Schematic representation of static contact angle. Interfacial tensions are drawn by arrows (S=solid, L=liquid, and V=vapour)

Contact angle measurements can be performed by various methods, goniometer method, Wilhelmy plate method, and drop-shape analysis. In this work, static contact angles were measured with a Goniometer OCA20 (Dataphysics, Germany) by the Sessile drop method. The clean functionalized silicon wafers were placed on a sample stage in a closed cell which is filled up to 1/3 with deionized water. To achieve a saturated environment samples were kept in the closed cell for 30 minutes and afterwards, a 4 µL drop of water was placed on

the sample via a syringe. 5 drops were placed on various spots of the sample and the contact angles were determined through the tangent fitting method.

3.4.6 Scanning electron microscopy

SEM measurements were carried out on a Phenom XL desktop SEM in the group of Prof. Roth at TU Darmstadt by Thorsten Abel. 5 µL of the Janus particle suspension was placed on an SEM disc. After drying, the disc was inserted into the sample holder and transferred to the tabletop SEM. The SEM was operated at the acceleration voltage of 10 kV. The images were recorded using a secondary electron detector (SED) camera which enables a surface-sensitive imaging.

3.4.7 Streaming current measurements

Streaming current is generated due to the migration of ions within the electrical double layer of the substrate due to the flow generated by the imposed pressure gradient. Within EDL the distribution of ions at the interface is equal under the equilibrium conditions which originates from the balance between Coulombic and entropic interactions.[130]

Streaming current measurements were performed by Dr. Johannes Lützenkirchen at KIT with a SurPASS electrokinetic analyzer (Anton Paar) at room temperature. The measurements were carried out in a rectangular streaming channel with a width of 10 mm and a length of 20 mm and a height of 100 µm, Figure 3.20. The samples were placed at the top and the bottom of the channel.[131,132] Once the sample comes into contact with water the counter ions get absorbed at the solid/liquid interface. Upon applying a pressure difference parallel to the solid/liquid interface the hydrodynamically mobile ions get transported across the channel which gives rise to the generation of streaming current. Consequently, the zeta potential of the samples could be obtained from the streaming current measurement according to the following equation:[133]

$$\zeta = \frac{\eta L}{\varepsilon_0 \varepsilon_r} \frac{dI}{dP} \tag{3.17}$$

where η is the dynamic viscosity of the fluid, L is the length of the channel, ε_0 is the permittivity of the vacuum, ε_r is the dielectric constant of the fluid, I the streaming current, and P is the pressure difference across the channel.

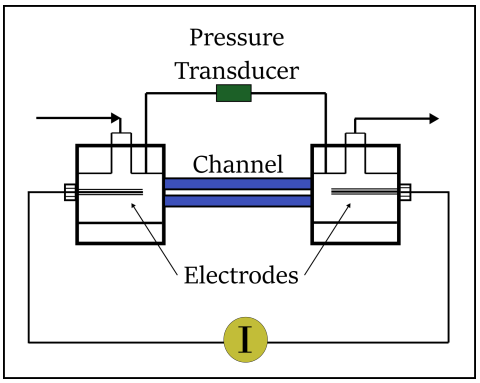

Figure 3.20: Schematic representation of a streaming current setup

The zeta potential of the substrates were obtained in milli-Q water as well as in 1 mM KCl solution. The measurement protocol is as follows: prior to the measurement, the desired electrolyte solution passes through the channel for a specific time to equilibrate the surface with the solution. Subsequently, the solution reservoir was filled with the desired electrolyte solution and the measurement started. pH and conductivity measurements were performed in a beaker next to the setup where the solution was titrated down by adding HCl.

Chapter 4

Impact of Surface Wettability on the Self-propulsion of Particles*

Abstract

The present chapter addresses the impact of slip length on the self-propulsion of thermophoretic Janus particles. Au-PS particles with a diameter of 2.4 µm move in close vicinity of three substrates with various water contact angles: bare glass, POEGMA-functionalized glass and silanized glass. Atomic force microscopy and contact angle measurements are employed to characterize the roughness and wettability of the substrates. The thickness of the POEGMA brush is obtained using ellipsometry as well as the nano-indentation method and the results are compared with each other.

The water contact angle of the bare glass and the brush-functionalized substrate are similar, whereas the contact angle of the silanized glass is significantly higher. This study shows that the hydrophilic properties of the substrate have no significant impact on the thermophoretic velocity of the particles and the particle reaches its maximum velocity near the brush-functionalized substrate.

*Similar content was presented by Tanja Pauly: Einfluss von Oberflächeneigenschaften auf die Bewegung aktiver Kolloide, Bachelor thesis, TU Darmstadt, 2018. The author of the present dissertation planned and supervised this bachelor thesis.

4.1 Introduction

In pursuit of an optimized motion of an active Janus particle near substrates, several parameters have been investigated. Apart from the numerous theoretical and experimental studies that have investigated the impact of parameters such as particle size,[56,134] particle shape,[135] fuel concentration,[136] patch size,[137] etc., only a few studies focused on the influence of the roughness, zeta potential, and slip length of the substrate on the velocity of the particles.

Holterhoff *et al.* found that the magnitude of the substrate's zeta potential could potentially affect the self-propulsion of diffusiophoretic microswimmers.[138] More specifically, they showed that SiO_2 particles half-coated with TiO_2 (SiO_2/TiO_2) exhibit an enhanced velocity near a substrate with reduced zeta potential. This is explained through the diminished local osmotic flow at the substrate/water interface underneath the particle. Moreover, they showed that the surface roughness leads to an increased velocity of the particle.

Furthermore, concerning the slip length of the substrate, Ketzetzi *et al.* reported that the diffusiophoretic velocity of catalytic colloidal swimmers is dependent on the slip length of the substrate.[70] They quantitatively examined the impact of substrates with various hydrophobicities on the velocity of 3-(trimethoxysilyl)propyl methacrylate (TPM) colloidal particles half-coated with platinum (Pt). It has been shown that upon increasing the hydrophobicity of the substrate, the slip velocity at the interface increases, hence particle velocity enhances. Moreover, they showed that the zeta potential of the substrate as well as its roughness has no dominant effect on the phoretic behavior of the particle.

Among these studies devoted to optimizing the motion of active particles near substrates, less attention has been given to the self-propulsion of thermophoretic particles near substrates with various hydrophilic properties. Inspired by the aforementioned research, this chapter aims to probe the thermophoretic behavior of Au-PS particles near substrates with various hydrophilic properties. Three samples were prepared: a bare glass, a poly(ethylene glycol)methacrylate (POEGMA) brush-functionalized glass, and a silane modified glass. The

physicochemical properties of the substrates are discussed in the following sections.

4.2 Results

4.2.1 Characterization of the POEGMA brush

The POEGMA-85 substrate was synthesized according to the procedure explained in section 3.2.1. "85" refers to the thickness of the brush in a swollen state. The thickness and refractive index of the brush in ambient conditions (relative humidity (r.h.)$\approx 30\%$) as well as in water was obtained by ellipsometry and is shown in Figure 4.1.

The thickness of the brush increases in the swollen state with a swelling ratio of 2. This is due to the fact that POEGMA bears ethylene oxide segments (repeating units = 5) as side chains which significantly enhances the hydrophilic properties of the brush. The refractive index of the brush decreases in the swollen state due to the presence of water (n = 1.33) which "dilutes" the polymer brush.

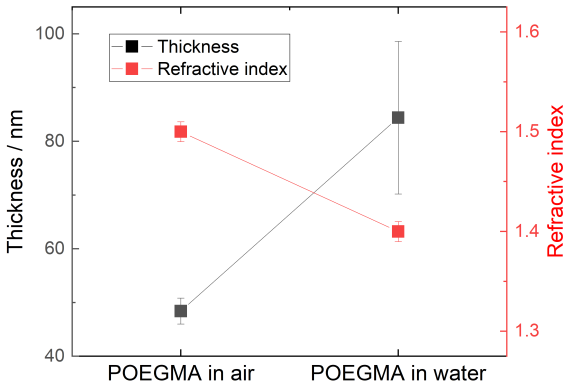

Figure 4.1: Thickness and refractive index of the POEGMA-85 brush in ambient conditions and in water measured by ellipsometry

AFM nano-indentation method was conducted as an alternative method to ellipsometry to determine the thickness of the brush. The force-indentation

curves in ambient conditions and Milli-Q water are shown in Figure 4.2. The contact point of the AFM tip with the brush is depicted by the symbols in the center of the curves, whereas the symbol on the right-hand side of the curves shows the contact of the tip with the substrate. The area between the two symbols on each curve corresponds to the indentation region. Upon analyzing this region, the thickness of the brush can be determined. A comparison of the brush thickness obtained by ellipsometry and nano-indentation method is provided in Table 4.1.

Table 4.1: Thickness of the POEGMA brush by ellipsometry and nano-indentation methods in dry and swollen states

	$\mathrm{d_{ambient}/nm}$	$\mathrm{d_{swollen}/nm}$
Ellipsometry	48.4 ± 2.4	84.4 ± 14.2
Nano-indentation	46.1 ± 3	77.1 ± 4.2

The results of the two independent methods are in good agreement with each other. This indicates that the full-indentation method was successfully applied to measure the thickness of the polymer brush.

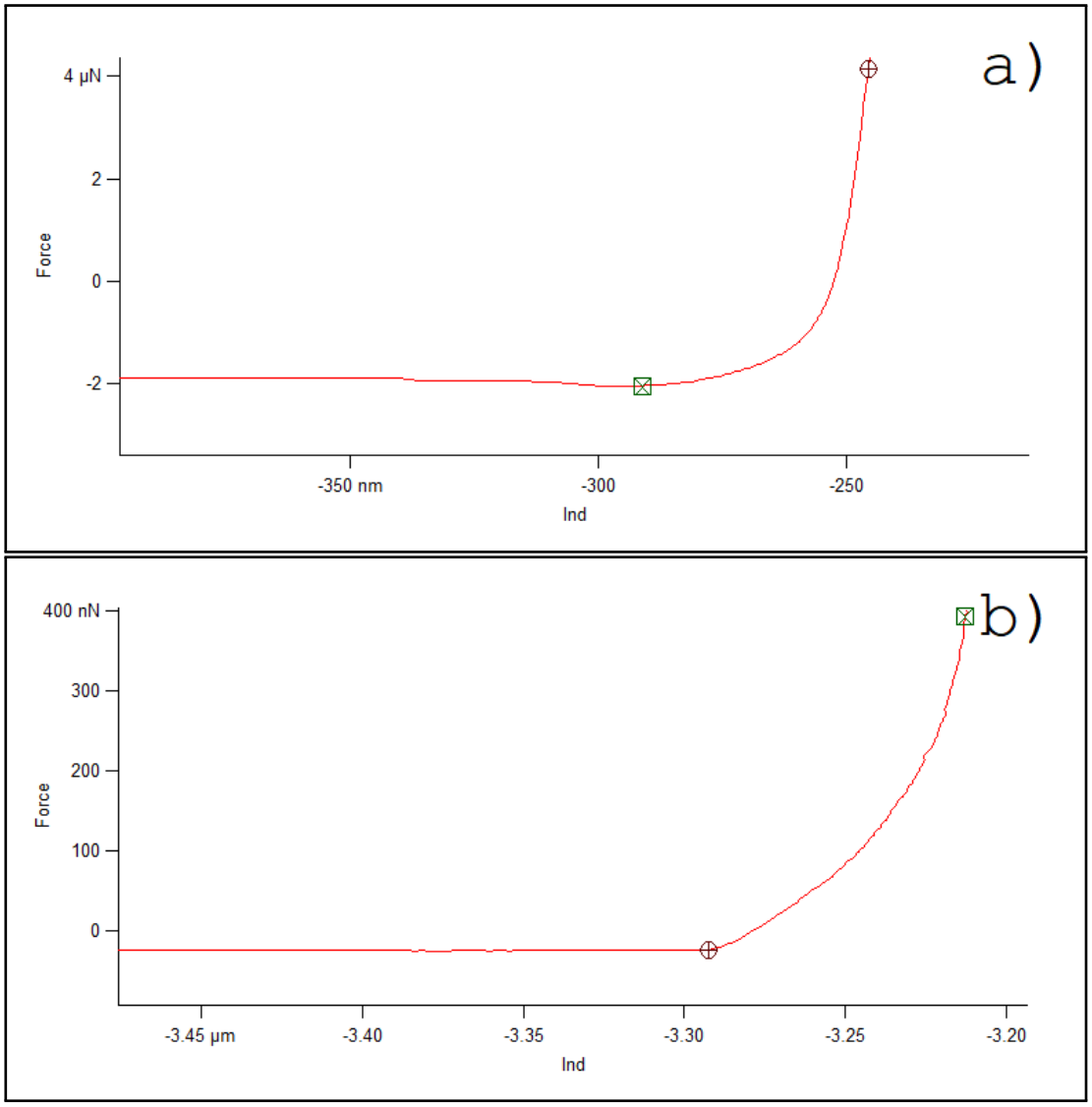

Figure 4.2: Force-Indentation curves of the POEGMA-85 brush in a) air and b) water at room temperature; The symbols on the left-hand side of the curves shows the contact point of the AFM tip with the brush, and on right with the silicon substrate

4.2.2 Physico-chemical properties of the substrates

Water contact angle: The contact angle of water (WCA) on the substrates is shown in Figure 4.3. Upon silanization, the contact angle of water on the coverslip glass increases significantly, whereas the WCAs on bare glass and POEGMA-functionalized glass are considerably lower. The results are in agreement with literature.[139]

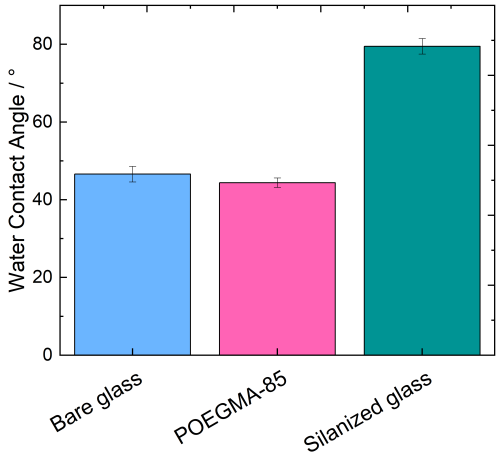

Figure 4.3: Static contact angle of water on the substrates

Glass substrates are hydroxylated surfaces that form a hydrogen bond with water molecules, hence the contact angle is low, $48°$. The contact angle of the POEGMA brush substrate is also similar to the bare glass which indicates that the brush substrate, due to the presence of ethylene oxide groups in its chemical structure, is highly hydrophilic.

The silanization treatment of the glass successfully yields a hydrophobic substrate with a water contact angle of $80°$. Upon this treatment, the hydroxyl groups of the substrate were functionalized with organosilane groups which have a hydrophobic nature. Hence, the water contact angle on the substrate increases.

Roughness: The surface topography of the substrates were obtained by conducting AFM in the scanning mode over the area of $5\,\mu m \times 5\,\mu m$. The micrographs are shown in Figure 4.4. The rms roughness of the substrates was determined by analyzing the height profile of the substrate on a sample area of $1\,\mu m^2$. The results are provided in Figure 4.5. The roughness of the POEGMA brush substrate increases once the brush is in its swollen state. Moreover, the roughness of the POEGMA substrate is relatively low both in ambient conditions and in water, which indicates the homogeneity of the brush layer and it is in agreement with the literature.[140]

The difference in the surface roughness of the POEGMA brush substrate and the bare glass is not very pronounced, whereas the silanized substrate expresses

the highest roughness with relatively high error values. This could originate from the non-uniform self-assembly of silane monolayer on the glass substrate resulting from the contaminants that are not completely removed in the cleaning procedure prior to the silanization treatment.[141]

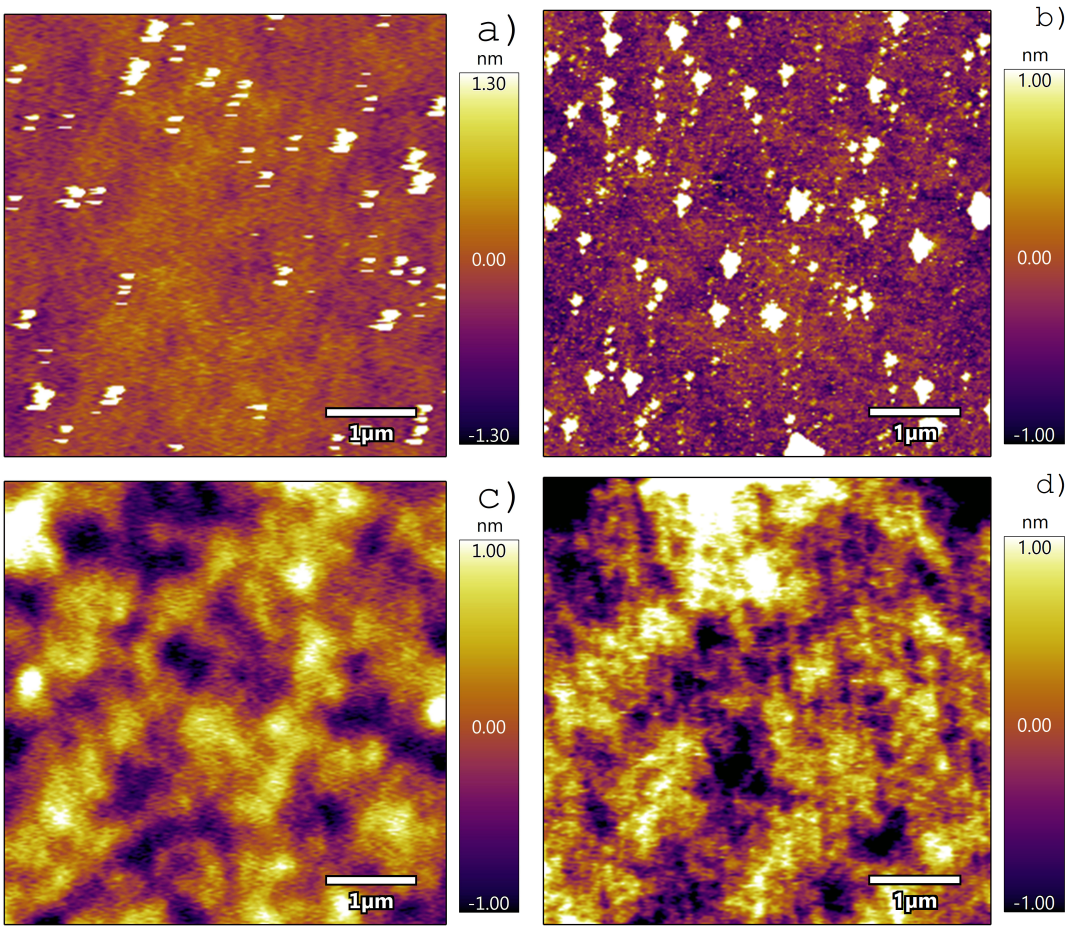

Figure 4.4: Surface morphologies of the substrates obtained by AFM in the scanning mode, a) the bare glass, b) the silanized glass, c) the POEGMA-85 in air, and d) the POEGMA-85 in water at room temperature

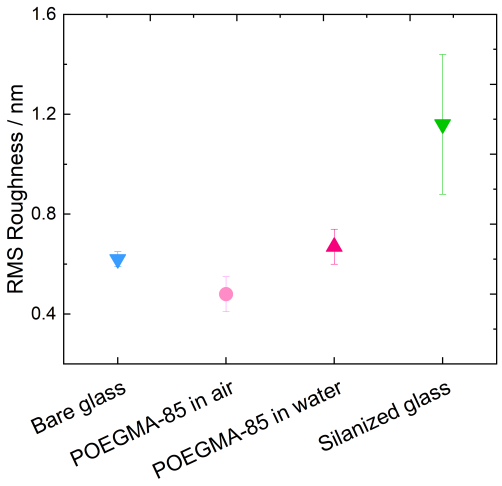

Figure 4.5: RMS roughness of the substrates, the error bars represent the standard deviation obtained by measuring on three substrates and at 5 different spots with an area of 1 µm × 1 µm on each substrate

4.2.3 Self-propulsion of the Au-PS particle near the substrates

The preparation of sample cell for the self-propulsion tests is discussed in chapter 3, section 3.1.1.6. Upon obtaining the position of the particle in every single frame, trajectories of the particle are produced. The thermophoretic velocity of the particle has been obtained through fitting the MSD curves with equation 4.1 for $t \ll \tau_{\mathrm{r}}$, where D is the diffusion coefficient of the particle, v_{th} is the thermophoretic velocity of the particle, and t is the lag time.

$$MSD = 4Dt + v_{th}^2 t^2 \tag{4.1}$$

τ_{r} is the rotational diffusion time of the particle and for a particle with a diameter of 2.4 µm was calculated to be 10 s in bulk. Therefore, the MSD curves were fitted up to $t \approx 1$ s, which is well below the rotational time of the particle. The trajectories of the Au-PS particles with a diameter of 2.4 µm as well as the MSD curves are presented in Figure 4.6.

The particle undergoes a Brownian motion when the laser beam is off. Its motion is purely diffusive, random, and without any specific direction. Therefore, the trajectory of the particle at P=0 mW is rather coiled and does not exceed an

area of 0.5×0.5 μm^2. The MSD curve of the particle increases linearly with time under no laser illumination conditions.

The trajectories of the particle under laser illumination differs from the ones without laser illumination. The particles exhibit a directed motion, where their overall displacement depends on the laser intensity. The higher the laser intensity, the larger the distance that particle can travel without changing its direction. The MSD increases non-linearly with time, which indicates the deviation of active motion from the Brownian motion. Moreover, it can be seen that the MSD of the particle near the POEGMA substrate is at maximum, whereas the MSD near the bare glass and the silanized substrate are lower and relatively similar.

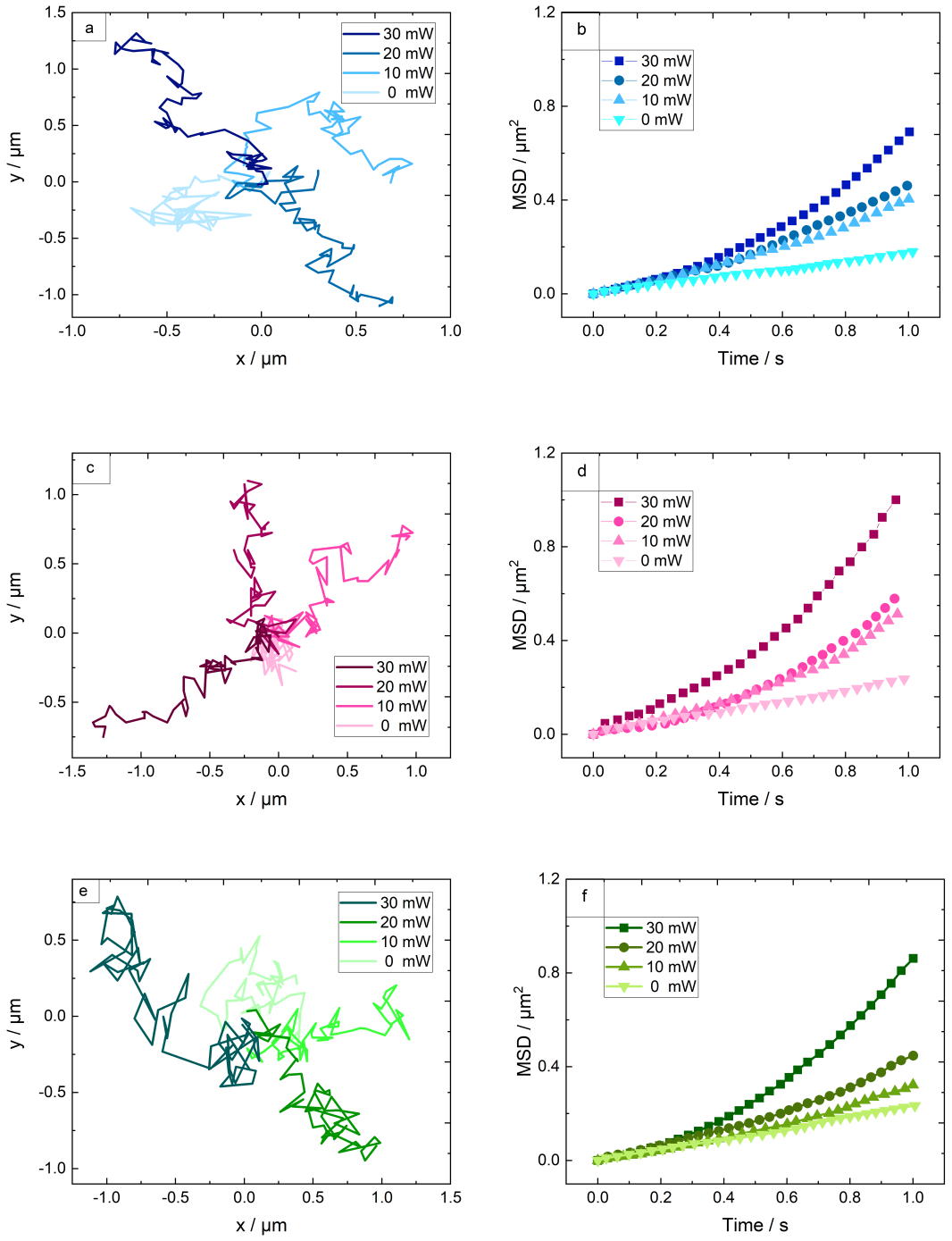

Figure 4.6: The trajectories and MSD curves of the Au-PS particle with a diameter of 2.4 µm within 1 s well below the rotational time of the particle $\tau_r = 10$ s near a&b) bare glass, c&d) POEGMA-85 and e&f) silanized glass, respectively

The MSD curves were further analyzed using equation (4.1), and the thermophoretic velocities, as well as the diffusion coefficients of the particles, were obtained. The results are shown in Figure 4.7. The results are the mean value of at least 20 measurements on various particles and the error bar represents the standard deviation of the data.

Figure 4.7a shows that the velocity of the particle increases upon increasing the laser power. Moreover, the Au-PS particle exhibits an enhanced velocity near the POEGMA-85, whereas its velocity near the bare and silanized glass is lower.

The diffusion coefficients of the particle near the bare and the silanized glass remain nearly unchanged, as it has also been observed in literature.[40] However, it slightly increases near the POEGMA-85. Furthermore, the diffusion coefficients of the particle confined between the substrates are considerably lower than the diffusion coefficient of the particle in bulk due to the presence of the wall, Figure 4.7b.

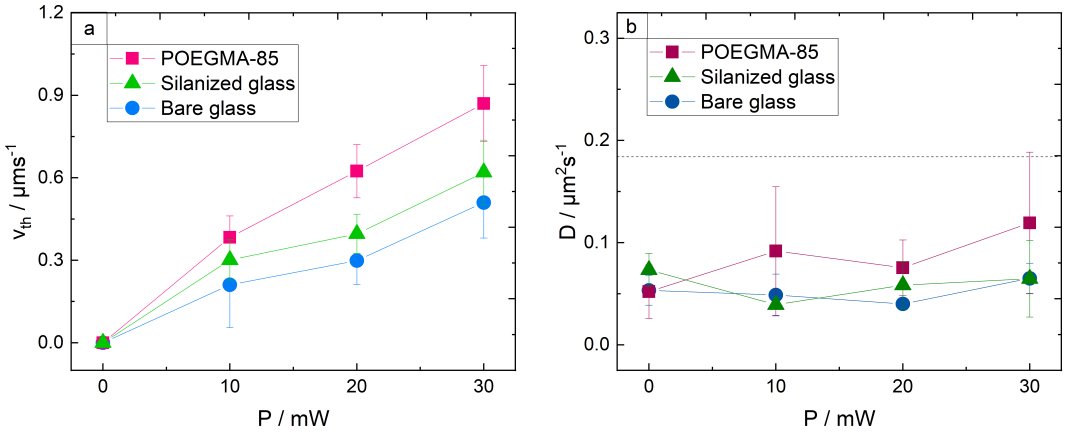

Figure 4.7: a) Thermophoretic velocity and b) diffusion coefficient of the Au-PS particles with a diameter of 2.4 µm near three various substrates; dashed line represents the diffusion coefficient of the particle in bulk

4.3 Discussion

Silanization treatment alters the wetting properties of the glass substrate and renders the substrate hydrophobic. Hydrophobized substrates are known to increase the boundary slip and reduce the fluid drag between solid and liquid adjacent to the solid substrate. The slip length is the distance below the substrate at which the slip extrapolates to zero, Figure 2.3, and it can be measured by using AFM. Analyzing hydrophobized substrates in contact with water using various methods such as AFM,[142] XRR,[143] and neutron reflectometry[144] has revealed the presence of air bubbles at their surface.[145,146] These bubbles formed during the wetting process, have a size range of a few nm to several microns, and are stable over a long period of time (over 20 h).[147] The so-called nanobubbles are believed to be responsible for the boundary slip by reducing the friction between the fluid and the solid at the solid-liquid interface.[148]

Moreover, upon silanization of the glass, the slip length of the substrate increases. Hence, the particle velocity enhances compared to the particle near the bare glass, Figure 4.7a. However, the velocity enhancement is not as pronounced as reported by Ketzetzi *et al.*[70] It is worth mentioning that the water contact angle of the hydrophobized substrate in their case was $120°$, whereas the WCA of the silanized glass in our case was $80°$. The more hydrophobic is the surface, the larger is the slip length, hence the velocity of the particle near the surface is higher.

The silanized glass expresses the highest contact angle, whereas the contact angle of the glass and the POEGMA substrate is $45°$. However, The Au-PS particles move fastest near the POEGMA-85 substrate in comparison to the silanized glass and the glass. This indicates that the hydrophobicity of the substrate is not the only important parameter and more interfacial parameters need to be examined. The silanized glass expresses the highest roughness amongst the substrates. The high roughness could originate from the presence of nanobubbles at the surface as well as the inhomogeneities in the silane monolayer at the interface. Consequently, the combination of the higher slip length at the interface as well as the high roughness resulted in an intermediate velocity of the particles near the silanized glass.

4.4 Conclusion

In this chapter, the thermophoretic velocity of the Au-PS particle with a diameter of 2.4 μm near substrates with various hydrophilic properties was investigated. Due to the silanization of the glass, the WCA increases significantly. However, the velocity of the particle did not enhance dramatically as expected according to literature.[70] The silanization increases the slip velocity of the fluid at the interface, hence the particle moves faster compared to the bare glass. Moreover, the higher roughness of the silanized glass compared to the POEGMA-85 is responsible for the lower velocity of the particle near the silanized glass. The Janus particles displayed their highest thermophoretic velocity near the POEGMA-functionalized substrate. Therefore, the following chapter is devoted to unravel the impact of a brush substrate on the self-propulsion of particles in a systematic fashion.

Chapter 5

Self-propulsion near PNIPAM-functionalized Substrates*

Abstract

The present chapter reports a study on the self-propulsion of Janus particles near PNIPAM-functionalized substrates. The PNIPAM-functionalized substrates were characterized extensively. Ellipsometry measurements provide detailed information on the swelling and collapsing of the brush substrate, while X-ray reflectometry as well as AFM studies determine the thickness and roughness of the substrates, respectively. Au-PS Janus particles were brought into close vicinity of the PNIPAM-functionalized substrates, where their self-propulsion kicks off upon laser irradiation. The results are compared with the case where the particle self-propels near the bare glass and the impact of interfacial parameters are discussed. The results display an enhanced thermophoretic velocity of the particle near the PNIPAM-functionalized substrates. This phenomenon is explained by considering the influence of the thermo-osmotic flow at the glass/water interface and how modification of the substrate with brushes suppresses the strength of the thermo-osmotic flow, hence the particle velocity increases. Next, the impact of brush thickness is discussed. The results reveal an enhancement in particle velocity close to the thinner brush. It has been attributed to the lower roughness and friction of the thinner brush.

*Similar content was presented in M. Heidari, S. Muiños Landin, A. Bregulla, F. Cichos, and R. von Klitzing, *Langmuir*, **2020**, 36, 7775-7780.

5.1 Introduction

Theoretical and numerical studies have shown that the physicochemical properties of the substrate could potentially lead to an increase or decrease of the swimming velocity of the particle.[52,73,149,150] Few experimental studies have also investigated the impact of the substrate on the propulsion of self-diffusiophoretic particles.[70,72] Despite using similar particles under the same experimental conditions, studies have obtained various results in terms of particle velocity.[55,151] This observed discrepancies could potentially originate from the interfacial properties of the substrate. Therefore, further studies are required to gain in-depth knowledge about the correlation between thermophoretic particles and substrate.

In this chapter, the interaction between thermophoretic Au-PS Janus particles and PNIPAM brush substrate/glass is addressed. The influence of the substrate functionalized with the hydrophilic PNIPAM brush as well as the thickness of the brush on the self-propulsion of Janus particles are investigated. Au-PS particles with various surface functionalities were chosen to examine the impact of surface charges on the thermophoretic behavior of the particle. The results provide useful guidelines for the design of a new substrate for the self-propulsion tests.

5.2 Results

5.2.1 Characterization of PNIPAM brush substrates

PNIPAM brushes were synthesized through grafting from technique. The thickness of PNIPAM brushes on silicon substrates in air and water were measured by ellipsometry.

To obtain a general overview of the characteristics of PNIPAM brushes, three brushes with various thicknesses were synthesized to investigate their phase transition behavior upon increasing temperature in water. The impact of polymerization time on the swelling behavior of the brush was also investigated.

The thickness and refractive indexes of the PNIPAM brushes are shown in Table 5.1.

Table 5.1: Thickness and refractive index of PNIPAM samples in ambient conditions ($22°C$, 32% r.h.). All samples were prepared on silicon substrates

Sample name	Polymerization time /min	Ambient thickness /nm	Refractive index n
PNIPAM-1	15	54.2 ± 1.5	1.52 ± 0.08
PNIPAM-2	60	78.4 ± 1	1.48 ± 0.07
PNIPAM-3	180	140.5 ± 2.3	1.39 ± 0.12

The longer the polymerization time, the thicker the brush. Moreover, the thicker brush represents a lower refractive index, whereas the refractive index of PNIPAM-1 and PNIPAM-2 is the same.

Figure 5.1 displays the temperature-dependent behavior of the PNIPAM brushes in Milli-Q water as well as their swelling ratio with respect to their initial dry thicknesses. Surface grown PNIPAM brushes collapse over a range of temperature. The solid black line represents the sigmoidal fit to the measured thicknesses.

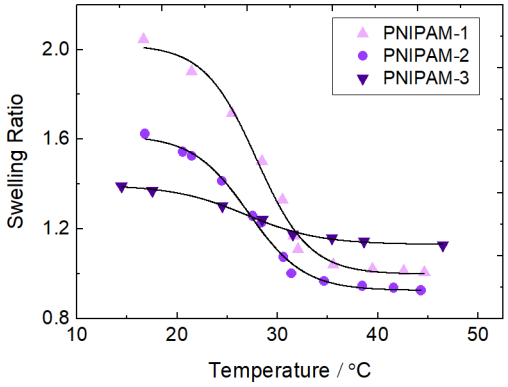

Figure 5.1: Temperature-dependent volume phase transition of the PNIPAM brushes in Milli-Q water measured by ellipsometry

The swelling ratio of the PNIPAM brushes was calculated according to equation 5.1.

$$\text{Swelling ratio} = \frac{d_{\text{swollen}}}{d_{\text{amb}}} \tag{5.1}$$

where d_{swollen} is the thickness of the brush in the swollen state and d_{amb} is the thickness of the brush in ambient conditions $(22°\mathrm{C}, 32\%$ r.h.$)$. As shown in Figure 5.1, all PNIPAM brushes collapse upon increasing temperature. However, this transition occurs gradually rather than a sharp coil-globule transition as observed for polymer brushes in bulk. Furthermore, Figure 5.1 shows that the swelling ratio of the brush depends on its thickness. The PNIPAM-1 sample with the lowest thickness swells by a factor of 2 at low temperatures, whereas the swelling ratio of the PNIPAM-3 with the highest thickness is 1.4 fold. Upon increasing the temperature from 25 to 35°C, the swelling ratio exhibits a onefold decrease for the thinnest brush, whereas it only drops by a factor of 0.2 for the thickest brush.

For the self-propulsion measurements, a new set of PNIPAM brushes on glass substrates were synthesized. These brushes were characterized by X-ray reflectometry and AFM-scratching methods. The specifications of the techniques are reported in Chapter 3. Table 5.2 reports their thickness and refractive index of the brushes in ambient conditions $(22°\mathrm{C}, 32\%$ r.h.$)$ and swollen states.

Table 5.2: Thickness and refractive index of the PNIPAM brushes used for self-propulsion measurements

Sample	$d_{\mathrm{amb}/nm}$	$d_{\mathrm{swollen}/nm}$	$\mathrm{rms}_{\mathrm{amb}}/\mathrm{nm}$	$\mathrm{rms}_{\mathrm{swollen}}/\mathrm{nm}$
PNIPAM-140	45 ± 2	140 ± 5	0.6 ± 0.1	0.8 ± 0.1
PNIPAM-190	140 ± 6	190 ± 6	1.4 ± 0.2	2.1 ± 0.4
PNIPAM-300	220 ± 4	300 ± 9	0.9 ± 0.1	1.2 ± 0.1

The thickness of the PNIPAM brushes grown from glass in ambient conditions was obtained from the AFM-scratch method. Figure 5.2 shows the height image of the PNIPAM-140 in ambient conditions.

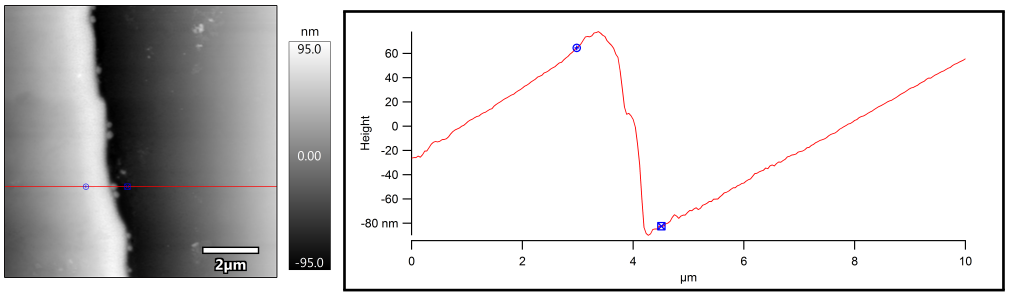

Figure 5.2: left) AFM height image of the scratched PNIPAM-140 brush substrate in ambient conditions, right) the cross-section of the image, the jump displays the scratched border

As the PNIPAM brushes were grown from glass substrates, the best way to acquire information about their thicknesses was to conduct X-ray reflectometry in ambient conditions. The reflectivity curves are reported in Figure 5.3. The thickness of the brushes was calculated according to equation 3.15.

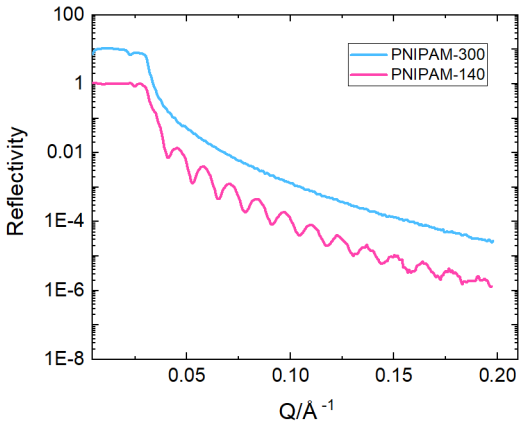

Figure 5.3: X-Ray reflectivity curves of PNIPAM-300 and PNIPAM-140 in ambient conditions

The results of XRR measurements are compared with the ones obtained from the AFM scratch method, Table 5.3. As the results are similar, it can be concluded that AFM scratch method can be successfully applied to determine the thickness of the brushes grown from a glass slide.

Table 5.3: Comparison of brush thicknesses obtained by XRR and AFM-scratch in ambient conditions ($22°$C, 32% r.h.)

Sample	d_{amb}/nm (XRR)	d_{amb}/nm (AFM- Scratch)
PNIPAM-140	45 ± 2	50 ± 9
PNIPAM-300	220 ± 4	198 ± 6

5.2.2 Self-propulsion of Au-PS Janus particles near PNIPAM brush substrates: Impact of the substrate

The procedure of the self-propel measurements is explained in Chapter 4, section 4.2.3. Figure 5.4 shows the experimentally obtained mean-squared displacement (MSD) as well as thermophoretic velocities of a single Janus particle functionalized with -COOH near a bare and a PNIPAM-functionalized substrate. The thickness of the swollen brush is 190 nm in water.
To prepare the cell for the self-propulsion tests, 0.5 µL of the Au-PS Janus particle dispersion in water was deposited between two bare/brush-functionalized glass slides. The edges of the glass were covered with silicon paste as a spacer. The presence of a spacer is inevitable in order to keep the movement of particles in 2D. Moreover, it prevents the evaporation of water inside the cell. The cell was placed on top of the objective. Self-propulsion tests were started by switching on the laser.

The thermophoretic velocity of the particle has been obtained through fitting the MSD curves with equation 4.1, below the rotational diffusion time of the particle which for a particle with a diameter of 1 µm was calculated to be 0.7 s in bulk. The experimentally measured values of the rotational diffusion time of the Au-PS-COOH particle near the bare glass and the PNIPAM-190 at 25 mW are 0.35 s and 0.3 s, respectively. At longer time scales ($t \gg \tau_r$), the motion of the particle becomes diffusive and deviates from the pure self-propulsion and MSD increases linearly with t, the black line in Figure 5.4a. Therefore, the MSD curves were fitted up to $t \approx 0.2$ s, which is below the rotational time of the particle, Figure 5.4b. The duration time of each measurement was set to 1.5 s.

As the most important novel finding, the data reveal an enhanced thermophoretic velocity of the particle near the PNIPAM-functionalized

substrate in comparison with the bare glass slide, Figure 5.4c. Particle velocity increases as well upon increasing the laser intensity. Each point in Figure 5.4c is attributed to the average of five separate Au-PS particles, each particle measured at least 3 times.

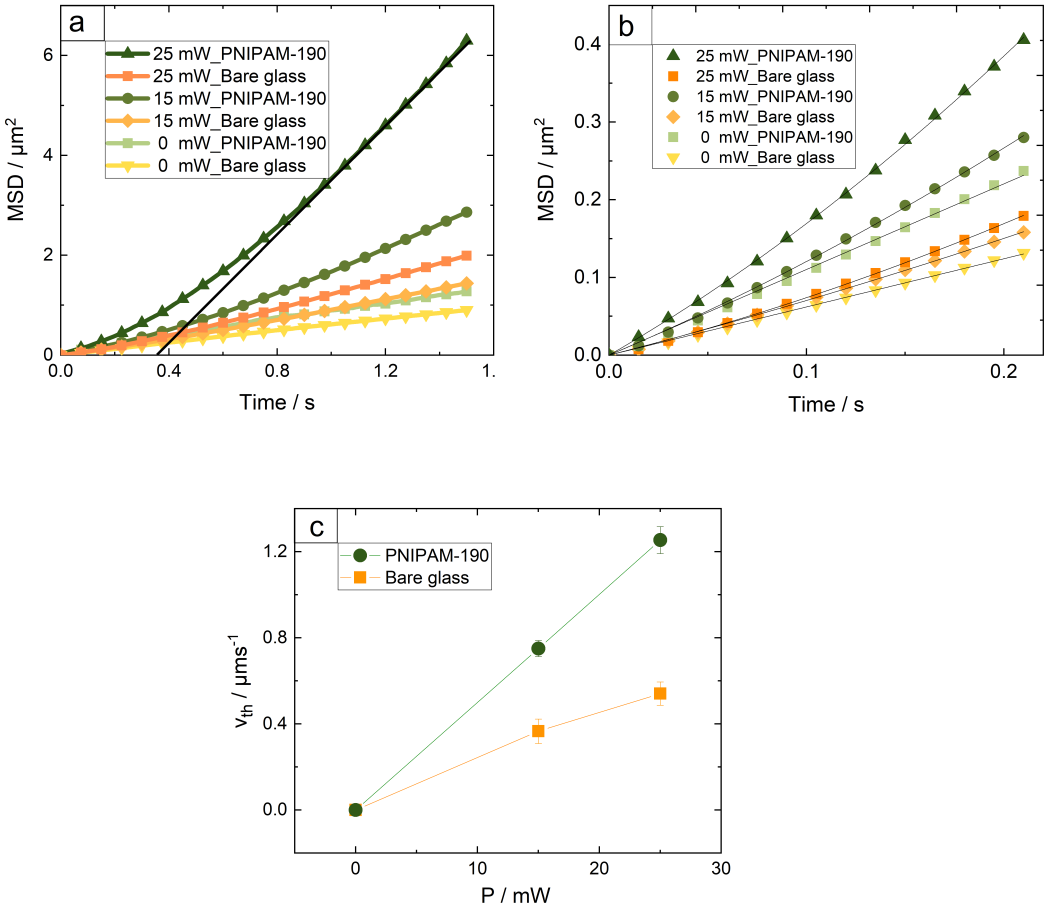

Figure 5.4: a) Typical mean-squared displacement (MSD) curves from a single measurement; solid black line represents the linear and diffusive behavior of the particle at longer time scales $t > \tau_r$, where the particle movement becomes diffusive. b) MSD of a single Au-PS-COOH particle at short times; solid black lines represent the fit to the curves. c) Average thermophoretic velocity of Au-PS-COOH Janus particles near a bare glass slide and a PNIPAM-functionalized substrate with a thickness of 190 nm (PNIPAM-190) in water under various laser intensities

5.2.3 Self-propulsion of Au-PS Janus particles near PNIPAM brush substrates: Impact of the brush thickness

To further investigate the role of brush substrate, two additional brushes with a lower and higher thicknesses were synthesized: 140 nm and 300 nm in the swollen states. Here, Au-PS particles were used without any -COOH functionalization. The rms roughness of the PNIPAM-140 and PNIPAM-300 in the swollen state was achieved from atomic force microscopy micrographs of 1×1 µm^2, and the values are 0.8 ± 0.1 nm and 1.2 ± 0.1 nm, respectively.

Figure 5.5 shows that variation of brush chain length has a great influence on the self-propulsion velocity of the Janus particles. According to Figure 5.5b, v_{th} decreases with increasing brush chain length. However, it is noticeable that the thermophoretic velocity does not increase linearly with laser power as expected.

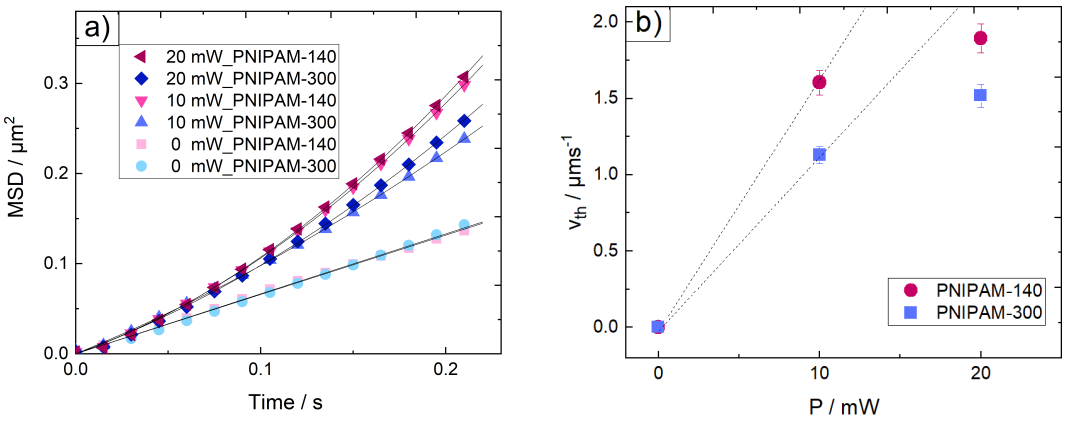

Figure 5.5: a) Mean-squared displacement and, b) thermophoretic velocity of Au-PS Janus particles under various laser intensities near PNIPAM brush substrate with 140 nm and 300 nm thickness in water; solid black lines represent the fit to MSD curves and dash lines represent the expected linear increase of the thermophoretic velocity with laser power

Diffusion coefficients of the Au-PS particle near the bare glass, PNIPAM-190, PNIPAM-140, and PNIPAM-300 are shown in Figure 5.6. The values are compared with the calculated diffusion coefficient of the particle in bulk. This figure shows that the diffusion coefficients of the particles near the substrates are

considerably lower compared to the diffusion coefficient of the particle in bulk. Furthermore, the diffusion coefficient of the particle near PNIPAM-190 increases upon increasing the laser power, whereas D displays a non-monotonous behavior in Figure 5.6b.

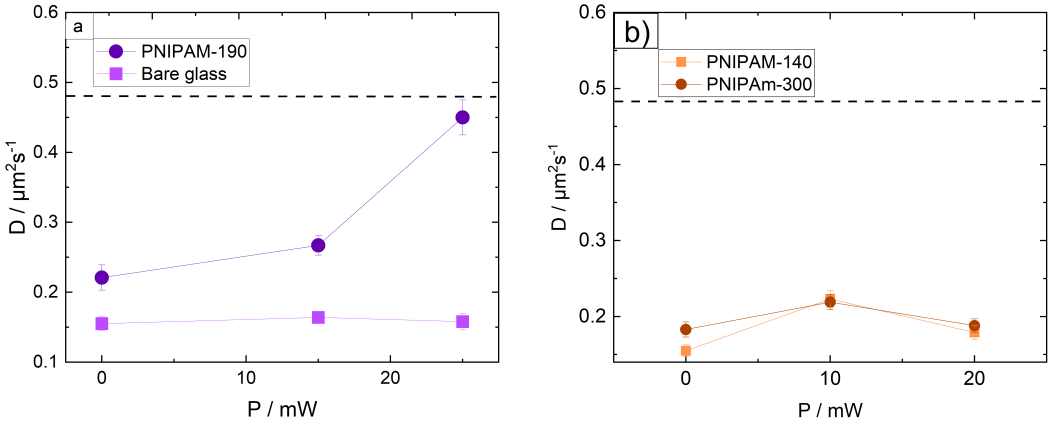

Figure 5.6: Diffusion coefficients of the a) Au-PS-COOH particle near the bare glass and PNIPAM-190, b) Au-PS particle near PNIPAM-140 and PNIPAM-300 under various laser intensities, the dashed lines represent the calculated diffusion coefficient of the particle in bulk

5.3 Discussion

Characteristics of the PNIPAM brush substrates

The gradual collapse of surface tethered PNIPAM brushes over a wide range of temperature has already been observed by means of neutron reflectivity measurements[152] and surface plasmon resonance.[153] This is in contrast to the sharp collapse of PNIPAM brush in bulk.[154] The origin of this broad temperature range is discussed in literature. The LCST is dependent on the polymer concentration.[155] Since the density of polymer brush gradually decreases by moving away from the substrate,[156] different parts of the brush collapse at different temperatures, hence forming a wider collapse.[157] It has also been claimed that the gradual collapse of the brush is not a first order phase transition.[158,159] However, this statement is contradicted by other researchers

where they argue that it is normal for finite sized systems to express a smeared phase transition temperature range.[160]

The swelling ratio of the surface grafted PNIPAM brushes indicates that under good solvent conditions the thicker brush swells less compared to the thinnest brush. Moreover, the thermal response of the brush is also highly affected by the brush thickness. In a model described by Wagner *et al.* a surface grafted polymer brush is more densely packed near the substrate and diluted near the ends of the polymer brush.[161] Therefore, it is harder for the molecules of the good solvent to penetrate the high density regime of polymer brushes. As the thickness of the densely packed layer near the substrate is higher in case of the thicker brush, its swelling ratio is lower compared to the thinner brush, and its thickness will be less affected by the temperature.

Self-propulsion near the PNIPAM brush substrates

To understand the mechanism by which a brush-functionalized substrate facilitates the self-propulsion of the particle, it is inevitable to consider the flow boundary conditions and thermo-osmotic slip at the solid substrate.[75] Upon laser irradiation, the local generated heat at the surface of the Au-PS particle transfers to the glass slides near the particle. The occurrence of a temperature gradient within the glass slides leads to excess hydrostatic pressure at the cold side of the glass which subsequently leads to a counteracting flow of charged liquid from the cold side toward the hot side, Figure 5.7. This phenomenon is called thermo-osmosis,[98] and the generated flow at the interface is called thermo-osmotic flow. These two thermo-osmotic flows at the boundary layer exert an additional torque on the self-propelling particle which makes the particle and consequently its velocity vector tilt toward the substrate. The x component of the velocity vector, v_x, is parallel to the substrate and counts for the displacement of the particle. Since it is smaller than v, the particle velocity decreases.

In Figure 5.7 only one glass slide is shown as the particle, due to gravity, is in close proximity of the substrate underneath it.

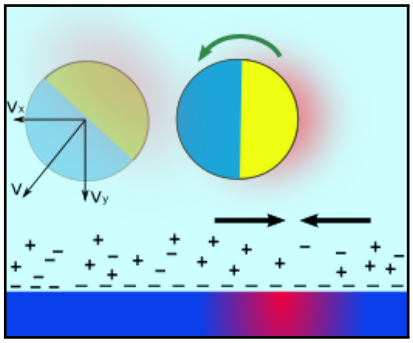

Figure 5.7: Asymmetric distribution of ions at the glass/water interface formed due to the temperature gradient within the glass slide, leads to the generation of two thermo-osmotic flows at the interface from the cold side towards the hot side which subsequently makes the particle tilt towards the substrate; hence, its velocity decreases

Impact of the substrate

To compare the degree of thermo-osmotic flow at the glass/water interface with that at the brush/water interface, several interfacial parameters such as strength of the water-substrate coupling, impact of the electric double layer at the interface, and the hydrophilicity/hydrophobicity of the substrate and its roughness should be taken into account.

The water contact angles on the bare glass and PNIPAM-190 at room temperature are comparable, and the values are $51^\circ \pm 2^\circ$ and $54^\circ \pm 4^\circ$, respectively. Hence, the slip length dependent behavior of the particles with respect to the hydrophobicity of the substrate can be ruled out in this case. Upon functionalization of the glass substrate with nonionic PNIPAM brushes, the surface charge and therefore the ion concentration within the electric double layer at the interface is reduced significantly. Subsequently, a lower amount of ions will contribute to the thermo-osmotic flow at the brush/water interface. Therefore, tilting of the particle toward the substrate is less likely; thus, the particle exhibits higher velocity.

In contrast to the brush/water interface, the thermo-osmotic slip at the glass/water interface is somewhat different. The higher amount of ions available at the glass/water interface plays a significant role in the formation of thermo-osmotic flow. As a result, the thermo-osmotic flow at the glass/water interface is stronger, and particle tilting is more likely than at the brush/water

interface; hence, the particle is more strongly affected by the interfacial fluid flow, and subsequently, its velocity decreases.

It is noteworthy that the thermophoretic velocity of a single Au-PS particle near bare glass reported here deviates from the results shown by Bregulla et al.[56] It should be pointed out that the velocities strongly depend on the surface properties of the particle defining the particle solvent interactions. Additional components in the system will always adsorb to the particle surface and change the interfacial interactions and thus also the thermophoretic velocity. The cleaning procedure of the glass substrate or the pH of the deionized water could originate the different values.

Impact of the brush chain length

Figure 5.5b shows that variation of the brush chain length has a great influence on the self-propulsion velocity of the Janus particles. This figure shows that v_{th} decreases with increasing brush chain length. In contrast, the measurement in Figure 5.4c shows that the thermophoretic velocity of the particle increases upon functionalizing the substrate with polymer brushes. This means that there are two counteracting effects: the already mentioned thermo-osmotic flow and a second mechanism. To unravel this mechanism, it is necessary to investigate the conditions at the outermost layer of the PNIPAM brush at the brush/water interface.

All brushes exhibit thicknesses above 100 nm in their swollen states, which is the thickness of the Debye length at the glass/water interface, where the ionic strength of deionized water is 10^{-5} M. Since PNIPAM is a neutral polymer, the contribution of ions and hence the formation of thermo-osmotic flow at the brush/water interface is assumed to be negligible. The only difference between these two samples which could cause the velocity difference is the roughness. The results show that the roughness increases with increasing brush chain length. This is in excellent agreement with the previously reported nature of brushes.[77] Furthermore, friction force microscopy (FFM) studies show that the friction coefficient between a gold-coated probe and a brush-functionalized substrate increases with increasing brush thickness for nonionic brushes.[162] Hence, the combination of a lower roughness and friction leads to higher particle velocity near the thin brush.

Figure 5.5b shows that the thermophoretic velocity of the Janus particle increases with increasing laser power. However, the velocity does not increase linearly with laser power as expected. This could be attributed to the fact that upon increasing laser power, the local generated heat around the particle is enough to make the PNIPAM substrate undergo a conformational transition from the highly swollen state to a semi collapsed state. Such a transition gives rise to the adhesion force[163] between the brush outermost layer and the particle which subsequently influences the particle self-propulsion. Hence, the particle velocity deviates from its expected value at P=20 mW. It is worth mentioning that the particle in Figure 5.4c shows a lower thermophoretic velocity near PNIPAM-190 in comparison with the particle in Figure 5.5b. This could be due to the fact that the particle in Figure 5.4c was functionalized with -COOH groups, and the presence of these groups on the surface of the particle gives rise to a stronger surface charge which potentially decreases the effective boundary slip at the particle/water interface;[164] hence, the thermophoresis will be less effective compared to the particle with no surface functionalization.

Figure 5.6 shows that the diffusion coefficients of the particles near the substrates are considerably lower compared to the diffusion coefficient of the particle in bulk. This hindered translational diffusion coefficient of the particle near substrate is in good agreement with the literature,[165,166] and it is due to the boundary conditions at the wall as well as the electrostatic interactions between the particle and the wall which acts upon the particle and hinders its translational diffusion coefficient.

The diffusion coefficient of the particle near PNIPAM-190 increases upon increasing the laser power, whereas D displays a non-monotonous behavior in Figure 5.6b. It is worth mentioning that the water-particle interactions strongly influence the dynamics of the particle as well as the heat exchange between the particle and water. Therefore, the functionalization of the particle with -COOH could lead to variations in the temperature profile and viscosity of the water around the particle and originate such different behaviors in D.

5.4 Conclusion

The thermophoretic motion of a single Janus particle near a brush-functionalized substrate was studied experimentally. The results demonstrate a strong influence of the confining substrate on the self-propulsion of an active colloidal particle. The findings lead to two main conclusions for the present work. First, upon functionalization with PNIPAM brushes, the thermophoretic velocity of the particle is enhanced. Second, the particle velocity can be tuned upon varying the brush thickness. The velocity decreases upon increasing the brush thickness, where roughness is higher as well. These observed phenomena can be explained by considering the role of thermo-osmotic flow within the electric double layer at the glass (brush)/water interface. Generation of such flow hinders the particle motion, gives rise to particle tilting toward the substrate, and hence decreases the particle velocity. The fact that two counteracting impacts (thermo-osmotic flow and surface roughness) influence the self-propulsion leads to the assumption that there is a certain brush thickness where the thermophoretic velocity reaches a maximum. The strength of the thermo-osmotic flow can be decreased by functionalizing the substrate with polymer brushes. However, substrate properties at the brush/water interface together with brush roughness play crucial roles as well. To obtain a more detailed understanding of the impact of the interfacial properties of the substrate and how these properties impact the particle self-propulsion, the next chapter is devoted to brushes with a range of thicknesses. However, to avoid any unwanted velocity decrease or attachment of the particle during laser illumination, the focus is only on the self-propulsion of particles near brush substrates without temperature-dependent behaviors.

Chapter 6

Self-propulsion near POEGMA/ PHEMA-functionalized Substrates

Abstract

In the present chapter, the substrates are functionalized with POEGMA and PHEMA brushes of varying swelling properties, grafting densities, and thicknesses to systematically modify and explore the substrate-swimmer interactions. Notably, the swimming speed is essentially controlled by the brush thickness and can vary by a factor of up to three. Remarkably, the swimming speed which we measure depends non-monotonously on the brush thickness, leading to a distinct speed maximum at an intermediate brush thickness. The emergence of the speed-maximum is explained by a competition of surface-charge induced substrate flows, which slow down the swimmer, but systematically decrease as the brush thickness increases, and a competing slow-down of the swimmers with increasing surface roughness.

6.1 Introduction

Chapter 5 reported that the functionalization of the substrate with PNIPAM can enhance the thermophoretic velocity of Au-PS Janus particles compared to bare glass.[57] While this study gives an indirect hint regarding the influence of brush thickness on the particle speed, it leaves important aspects of the precise mechanism controlling the particle speed open. In particular, PNIPAM exhibits

a lower critical solution temperature (LCST) of $\approx 32°$C in water which might allow nearby thermophoretic swimmers to locally trigger a phase transition resulting in PNIPAM-specific microswimmer-wall interactions. Therefore, an understanding of the precise mechanism through which walls control the speed of (thermo)phoretic microswimmers calls for novel experiments which (i) allow for a systematic variation of the physical and chemical properties of the substrate and (ii) do not show a LCST in the relevant temperature regime.

To achieve this, in this chapter, hydrophilic brushes of poly(ethylene glycol)methacrylate (POEGMA) and poly(2-hydroxyethyl methacrylate) (PHEMA) with various thicknesses are synthesized. The two brushes, POEGMA and PHEMA, substantially differ regarding their refractive index, grafting density and the resulting surface roughness and help us to test the generic character of the analyzed substrate-wall interactions. In addition, unlike the previously used PNIPAM brushes, they do not show a LCST in the relevant temperature regime which allows us to exclude possible contributions due to a phase-transition within the brush on the speed of the microswimmers.

6.2 Results

6.2.1 Characterization of POEGMA and PHEMA brush substrates

Thickness and roughness: The thickness and roughness of the polymer brushes were determined by ellipsometry and atomic force microscopy measurements, both in ambient conditions and swollen states. The results are shown in Figure 6.1a,b, respectively. The rms roughness of the brushes in water was determined by the AFM height scan. The polymerization time of POEGMA samples 1-4 is 15, 30, 45, and 60 minutes, whereas the PHEMA samples 1-4 were synthesized in 1, 2, 3, and 4 hours, respectively. From each polymer (POEGMA or PHEMA) four brush functionalized samples with various thicknesses were synthesized. The thickness of the synthesized PHEMA and POEGMA samples in the dry state are similar. Figure 6.1c,d represent the surface topographies of the PHEMA-3

and POEGMA-2 samples, respectively, in water at room temperature. These two samples display a thickness of 100 nm in water.

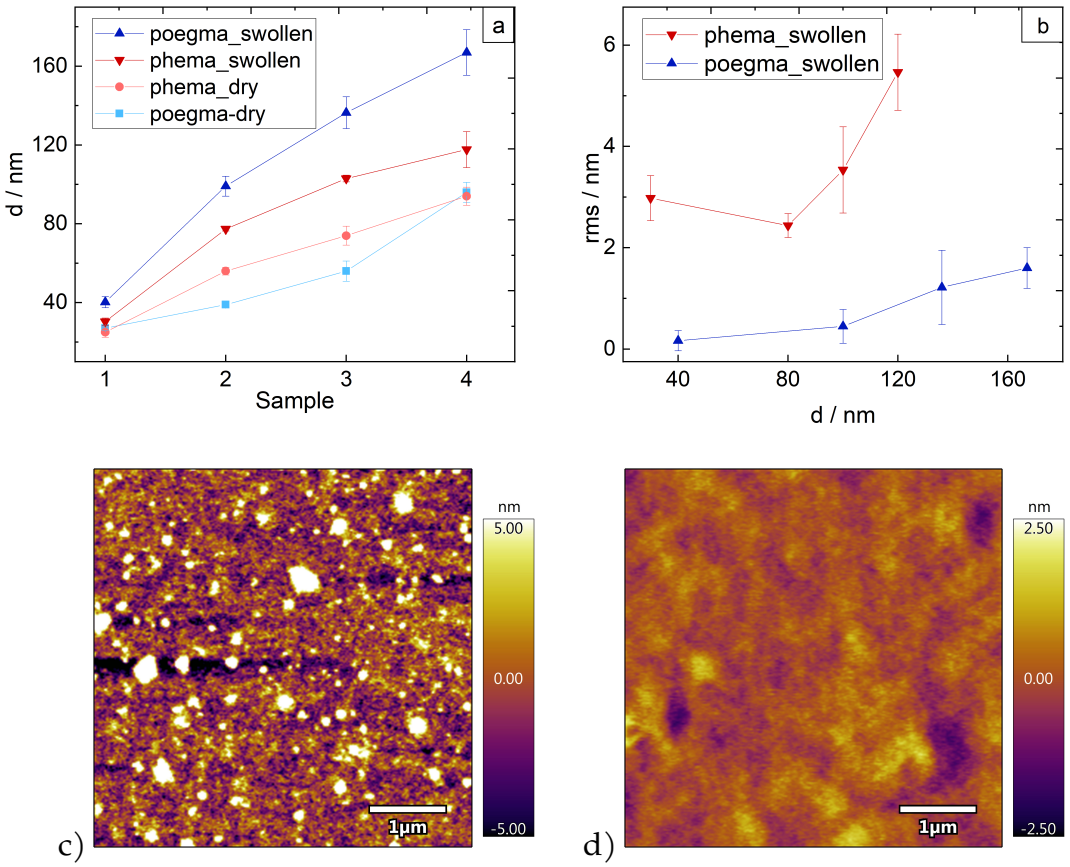

Figure 6.1: a) Thickness of the POEGMA and PHEMA brushes in the dry and swollen states, b) rms roughness of the POEGMA and PHEMA in the swollen state; surface topographies of c) PHEMA-3 and d) POEGMA-2 in water, respectively, obtained by conducting AFM in the scanning mode over the area of 5 µm × 5 µm.

Figure 6.1a shows that for all the samples, the brush thickness increases with increasing polymerization time, which is typical for controlled surface-initiated radical polymerization. This enables the adjustment of brush thickness by controlling the reaction time. Figure 6.1b presents the rms roughness of the synthesized brushes in the swollen state. The roughness of the brushes increases with increasing the brush thickness. This is in good agreement with previously published results from Christau *et al.*[167]

The swelling ratio of the brushes in Milli-Q water is defined as the thickness

of the brush in water divided by the thickness of the brush in dry state and the values are listed in Table 6.1. The swelling ratios are similar for all the brushes, with the values ranging from 1.2-2.6, and are in agreement with the swelling ratios of hydrophilic brushes.[168] The results listed in Table 6.1 exhibit two properties of the brush substrates: firstly, the swelling ratio of the brushes decreases as the brush thickness increases (samples 2-4); and secondly, the POEGMA brushes display a higher swelling ratio compared to PHEMA brushes.

Table 6.1: Swelling ratios of the POEGMA and PHEMA brushes

Sample	Swelling ratio POEGMA	Swelling ratio PHEMA
1	1.5	1.2
2	2.6	1.4
3	2.4	1.3
4	1.7	1.2

Wettability: The water contact angle of PHEMA and POEGMA brush substrates is reported in Figure 6.2. The average water contact angles (WCA) of the POEGMA and the PHEMA samples are $67° \pm 6°$ and $80° \pm 7°$, respectively. No systematic change in the WCA of the samples upon increasing the brush thickness is observed.

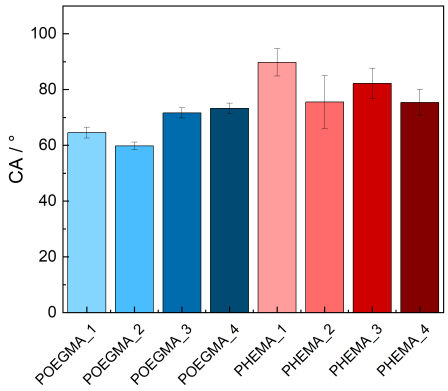

Figure 6.2: Water contact angle of PHEMA and POEGMA brush substrates

Mechanical properties: The Young's moduli of the PHEMA and POEGMA brushes in Milli-Q water at room temperature were determined by colloidal probe AFM. The aim of this measurement is to investigate whether the mechanical properties of the brush vary upon increasing the brush thickness and how this affects the self-propulsion of the particle. The experimental and evaluation procedure is described in Chapter 3. A typical force map which includes 100 single force-distance curves obtained over an area of 90 µm×90 µm of the brush substrate is shown in Figure 6.3a. The elastic moduli of the PHEMA and POEGMA brush substrates in Milli-Q water at room temperature were determined by fitting the force-indentation curves.

Figure 6.3b shows that the brushes exhibit Young's moduli of 1-2 kPa, which is an indication of a very soft polymer film. However, the POEGMA brush substrates display slightly higher elastic moduli values compared to the PHEMA brush. Moreover, the Young's moduli does not vary significantly with the brush thickness.

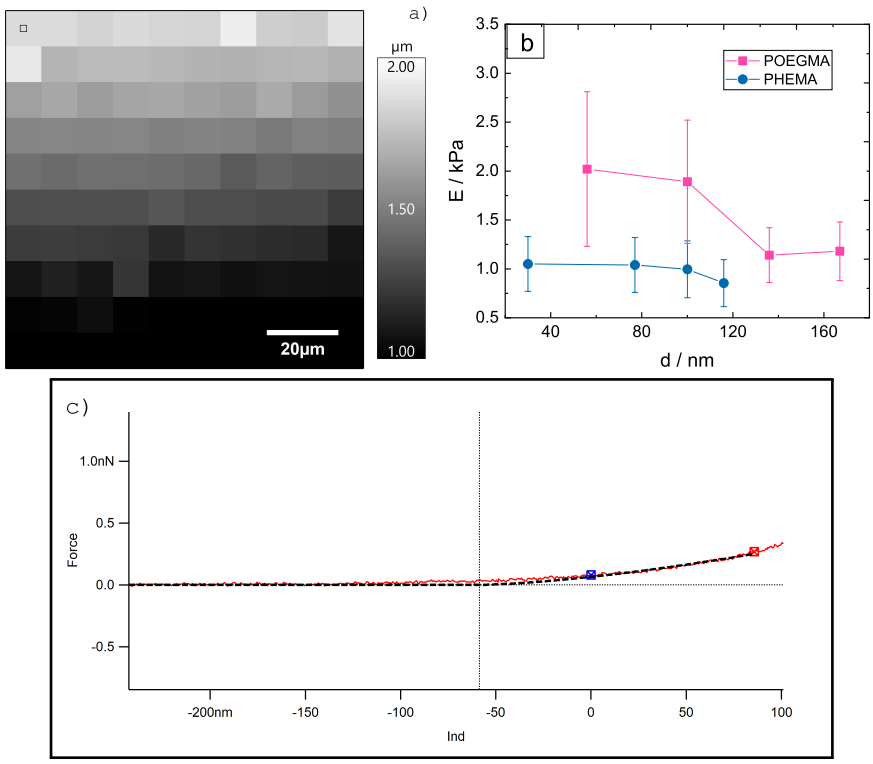

Figure 6.3: a) The force map including 100 single force-distance curves, b) elastic moduli of the PHEMA and POEGMA brush substrates in water at room temperature, and c) a typical force-indentation curve (the red line), where the black line is fitted to the outermost region of the brush indicated by the symbols

Surface charges of the substrates: Streaming current measurements are performed to study the surface charge properties of the substrates. Figure 6.4a,b shows the zeta potential and the isoelectric point of the POEGMA brush substrates with increasing the brush thickness. A thickness of 0 corresponds to the bare glass.

The bare glass has a zeta potential of -120 mV in Milli-Q water. Despite the neutral nature of POEGMA, all the POEGMA brushes display negative zeta potential values, however, their values are significantly lower compared to the bare glass. Moreover, Figure 6.4a indicates that increasing the brush thickness leads to a slight decrease in the zeta potential value for the first three POEGMA brush substrates. Whereas it increases again by further increasing the brush thickness.

The zeta potential of the POEGMA brush substrates is also investigated in l mM KCl solution. The trend is similar compared to the measurement in water, however, the substrates tend to have slightly lower zeta potential values in the salt solution. Exceptions are the last two POEGMA brush substrates whose surface charges increase upon adding salt.

Figure 6.4b indicates that the isoelectric point of the bare glass is at pH 4.2. The POEGMA brush substrate with the swollen thickness of 56 nm in water displays the highest IEP, whereas the substrate with the swollen thickness of 167 nm reaches the lowest IEP amongst the substrates. Moreover, Figure 6.4b reveals that increasing the brush thickness leads to a steep decrease in IEP.

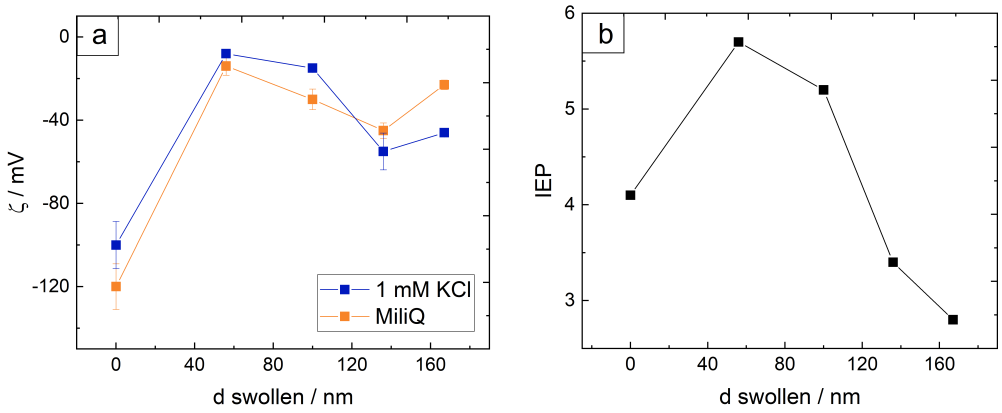

Figure 6.4: a) Zeta potential of the POEGMA brush substrates in Milli-Q water and 1mM KCl solution, b) isoelectric point of the substrates

SEM image of the particle: Figure 6.5 shows a SEM image of the herein used Janus particles with a diameter of 2.4 μm.

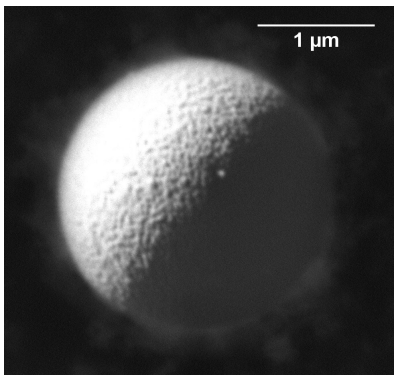

Figure 6.5: SEM image of an Au-PS Janus particle with a diameter of 2.4 μm

6.2.2 Self-propulsion of Au-PS Janus particle near POEGMA brush substrates

Figure 6.6a,b reports the experimentally obtained thermophoretic velocities and diffusion coefficients of a Au-PS Janus particle with a diameter of 2.39 μm and a zeta potential of -28.4 ± 6.2 mV close to the bare glass and POEGMA brush substrates with various thicknesses. The thermophoretic velocity and diffusion coefficient of the particle has been obtained through fitting MSD curves with equation 4.1, well below the persistence time $\tau_r = 1/D_r \approx 10$ s.[169] The error bars represent the standard deviations of at least 20 measurements for each data point. The D values are considerably lower than the the diffusion coefficient of the particle in bulk, D_{bulk}, which is in agreement with literature.[170] The average diffusion coefficient values near the POEGMA and PHEMA brushes are 0.07 ± 0.03 $\mu m^2 s^{-1}$ and 0.07 ± 0.02 $\mu m^2 s^{-1}$, respectively. According to Figure 6.6c, the thermophoretic particle velocity enhances with increasing brush thickness, until it reaches a maximum at about 100 nm brush thickness. A further increase in brush thickness leads to a decrease in particle velocity.

The MSD curves and the trajectories of the Au-PS Janus particles near the POEGMA brush substrates are shown in Figure 6.7.

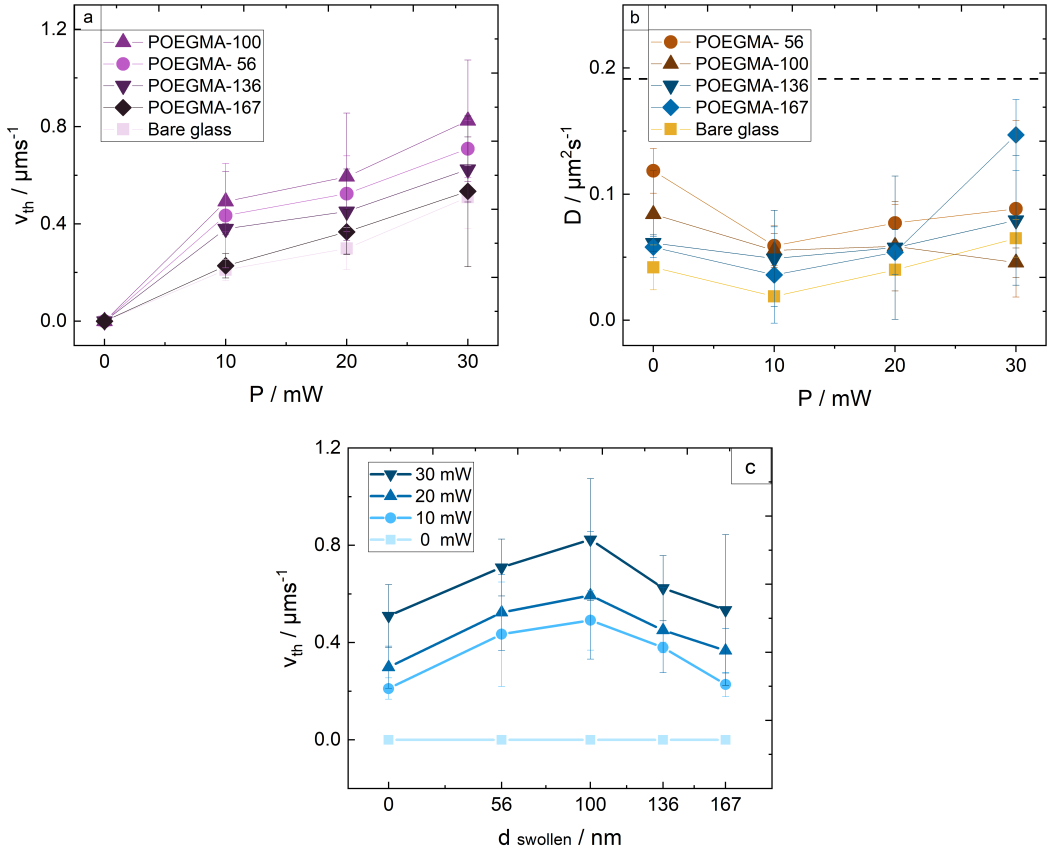

Figure 6.6: a) Thermophoretic velocity vs. laser power, b) diffusion coefficient, c) thermophoretic velocity vs. brush thickness of the Au-PS Janus particles near the POEGMA brush substrates; the dashed line in b resembles the diffusion coefficient of the particle with a diameter of 2.4 µm in bulk

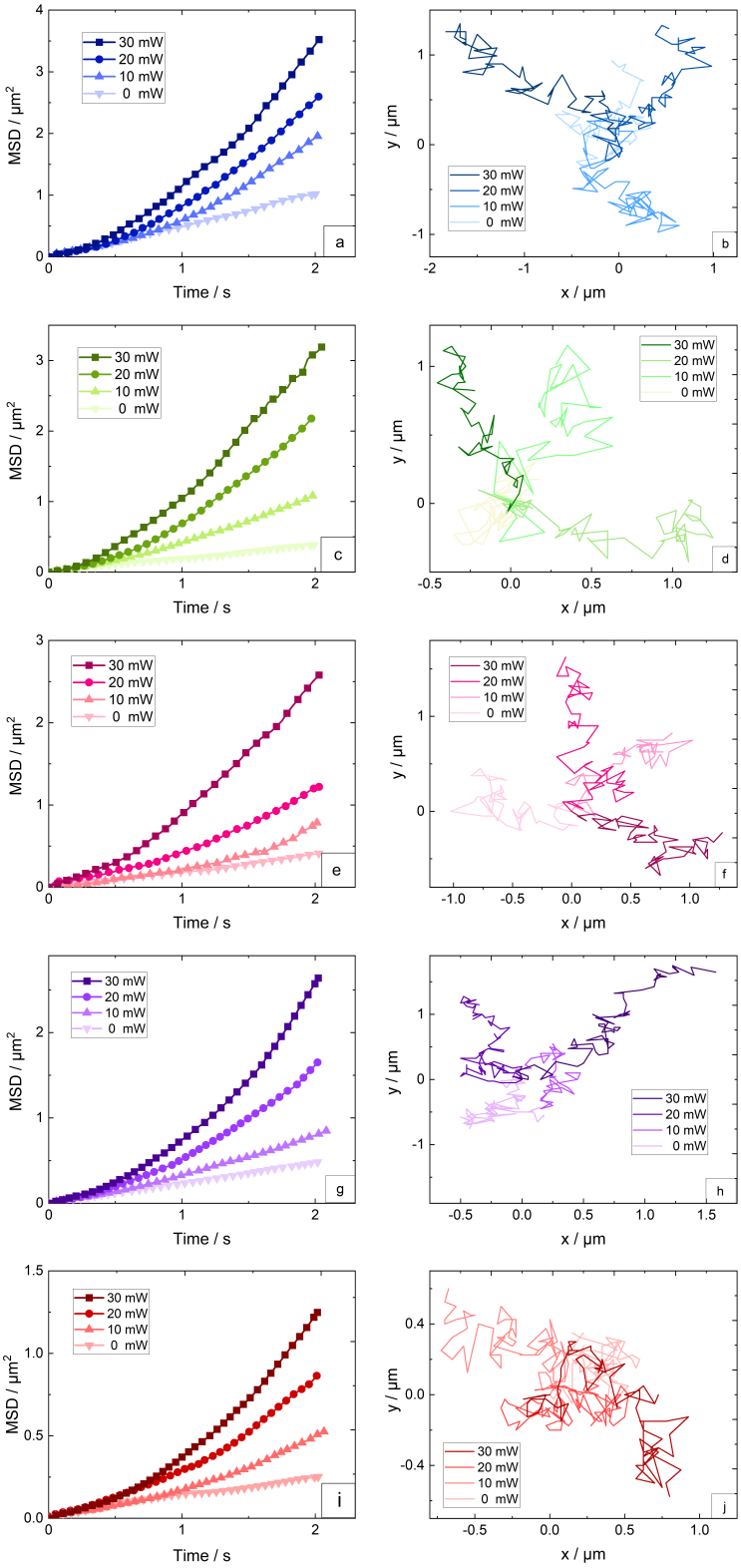

Figure 6.7: MSD curves and trajectories of the Au-PS Janus particle near a&b) POEGMA-56, c&d) POEGMA-100, e&f) POEGMA-136, g&h) POEGMA-167, and i&j) the bare glass, respectively

6.2.3 Self-propulsion of Au-PS Janus particle near PHEMA brush substrates

Figure 6.8a,b report the experimentally obtained thermophoretic velocities and diffusion coefficients of a Au-PS Janus particle with a diameter of 2.39 µm near the bare glass and PHEMA brush substrates with various thicknesses. Independently of the chemical nature of the brush, similar trends were observed for both brush systems regarding the relation between the thermophoretic velocity of the particle and the brush thickness, Figure 6.8c. Here again, the Janus particle reaches a maximum velocity near a PHEMA functionalized substrate with an intermediate thickness. Furthermore, Figure 6.8c shows an even higher thermophoretic velocity of the particle when it is near PHEMA brushes than POEGMA. The MSD curves and the trajectories of the Au-PS Janus particles near the PHEMA brush substrates are shown in Figure 6.9.

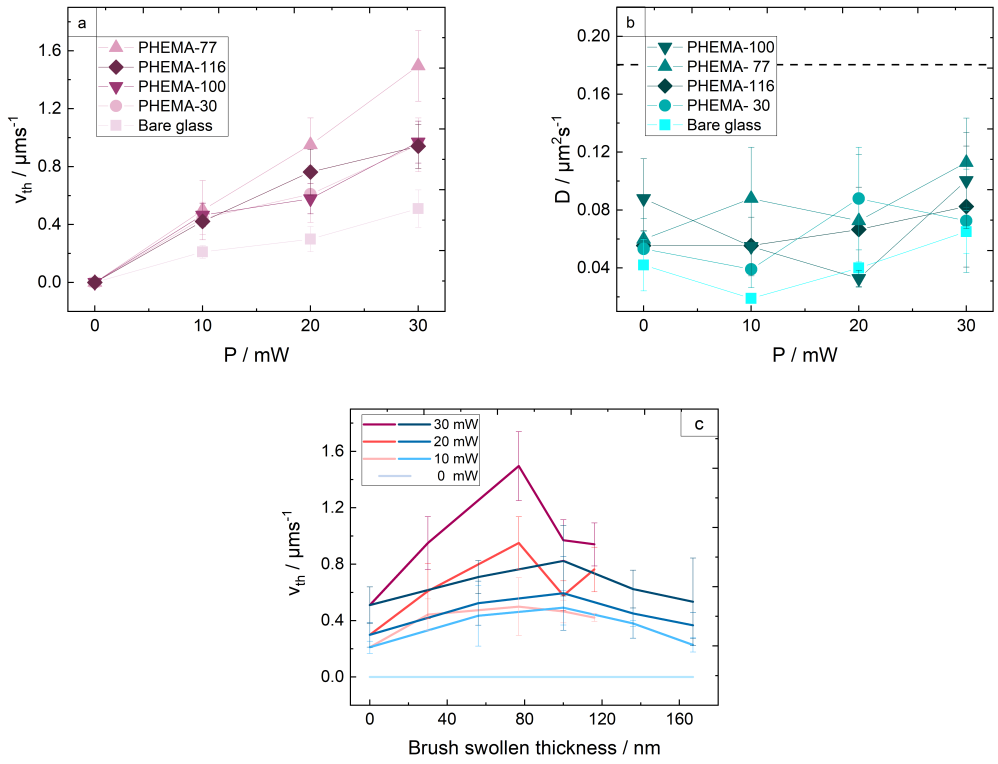

Figure 6.8: a) Thermophoretic velocity vs. laser power and b) diffusion coefficient of the Au-PS Janus particles near PHEMA, c) thermophoretic velocity vs. brush thickness of the Au-PS Janus particles near PHEMA (red curves) and POEGMA (blue curves) brush substrates; the dashed line in b resembles the diffusion coefficient of the particle with a diameter of 2.4 µm in bulk

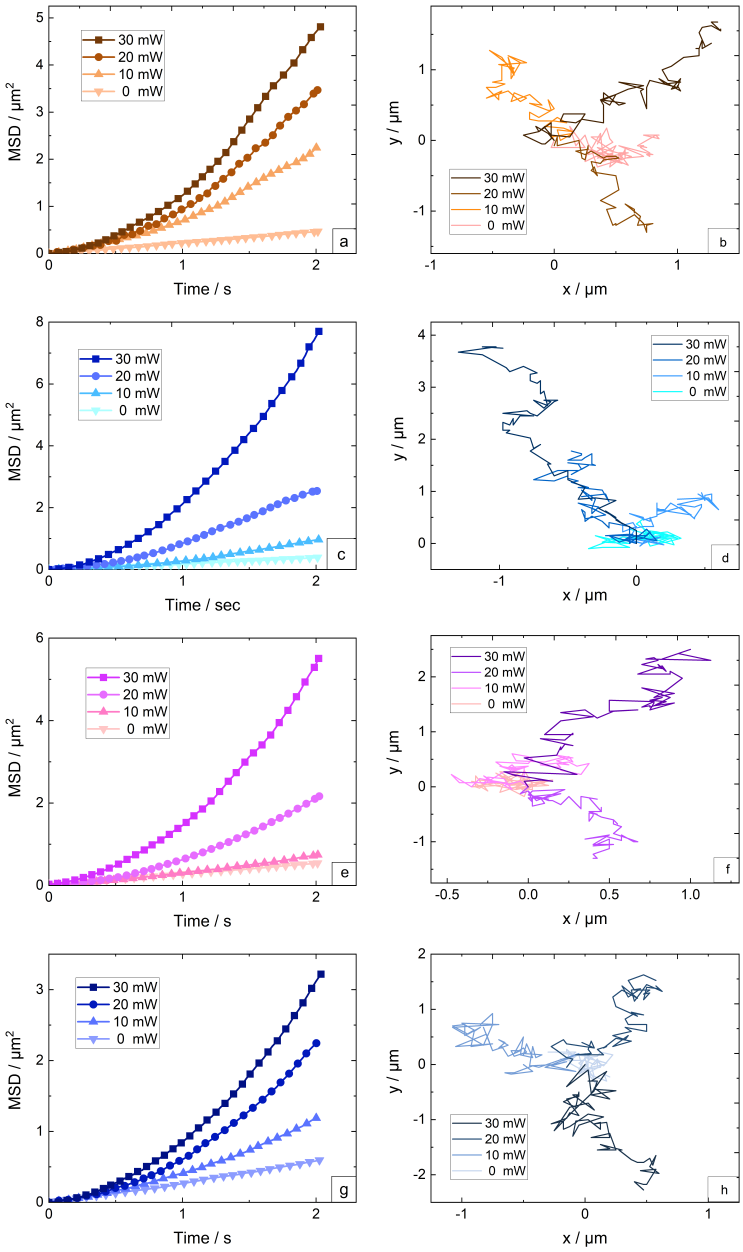

Figure 6.9: MSD curves and trajectories of the Au-PS Janus particle near a&b) PHEMA-30, c&d) PHEMA-77, e&f) PHEMA-100, and g&h) PHEMA-116, respectively

6.3 Discussion

6.3.1 The properties of the brush functionalized substrates

Thickness and roughness: The thickness of the POEGMA and PHEMA brushes increases with increasing polymerization time. This growth behavior has been observed for other polymer bush types as well.[171,172]

The rms roughness of the POEGMA and PHEMA brush substrates increases with increasing thickness. During the polymerization, monomers are hindered to reach the growing radical chain. Hence, individual chains do not grow simultaneously. Subsequently, brush chains achieve various lengths during the polymerization, thus, the roughness of the brush-functionalized substrate increases.

The swelling ratio of the POEGMA brush substrates is shown to be higher than PHEMA, Table 6.1. Thus, it is inevitable to consider the chemical structures of POEGMA and PHEMA chains (Figure 6.10).

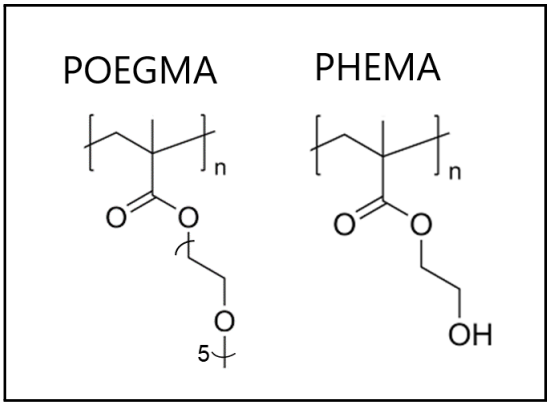

Figure 6.10: Chemical structures of POEGMA and PHEMA

The higher swelling ratio of the POEGMA brush substrates is attributed to the fact that POEGMA consists of ethylene oxide (-CH2-CH2-) segments in its side chain with repeating units of five, whereas the number of ethylene oxide group on the side chain of PHEMA is only one. Ethylene oxide is known for its strong hydration. As a result, the higher amount of ethylene oxide in a polymer chain

leads to a stronger attraction between the polymer and water molecules, thus the POEGMA brush swells stronger.[122]

Furthermore, the swelling ratio of the POEGMA and PHEMA brushes decrease with increasing the brush thickness (sample 2-4). This suggests that the thicker brush, due to steric hindrance, is already more stretched in the dry state, whereas the thinner brush is more in a coiled state with lower chain densities.[173] Therefore, thicker brush swells less.

Wettability: Despite the higher hydrophilicity of the POEGMA brush, the average WCA of the POEGMA brush substrates is comparable to the average value of PHEMA. This arises from the fact that POEGMA consists of methoxy-ended ethylene oxide side chains, which slightly reduces its affinity to make hydrogen bonding with water molecules. Thus prevents the WCA to reach lower values.[121] PHEMA brushes bear hydroxyl groups at the end of their side chains which promote the hydrophilicity of the brush substrate at its outermost layer where the WCA measurements take place. Hence, its WCA decreases. Therefore, the impact of substrate hydrophilic properties on the self/propulsion of particles can be ruled out here.

Nanomechanical properties of the brush substrates: The Young's moduli of the PHEMA and POEGMA brushes in water at room temperature are representative of very soft brushes. This aligns well with previously reported nano-mechanical properties of brushes in good solvents.[174] However, it should be noted that only a few studies in the literature have investigated the nanomechanical properties of PHEMA and POEGMA brushes and their obtained Young's moduli differ from the results reported in this thesis.[173,175,176] The Young's moduli of PHEMA, POEGMA_6, and POEGMA_{10} brushes (the subscripts refer to the number of ethylene oxide units in the POEGMA side chains) reported by Desseaux *et al.* are in the range of 1-4 MPa which is three orders of magnitude higher than the values shown in Figure 6.3b. This high elastic modulus is ascribed to the crystallization of the oligo(ethylene oxide) chains in their chemical structures. However, it should be mentioned that fitting the force-distance curves requires extra care, as choosing the correct fit region is essential to obtain the right values for the Young's Moduli. Surface grown polymer brushes often consist of two distinct regions: a thin dense polymer layer near the substrate, and a less dense polymer layer farther away from the substrate. The fit to the force-distance

curves should be applied to the outermost region of the brush, where its elastic property is not affected by the underlying substrate.[177]

Despite their stronger hydrophilicity, POEGMA brushes exhibit slightly higher elastic moduli compared to PHEMA brushes. This is attributed to the fact that the POEGMA brush consists of longer ethylene oxide side chains that generate a lightly cross-linked polymer structure, which subsequently gives rise to the elastic moduli of the substrates.[178]

The Young's moduli of PHEMA and POEGMA brushes did not vary significantly with increasing brush thickness, which is in agreement with literature.[173] Therefore, it is less likely that the velocity trend of the Janus particle is affected by the mechanical properties of the substrate.

Surface charges of the brush functionalized substrates: The zeta potential of the bare glass is -120 mV in Milli-Q water. This value originates from protonation and deprotonation of the abundant surface hydroxyl groups on the bare glass.

Functionalization of the substrate with the POEGMA brushes leads to a drastic decrease of the zeta potentials, whereas the variation of the brush chain length does not play a significant role in the zeta potential value. Upon grafting the substrate with neutral POEGMA brushes, significant amounts of hydroxyl groups are substituted with the initiator molecules. This dramatically reduces the number of charges at the interface, leaving the substrate almost uncharged. As the same amount of initiator molecules were used in the polymerization process, it is assumed that the grafting density of the brush substrates is equal. Therefore, the number of unreacted hydroxyl groups at the interface are comparable among the POEGMA brush substrates. Hence no considerable change in the zeta potential of the substrates upon increasing the POEGMA thickness was observed.

Furthermore, all POEGMA brushes, independent of their thickness, show a negative zeta potential value. This phenomenon is typical for neutral polymers with non-dissociable groups and it is caused by the preferential ion adsorption of hydroxide or chloride ions (OH^- or Cl^-) from water or an electrolyte solution at the interface at pH>IEP.[179,180] The streaming current measurements were performed in Milli-Q water at pH 5.5, which is higher than the IEP of the samples except for the POEGMA-56 sample. Therefore, the POEGMA-56 is

slightly less charged than the other POEGMA substrates, thus it reaches the lowest zeta potential value.

The zeta potential of the substrate is a determining factor on the strength of the thermo-osmotic flow at the substrate, hence affecting the particle velocity. This relation is explained in the section 6.3.2.

The addition of 1 mM KCl to the solution reduces the surface charging and the zeta potential value due to the screening of charges by potassium ions K^+. Moreover, the adsorption of K^+ to the deprotonated hydroxyl groups at the interface leads to a compression of the EDL layer, thus the zeta potential value decreases.[181] Surprisingly, the zeta potential values of the POEGMA-136 and POEGMA-167 increased upon adding the salt. This suggests that due to the stronger adsorption of K^+ to the brush $(\mathrm{pH} \gg \mathrm{IAP})$, the electrostatic repulsion between the polymer chains is so high that it can not be influenced by the low salt concentration.[133] Therefore, the zeta potential slightly increases.

The IEP of the bare glass was at pH 4 which is within the range of published data[131,182] and it implies that the surface density of protons and hydroxide ions are equal at pH 4. Functionalization of the bare glass with the thinnest POEGMA brush leads to an increase in the IEP value. This originates from the lower zeta potential of this substrate, where fewer amounts of surface charges are available within the EDL, hence IEP can be reached with the lower amount of HCl.

Increasing the POEGMA brush thickness influences the IEP dramatically, from pH 5.7 for the thinnest brush to pH 2.8 for the thickest one. This is caused by the enhanced preferential adsorption of hydroxide ions upon increasing the brush thickness. As the number of charges increases in the system, a higher amount of HCL is needed to reach the isoelectric point. Therefore, the IEP decreases for the POEGMA brush with increasing thickness.

6.3.2 Self-propulsion near POEGMA and PHEMA brush substrates

Figure 6.8c shows that the swimming speed does not monotonously change with brush thickness but it rather shows a distinct maximum at a certain intermediate

thickness. To shed light on this observed velocity trend, it is of great importance to consider the role of thermo-osmotic flow at the brush/water interface.

Thermo-osmosis is induced by a temperature gradient at interfaces and drives the solute particles to the cold or the warm region depending on the interfacial properties.[183] When the glass substrate comes into contact with water, the substrate becomes negatively charged (at intermediate pH) which subsequently gives rise to an accumulation of cations within the electric double layer (EDL) of the substrate, where the ions are distributed uniformly parallel to the substrate surface in the absence of a Janus colloid. Based on the ionic strength of the deionized water of 10^{-5} M, an EDL with a thickness of 100 nm is expected to be formed at the glass/water interface. In the present case, laser irradiation leads to the generation of local heat at the gold side of the Janus particle. This generated heat is subsequently transferred to the glass slide near the particle, as the heat diffusion is several orders of magnitude faster than the particle diffusion.[184] The distance between the particle and the glass slide is expected to be 200-300 nm.[185] The occurrence of a temperature gradient within the glass slide disturbs the distribution of ions within the EDL and leads to a relatively low ion concentration beneath the hot gold cap. This excess amount of ions at the cold side creates an excess hydrostatic pressure which subsequently leads to flow of fluid towards the hot side of the particle. Due to anisotropy of the particle surface flow pattern is not symmetric with respect to the particle center, leading to an effective torque rotating the gold cap away from the substrate. This torque vanishes only if the gold cap is oriented in the upwards direction, such that the projection of the swimming velocity in the direction parallel to the substrate vanishes, Figure 6.11. In practice, the orientation of the particles of coarse fluctuates, e.g. due to rotational diffusion, such that the particle still shows a finite speed component along the substrate most of the time. Thus, the measured speed, i.e. the average particle speed along the substrate, is a compromise between the substrate-induced alignment of the particle perpendicular to the substrate and the presence of fluctuations. The particle speed is therefore expected to decrease as the velocity of the thermo-osmotic flow along the substrate increases.

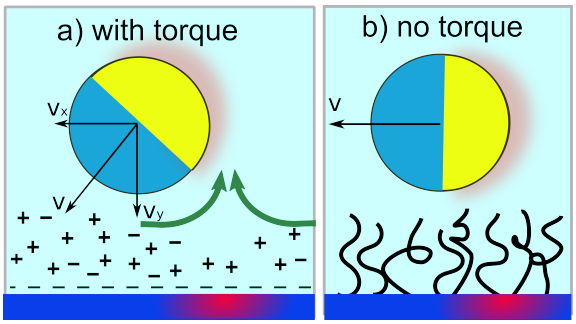

Figure 6.11: Schematic illustration of particle self-propulsion near a) the bare glass with torque vs. b) near the brush functionalized glass without torque. The green arrows indicate the thermo-osmotic flow induced by the Janus particle

The following simple calculation based on the Smoluchowski equation for the probability distribution of the particle orientation (in 2D for simplicity) can be considered:

$$\dot{P}(\theta, t) = -\partial_\theta[\Omega P] + D_r \partial_\theta^2 P \tag{6.1}$$

where D_r is the rotational diffusion coefficient, θ is the angle between the symmetry axis of the particle and the substrate, such the cap vertically points vertically upwards for $\theta = \pi/2$, and $\Omega = \Omega_0 \cos\theta$ is the substrate induced rotation rate of the particle, whose magnitude reaches its maximal value Ω_0 for $\theta \in \{0, \pi\}$.

The steady state solution of this equation reads

$$P(\theta) = \exp[(\Omega_0/D_r)\sin\theta]/I_0(\Omega_0/D_r) \tag{6.2}$$

which has been normalized to $\int_0^{2\pi} P(\theta)\mathrm{d}\theta/(2\pi) = 1$ and where I_0 is the 0-th modified Bessel function of the first kind.

This distribution features a distinct peak at $\theta = \pi/2$ (cap points upwards) and a minimum at $\theta = 3\pi/2$ (cap points downwards) which is increasingly pronounced as Ω_0/D_r increases.

The expectation value of the measured speed, i.e. of the velocity component parallel to the substrate is then given by $\langle v_\parallel \rangle = (1/\pi)\int_{-\pi/2}^{\pi/2} v_0 \cos\theta P(\theta)\mathrm{d}\theta$, where v_0 being the self-propulsion speed of a particle which is aligned parallel to the substrate. Thus, the relative slowdown due to the substrate is then given by

$\langle v_{\parallel}\rangle/\langle v_{\parallel}(\Omega_0 = 0)\rangle = D_r \sinh(\theta)/[\Omega_0 I_0(\Omega_0/D_r)]$, which decreases with increasing Ω_0 and increases as D_r increases.

This simple result complements our understanding that the measured speed is essentially a compromise between the substrate-induced effective torque which systematically turns the cap into the upwards direction and reduces the measured speed, and rotational diffusion which randomizes the cap-orientation. The theoretical part was performed by Prof. Benno Liebchen at TU Darmstadt.

The impact of the thermo-osmotic flow at the interface weakens by reducing the EDL by adding salt to the medium or decreasing the charge density within the EDL by functionalizing the substrate with polymer brushes, as it will be discussed here. It is expected that the thickness of the EDL does not change significantly by functionalizing the substrate with polymer brushes. The Debye length depends on the relative permittivity of a medium which consequently depends on its refractive index. As the refractive index of the POEGMA-functionalized substrates (1.37) is very similar to that of water (1.33), the EDL thickness is expected to remain almost constant as the brush thickness varies.

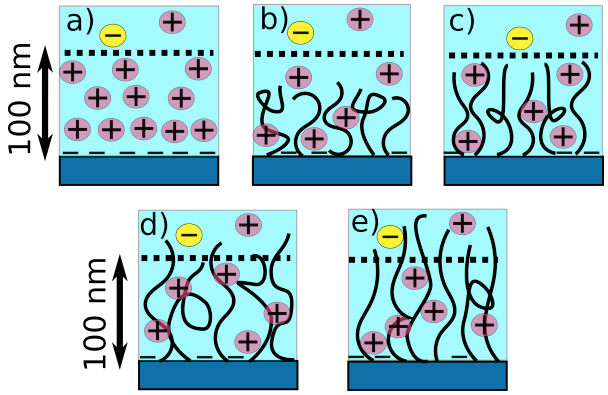

Figure 6.12: Schematic illustration of the distribution of ions within the EDL and its variation upon functionalization of the glass with polymer brushes. The arrows with the 100nm label indicate the thickness of the EDL.

Figure 6.12a illustrates the distribution of ions within the EDL at the bare glass substrate with no polymer coatings. The glass substrate carries silanol groups (Si-OH), which are deprotonated (Si-O^-) when in contact with water and above the isoelectric point (pH 2-3), making the surface negatively charged.[186] This gives rise to an excess of ions at the glass/water interface which subsequently leads to the formation of an electric double layer with a thickness of about 100 nm

at the interface. The zeta potential of the bare glass substrate was measured to be -121 mV. Here, the thermo-osmotic flow at the interface, which increases as the magnitude of the zeta potential increases, is higher than for substrates functionalized with a non-ionic polymer as we will see next. Therefore, the bare glass substrate leads to a minimal swimming speed.

Figure 6.12b is attributed to the substrate functionalized with non-ionic POEGMA brushes with the swollen thickness being lower than the thickness of the electric double layer. Functionalization of the substrate with brushes significantly lowers the amount of ions available within the EDL, as the initiator molecules required for the polymerisation bind to the silanol groups, reducing the surface charge. Hence, the substrate is less negatively charged compared to the bare glass. The zeta potential of the this substrate is -14 mV which arises from the non-functionalized silanol groups at the interface that attract the ions, hence render the substrate slightly negatively charged. Consequently, the generated thermo-osmotic flow at the interface is weaker in comparison to the one at the bare glass surface,[183] therefore particle thermophoretic velocity enhances.

Figure 6.12c shows the brush for which the particle reaches its maximum thermophoretic velocity. In this case, the thickness of the brush in the swollen case is comparable to the thickness of the Debye length; therefore, the access of ions at the interface is relatively small. Here, the zeta potential of the substrate displays no significant change upon increasing the brush thickness, as the grafting density, hence the number of non-functionlaized silanol groups at the interface has remained constant. The low amount of ions and hence the near-absence of a thermo-osmotic flow at the interface leads to the largest particle velocity in our experiments, as no effective torque is present at the interface to "disturb" the particle motion along the interface.

Figure 6.12d shows the case where the thickness of the swollen brush is beyond the electric double layer and no significant thermo-osmotic flow is assumed to be present at the brush/water interface. However, the particle velocity is lower than the previous case. Here brush roughness and hence the brush slip length comes into play. Ketzetzi *et al.* recently showed that the substrate slip length could significantly influence the catalytic propulsion of colloidal swimmers.[70] Moreover, it has been shown that surface roughness has an inverse effect on the slip length, i.e. the higher the surface roughness, the smaller the slip length.[187]

As the brush thickness increases its roughness increases as well;[162] hence the brush slip length and subsequently the slip velocity decreases which leads to a reduced particle velocity.

Figure 6.12e illustrates the brush for which the particle velocity further decreases upon increasing the brush thickness. The roughness of the substrate reaches a maximum; thus particle velocity reaches its minimum value amongst the brush-functionalized samples.

To test the hypothesis of the Debye length as the critical length, the effect of salt was studied. However, the measurement in 1 mM NaCl solution was not successful as the particles stuck to the substrate and did not show any mobility.

POEGMA chains consist of ethylene oxide segments in its side chain with a repeating unit of five, whereas the number of ethylene glycol group on the side chain of PHEMA is only one. This indicates that a POEGMA brush contains longer side chains in comparison with a PHEMA brush. Moreover, a lower refractive index of the POEGMA brush (1.37) in the swollen state suggests a lower polymer density compared to the PHEMA brush, which has a refractive index of 1.46. Therefore, the combination of longer side chains and the lower polymer density could lead to the conclusion that the grafting density of the POEGMA brush is lower compared to the PHEMA brush (Figure 6.13a,b). In other words, there is more space between the brush chains available for water to penetrate the brush. Hence higher ion density could contribute to the thermo-osmotic flow at the brush/water interface; therefore, the particle velocity is lower near POEGMA-functionalized substrates.

It is worth-mentioning that the maximum velocity of the Janus particle is achieved near PHEMA-2 with a swollen thickness of 80 nm, i.e. shorter than the one of POEGMA brushes. This might be explained by a lower water content which is indicated by a higher refractive index of PHEMA brushes (1.46) than of POEGMA brushes (1.37). The lower amount of water and the higher polymer density, respectively, leads to lower polarity of PHEMA brushes which decreases the relative permittivity and therefore the Debye length. Therefore, the particles reach their highest velocity at shorter brushes than in case of POEGMA brushes (100 nm).

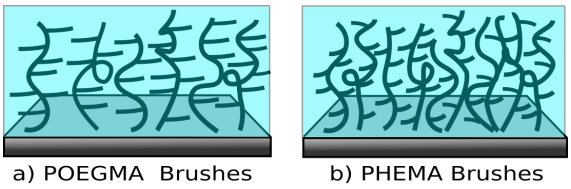

Figure 6.13: Schematic representation of a) POEGMA and b) PHEMA brushes

6.4 Conclusion

The results elucidate the significant impact of the physicochemical properties of the substrate on thermophoretic microswimmers. In particular, they unveil the occurrence of a speed maximum at brush-functionalized surfaces at an intermediate brush thickness. It is expected that the underlying mechanism, which is based on particle-induced osmotic flows along the substrate and surface roughness, essentially transfers also to self-diffusiophoretic and self-electrophoretic swimmers. Accordingly, these results may help to understand the origin of the large discrepancy between the speed values, which have been observed for the same microswimmer in the literature. They also offer a versatile route to control the speed of self-phoretic microswimmers through functionalization of the underlying substrate, which could be applied in the future e.g. to design complex motility landscapes.

Chapter 7

Conclusion and Future Perspectives

7.1 Summary and Conclusion

This thesis presents the self-propulsion of thermophoretic active colloidal particles in 2D near substrates with various physicochemical properties. Although numerous experimental and theoretical studies have been devoted to investigate the active motion of synthetic microswimmers, still the impact of the substrate on their motion was missing. Therefore, more detailed studies were needed to shed light on this aspect of the research field.

The thesis particularly focuses on the substrates functionalized with polymer brushes. Brushes with various structural and physical properties were synthesized and investigated with methods such as ellipsometry, x-ray reflectometry, atomic force microscopy, streaming current, and contact angle measurements. Thereby, an extensive overview of the structural features of the brushes is achieved.

The first part is devoted to the impact of substrates with various surface wettabilities on the self-propulsion of Au-PS particles. Three substrates were prepared: a bare glass, a POEGMA brush substrate, and a silanized glass. The silanized glass is served as the hydrophobic substrate, whereas the hydrophilicity of the bare and the POEGMA brush substrate is comparable. This study reveals that the particle velocity near the brush substrate is higher than its velocity near the silanized glass and the bare glass. This is explained by the presence of nano-bubbles at the silanized glass/water interface which alters

the physicochemical properties of the substrate, consequently, the the particle velocity is decreased. Moreover, it is emphasized that the hydrophilic properties of the substrate is not a determining factor in the thermophoretic speed of the particle and other interfacial parameters such as roughness and zeta potential must be taken into account.

As the particle achieved its highest velocity near the brush-functionalized substrate, the second part of this thesis is contributed to the self-propulsion of Janus particles near PNIPAM-functionalized substrate. The results are compared with the active motion of a particle near a bare glass. Moreover, the impact of -COOH functionalization on the thermophoretic velocity of the particles is investigated. The results show that the functionalization of the substrate with polymer brushes leads to an enhancement of the particle velocity. The results are interpreted by taking the impact of the thermo-osmotic slip at the interface into account. Moreover, the study shows that increasing the brush thickness does not necessarily lead to higher particle velocities. In fact, higher brush thickness decreases the particle velocity, although still the particle velocity is higher than the bare glass. These findings highlight the non-negligible impact of the substrate, where the prior knowledge of the substrate properties may facilitate the interpretation of self-propel measurements.

The final part of the thesis focuses only on the brush-functionalized substrates with various chemical properties, thicknesses, and grafting densities. Moreover, as the thermoresponsive nature of the PNIPAM brush leads to mutual effects with the particle and could cause an undesired velocity decrease, POEGMA and PHEMA brushes are selected which show excellent hydrophilic properties and do not undergo any conformational changes within the experimental conditions. The Au-PS particle expresses a similar velocity trend with respect to the brush thickness, irrespective of the brush chemical structure. Remarkably, it is shown that the swimming speed depends non-monotonously on the brush thickness, leading to a characteristic speed maximum at an intermediate brush thickness. The emergence of such a speed-maximum is explained by competition of surface-charge induced substrate flows, which slow down the swimmer but systematically decrease as the brush thickness increases and a competing slow-down of the swimmers with increasing surface roughness.

These results open a route towards the systematic design of motility-landscapes

for microswimmers through patterning substrates with polymer brushes. They might also help to resolve the quest for the origin of a strong discrepancy of swimming speeds which have been reported in the literature for the same swimmer type, which may, as the present study suggests, very well be a consequence of the influence of the substrate.

7.2 Future Perspectives

Despite the promising potential of active matter shown by theoretical and experimental studies, this field is still in its infancy. More experimental studies are required to perform to keep up with the theoretical ones and to achieve a robust understanding of microswimmer's behavior. In the following, a few suggestions are presented that can be applied to the present study to improve the particle motion and broaden its horizon.

In the realm of microswimmers, it of great importance to improve the directed motion of a particle. By considering the results obtained in the present thesis, micro-channels created by patterning the substrate with polymer brushes would be an interesting study to conduct. Covering a surface-initiated substrate with a desired mask and exposing it to UV light would be an ideal way to create brush patterned structures on the substrate.

Moreover, the Janus particles can be further functionalized with dye moieties or nanogel particles to investigate their cargo transport properties. The size and zeta potential of the cargo could affect the self-propulsion characteristics of the particle.

The focus of present thesis was on the self-propulsion of single Janus particles. Considering the rich theoretical studies, it is highly relevant to perform the measurements in the presence of multiple active particles as well as an ensemble of active and passive particles. The resulting collective behavior of active particles and the interactions between active and passive particles near brush-functionalized substrates would further enhance our vision of self-thermophoretic microswimmers. A profound theoretical study is crucial to further refine the results.

Chapter 8

Appendix

Degrafting of polymer brushes

To determine the grafting densities of the POEGMA and PHEMA brushes the brushes were subjected to degrafting by vertically dipping into a 0.1 M tetrabutyl ammonium fluoride (TBAF) solution. The TBAF solution was prepared by adding 1 mL of 1 M TBAF in 10 mL of tetrahydrofuran (THF). The samples were incubated in the TBAF solution at 60°C for 24-36 hours.[188] Degrafting time varies based on the initial thickness of the brush. During the incubation time, the samples were removed from the solution at regular time intervals and their thicknesses were inspected with ellipsometry.

Figure 8.1 shows the progress of the degrafting with time. The x-axis is the relative thickness which is the dry thickness of the brush d divided by the initial dry thickness of the brush d_0. The POEGMA substrates undergo a stepwise degrafting procedure, such that their initial thickness reduces by $30 - 40\%$ after 5-7 hours of incubation time. It should be noted that the onset of degrafting shifts to shorter times with decreasing the polymer thickness. The POEGMA-120 and POEGMA-150 are successfully degrafted after 24h and 48h, respectively.

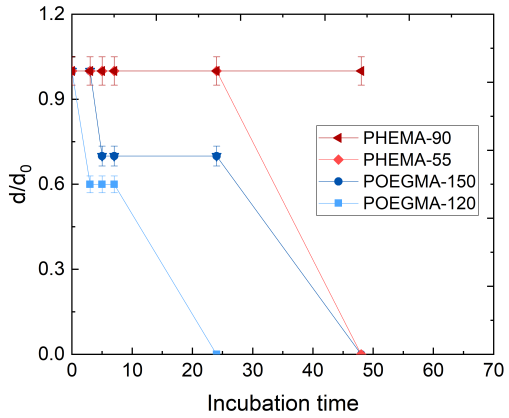

Figure 8.1: Degrafting of the POEGMA and PHEMA brushes from planar silicon substrates in 0.1 M TBAF solution at 50°C as a function of incubation time; the numbers given in the legend represent the dry thickness of the brushes

Furthermore, the thickness of PHEMA-55 and PHEMA-90 did not change within the first 24 hours of incubation time. In fact, the PHEMA-90 was not degrafted from the substrate at all even after 56 hours, whereas the PHEMA-55 was successfully degrafted after 48 hours.

The surface anchored POEGMA and PHEMA brushes were degrafted from the silicon substrate using TBAF. Patil *et al.* showed that TBAF can be effectively applied to break the Si-O bonds and thus helps to degraft polymer brush chains from silicon-based substrates.[188] As TABF attacks the Si-O bond, it is of great importance to consider the nature of trifunctional silane attachment to the substrate. The presence of trifunctional silanes can cause in-plane linkages and lead to the formation of clusters that are held by incomplete Si-O networks. Subsequently, polymer brushes could be grown from an initiator as an individual chain, or they can form assemblies of chains grown from an imperfect silane cluster.[189] Figure 8.2 displays the hypothesis in that regard.

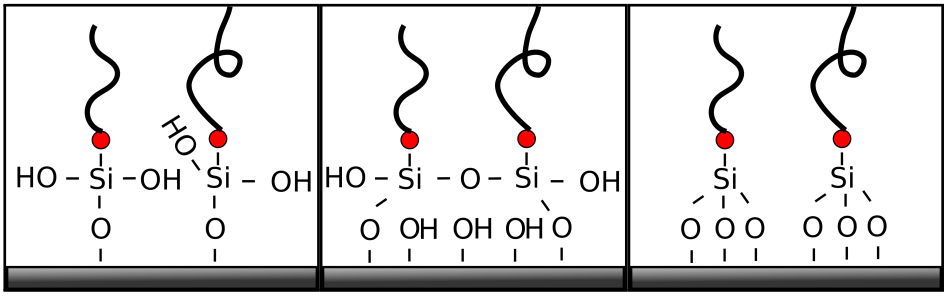

Figure 8.2: From left to right: attachment of the initiator to the surface with one (α), two (β), and three points of attachment (γ); the red dots represent the initiator molecules

The POEGMA samples degrafted relatively sharp within the first few hours of incubation. This suggests that the degrafted brushes were attached to the substrate with one point of attachment (α). It should be also considered that longer chains are more prone to degraft at the early stages of degrafting.[190] The sharp decrease is followed by a plateau which indicates that the remaining polymer chains on the substrate are attached to the substrate with two or three points of attachment. Therefore, longer times are needed to degraft the remaining chains.

Cleavage of the POEGMA-120 occurred within 24h, whereas the POEGMA-150 was cleaved after 48h, suggesting that the thicker brushes need more time to degraft from the substrate. This phenomenon was observed by Ataman *et al.* as well and it stems from an increased fraction of cross-linked POEGMA chains with a higher thickness which prolongs the Degrafting process.[191] PHEMA-55 is degrafted without showing any interval step, which could be due to the grafting of the brush to the substrate with two or three points of attachment, thus, longer cleavage time.

The degrafted polymers were further analyzed by the gel permeation chromotography (GPC) method to determine the molecular weight and hence the grafting density of the polymer brush. The GPC measurements were performed by Mrs. Heike Herbert at the group of Prof. Biesalski at TU Darmstadt. The preliminary results showed that the molecular weight of the polymers are beyond the allowed range of the instrument. Therefore, the results were not reliable and they are not shown here.

Bibliography

[1] Vogel, P. D. Nature's design of nanomotors. 2005; pp 267–277.

[2] Khataee, H. R.; Khataee, A. R. Kinesin and dynein smart nanomotors: Towards bio-nanorobotic systems. *Nano* **2010**, *5*, 13–23.

[3] Jankowsky, E.; Fairman, M. E.; Yang, Q. RNA helicases: versatile ATP-driven nanomotors. *Journal of nanoscience and nanotechnology* **2005**, *5*, 1983–1989.

[4] Utada, A. S.; Bennett, R. R.; Fong, J. C.; Gibiansky, M. L.; Yildiz, F. H.; Golestanian, R.; Wong, G. C. Vibrio cholerae use pili and flagella synergistically to effect motility switching and conditional surface attachment. *Nat. Commun.* **2014**, *5*, 1–8.

[5] Di Leonardo, R.; Dell'Arciprete, D.; Angelani, L.; Iebba, V. Swimming with an image. *Phys. Rev. Lett.* **2011**, *106*, 038101.

[6] Lauga, E.; DiLuzio, W. R.; Whitesides, G. M.; Stone, H. A. Swimming in circles: Motion of bacteria near solid boundaries. *Biophys. J.* **2006**, *90*, 400–412.

[7] Friedrich, B. M.; Jülicher, F. The stochastic dance of circling sperm cells: Sperm Chemotaxis in the plane. *New J. Phys.* **2008**, *10*, 123025.

[8] Nosrati, R.; Graham, P. J.; Zhang, B.; Riordon, J.; Lagunov, A.; Hannam, T. G.; Escobedo, C.; Jarvi, K.; Sinton, D. Microfluidics for sperm analysis and selection. *Nature Reviews Urology* **2017**, *14*, 707–730.

[9] Jikeli, J. F.; Alvarez, L.; Friedrich, B. M.; Wilson, L. G.; Pascal, R.; Colin, R.; Pichlo, M.; Rennhack, A.; Brenker, C.; Kaupp, U. B. Sperm navigation along helical paths in 3D chemoattractant landscapes. *Nat. Commun.* **2015**, *6*, 1–10.

[10] Kantsler, V.; Dunkel, J.; Polin, M.; Goldstein, R. E. Ciliary contact interactions dominate surface scattering of swimming eukaryotes. *Proc. Natl. Acad. Sci. U. S. A.* **2013**, *110*, 1187–1192.

[11] Bayly, P. V.; Lewis, B. L.; Ranz, E. C.; Okamoto, R. J.; Pless, R. B.; Dutcher, S. K. Propulsive forces on the flagellum during locomotion of chlamydomonas reinhardtii. *Biophys. J.* **2011**, *100*, 2716–2725.

[12] Wu, H.; Thiébaud, M.; Hu, W. F.; Farutin, A.; Rafaï, S.; Lai, M. C.; Peyla, P.; Misbah, C. Amoeboid motion in confined geometry. *Phys. Rev. E - Stat. Nonlinear, Soft Matter Phys.* **2015**, *92*, 050701.

[13] Poon, W. C. K. From Clarkia to Escherichia and Janus: the physics of natural and synthetic active colloids. *Soft Condens. Matter* **2013**, 317–386.

[14] Bastos-Arrieta, J.; Revilla-Guarinos, A.; Uspal, W. E.; Simmchen, J. Bacterial biohybrid microswimmers. *Frontiers in Robotics and AI* **2018**, *5*, 97.

[15] Kaynak, M.; Ozcelik, A.; Nourhani, A.; Lammert, P. E.; Crespi, V. H.; Huang, T. J. Acoustic actuation of bioinspired microswimmers. *Lab Chip* **2017**, *17*, 395–400.

[16] Kroy, K.; Chakraborty, D.; Cichos, F. Hot microswimmers. *Eur. Phys. J. Spec. Top.* **2016**, *225*, 2207–2225.

[17] Golestanian, R. Collective behavior of thermally active colloids. *Phys. Rev. Lett.* **2012**, *108*, 1–5.

[18] Schmidt, F.; Liebchen, B.; Löwen, H.; Volpe, G. Light-controlled assembly of active colloidal molecules. *J. Chem. Phys.* **2019**, *150*, 094905.

[19] Yang, M.; Ripoll, M. Thermophoretically induced flow field around a colloidal particle. *Soft Matter* **2013**, *9*, 4661–4671.

[20] Qian, B.; Montiel, D.; Bregulla, A.; Cichos, F.; Yang, H. Harnessing thermal fluctuations for purposeful activities: The manipulation of single microswimmers by adaptive photon nudging. *Chem. Sci.* **2013**, *4*, 1420–1429.

[21] Gomez-Solano, J. R.; Blokhuis, A.; Bechinger, C. Dynamics of Self-Propelled Janus Particles in Viscoelastic Fluids. *Phys. Rev. Lett.* **2016**, *116*, 1–5.

[22] Bregulla, A.; Yang, H.; Cichos, F. Stochastic localization of particles by photon nudging. *ACS Nano* **2014**, *8*, 6542–6550.

[23] Kline, T. R.; Paxton, W. F.; Mallouk, T. E.; Sen, A. Catalytic nanomotors: Remote-controlled autonomous movement of striped metallic nanorods. *Angew. Chemie - Int. Ed.* **2005**, *44*, 744–746.

[24] Feldmann, D.; Maduar, S. R.; Santer, M.; Lomadze, N.; Vinogradova, O. I.; Santer, S. Manipulation of small particles at solid liquid interface: light driven diffusioosmosis. *Sci. Rep.* **2016**, *6*, 36443.

[25] Parmar, J.; Vilela, D.; Sanchez, S. Tubular microjets: Fabrication, factors affecting the motion and mechanism of propulsion. *Eur. Phys. J. Spec. Top.* **2016**, *225*, 2255–2267.

[26] Grzybowski, B. A.; Stone, H. A.; Whitesides, G. M. Dynamic self-assembly of magnetized, millimetre-sized objects rotating at a liquid-air interface. *Nature* **2000**, *405*, 1033–1036.

[27] Tierno, P.; Golestanian, R.; Pagonabarraga, I.; Sagués, F. Controlled swimming in confined fluids of magnetically actuated colloidal rotors. *Phys. Rev. Lett.* **2008**, *101*, 218304.

[28] Baraban, L.; Tasinkevych, M.; Popescu, M. N.; Sanchez, S.; Dietrich, S.; Schmidt, O. G. Transport of cargo by catalytic Janus micro-motors. *Soft Matter* **2012**, *8*, 48–52.

[29] Xu, H.; Medina-Sánchez, M.; Magdanz, V.; Schwarz, L.; Hebenstreit, F.; Schmidt, O. G. Sperm-Hybrid Micromotor for Targeted Drug Delivery. *ACS Nano* **2018**, *12*, 327–337.

[30] Wang, B.; Kuo, J.; Granick, S. Bursts of active transport in living cells. *Phys. Rev. Lett.* **2013**, *111*, 1–5.

[31] Guix, M.; Mayorga-Martinez, C. C.; Merkoçi, A. Nano/micromotors in (bio) chemical science applications. *Chemical reviews* **2014**, *114*, 6285–6322.

[32] Wang, J.; Gao, W. Nano/microscale motors: biomedical opportunities and challenges. *ACS nano* **2012**, *6*, 5745–5751.

[33] Sengupta, S.; Ibele, M. E.; Sen, A. Fantastic voyage: designing self-powered nanorobots. *Angewandte Chemie International Edition* **2012**, *51*, 8434–8445.

[34] Kong, L.; Guan, J.; Pumera, M. Micro-and nanorobots based sensing and biosensing. *Current Opinion in Electrochemistry* **2018**, *10*, 174–182.

[35] Zarei, M.; Zarei, M. Self-Propelled Micro/Nanomotors for Sensing and Environmental Remediation. *Small* **2018**, *14*, 1800912.

[36] Brown, A.; Poon, W. Ionic effects in self-propelled Pt-coated Janus swimmers. *Soft Matter* **2014**, *10*, 4016–4027.

[37] Simmchen, J.; Katuri, J.; Uspal, W. E.; Popescu, M. N.; Tasinkevych, M.; Sánchez, S. Topographical pathways guide chemical microswimmers. *Nat. Commun.* **2016**, *7*, 1–9.

[38] Popescu, M. N.; Uspal, W. E.; Dietrich, S. Self-diffusiophoresis of chemically active colloids. *Eur. Phys. J. Spec. Top.* **2016**, *225*, 2189–2206.

[39] Lozano, C.; Ten Hagen, B.; Löwen, H.; Bechinger, C. Phototaxis of synthetic microswimmers in optical landscapes. *Nat. Commun.* **2016**, *7*, 1–10.

[40] Schachoff, R.; Selmke, M.; Bregulla, A.; Cichos, F.; Rings, D.; Chakraborty, D.; Kroy, K.; Günther, K.; Henning-Knechtel, A.; E., S.; Mertig, M. Hot Brownian motion and photophoretic self-propulsion. *Diffusion-Fundamentals.Org* **2015**, *23*, 1–19.

[41] Braun, M.; Bregulla, A. P.; Günther, K.; Mertig, M.; Cichos, F. Single Molecules Trapped by Dynamic Inhomogeneous Temperature Fields. *Nano Lett.* **2015**, *15*, 5499–5505.

[42] Muiños-Landin, S.; Fischer, A.; Holubec, V.; Cichos, F. Reinforcement learning with artificial microswimmers. *Science Robotics* **2021**, *6*.

[43] Morthomas, J.; Würger, A. Thermophoresis at a charged surface: The role of hydrodynamic slip. *J. Phys. Condens. Matter* **2009**, *21*, 1–4.

[44] Balasubramanian, S.; Kagan, D.; Jack Hu, C. M.; Campuzano, S.; Lobo-Castañon, M. J.; Lim, N.; Kang, D. Y.; Zimmerman, M.; Zhang, L.; Wang, J. Micromachine-enabled capture and isolation of cancer cells in complex media. *Angew. Chemie - Int. Ed.* **2011**, *50*, 4161–4164.

[45] Solovev, A. A.; Mei, Y.; Bermúdez Ureña, E.; Huang, G.; Schmidt, O. G. Catalytic Microtubular Jet Engines Self-Propelled by Accumulated Gas Bubbles. *Small* **2009**, *5*, 1688–1692.

[46] Alapan, Y.; Yasa, O.; Schauer, O.; Giltinan, J.; Tabak, A. F.; Sourjik, V.; Sitti, M. Soft erythrocyte-based bacterial microswimmers for cargo delivery. *Science Robotics* **2018**, *3*.

[47] Ricotti, L.; Trimmer, B.; Feinberg, A. W.; Raman, R.; Parker, K. K.; Bashir, R.; Sitti, M.; Martel, S.; Dario, P.; Menciassi, A. Biohybrid actuators for robotics: A review of devices actuated by living cells. *Science Robotics* **2017**, *2*.

[48] Xu, T.; Soto, F.; Gao, W.; Dong, R.; Garcia-Gradilla, V.; Magaña, E.; Zhang, X.; Wang, J. Reversible swarming and separation of self-propelled chemically powered nanomotors under acoustic fields. *J. Am. Chem. Soc.* **2015**, *137*, 2163–2166.

[49] Aranson, I. S. Active colloids. *Uspekhi Fiz. Nauk* **2013**, *56*, 79–92.

[50] Lattuada, M.; Hatton, T. A. Synthesis, properties and applications of Janus nanoparticles. *Nano Today* **2011**, *6*, 286–308.

[51] Jiang, S.; Chen, Q.; Tripathy, M.; Luijten, E.; Schweizer, K. S.; Granick, S. Janus particle synthesis and assembly. *Adv. Mater.* **2010**, *22*, 1060–1071.

[52] Mozaffari, A.; Sharifi-Mood, N.; Koplik, J.; Maldarelli, C. Self-diffusiophoretic colloidal propulsion near a solid boundary. *Physics of Fluids* **2016**, *28*, 053107.

[53] Ibrahim, Y.; Liverpool, T. B. The dynamics of a self-phoretic Janus swimmer near a wall. *EPL* **2015**, *111*, 48008.

[54] Liu, C.; Zhou, C.; Wang, W.; Zhang, H. P. Bimetallic Microswimmers Speed Up in Confining Channels. *Phys. Rev. Lett.* **2016**, *117*, 198001.

[55] Howse, J. R.; Jones, R. A.; Ryan, A. J.; Gough, T.; Vafabakhsh, R.; Golestanian, R. Self-motile colloidal particles: from directed propulsion to random walk. *Physical review letters* **2007**, *99*, 048102.

[56] Bregulla, A. P.; Cichos, F. Size dependent efficiency of photophoretic swimmers. *Faraday Discuss.* **2015**, *184*, 381–391.

[57] Heidari, M.; Bregulla, A.; Landin, S. M.; Cichos, F.; Von Klitzing, R. Self-Propulsion of Janus Particles near a Brush-Functionalized Substrate. *Langmuir* **2020**, *36*, 7775–7780.

[58] Ebbens, S. J.; Howse, J. R. In pursuit of propulsion at the nanoscale. *Soft Matter* **2010**, *6*, 726–738.

[59] Paxton, W. F.; Kistler, K. C.; Olmeda, C. C.; Sen, A.; St. Angelo, S. K.; Cao, Y.; Mallouk, T. E.; Lammert, P. E.; Crespi, V. H. Catalytic nanomotors: autonomous movement of striped nanorods. *Journal of the American Chemical Society* **2004**, *126*, 13424–13431.

[60] Nourhani, A.; Crespi, V. H.; Lammert, P. E.; Borhan, A. Self-electrophoresis of spheroidal electrocatalytic swimmers. *Phys. Fluids* **2015**, *27*, 092002.

[61] Wang, Y.; Hernandez, R. M.; Bartlett, D. J.; Bingham, J. M.; Kline, T. R.; Sen, A.; Mallouk, T. E. Bipolar electrochemical mechanism for the propulsion of catalytic nanomotors in hydrogen peroxide solutions. *Langmuir* **2006**, *22*, 10451–10456.

[62] Wang, W.; Duan, W.; Ahmed, S.; Mallouk, T. E.; Sen, A. Small power: Autonomous nano-and micromotors propelled by self-generated gradients. *Nano Today* **2013**, *8*, 531–554.

[63] Buttinoni, I.; Volpe, G.; Kümmel, F.; Volpe, G.; Bechinger, C. Active Brownian motion tunable by light. *J. Phys. Condens. Matter* **2012**, *24*, 284129.

[64] Wang, S.; Wu, N. Selecting the swimming mechanisms of colloidal particles: Bubble propulsion versus self-diffusiophoresis. *Langmuir* **2014**, *30*, 3477–3486.

[65] Jiang, H. R.; Yoshinaga, N.; Sano, M. Active motion of a Janus particle by self-thermophoresis in a defocused laser beam. *Phys. Rev. Lett.* **2010**, *105*, 1–4.

[66] Gomez-Solano, J. R.; Bechinger, C. Transient dynamics of a colloidal particle driven through a viscoelastic fluid. *New Journal of Physics* **2015**, *17*, 103032.

[67] Bickel, T.; Majee, A.; Würger, A. Flow pattern in the vicinity of self-propelling hot Janus particles. *Physical Review E* **2013**, *88*, 012301.

[68] Uspal, W. E.; Popescu, M. N.; Dietrich, S.; Tasinkevych, M. Self-propulsion of a catalytically active particle near a planar wall: From reflection to sliding and hovering. *Soft Matter* **2015**, *11*, 434–438.

[69] Chiang, T. Y.; Velegol, D. Localized electroosmosis (LEO) induced by spherical colloidal motors. *Langmuir* **2014**, *30*, 2600–2607.

[70] Ketzetzi, S.; De Graaf, J.; Doherty, R. P.; Kraft, D. J. Slip Length Dependent Propulsion Speed of Catalytic Colloidal Swimmers near Walls. *Phys. Rev. Lett.* **2020**, *124*.

[71] Jalilvand, Z.; Pawar, A. B.; Kretzschmar, I. Experimental study of the motion of patchy particle swimmers near a wall. *Langmuir* **2018**, *34*, 15593–15599.

[72] Wei, M.; Zhou, C.; Tang, J.; Wang, W. Catalytic Micromotors Moving Near Polyelectrolyte-Modified Substrates: The Roles of Surface Charges, Morphology, and Released Ions. *ACS Appl. Mater. Interfaces* **2018**, *10*, 2249–2252.

[73] Popescu, M. N.; Dietrich, S.; Oshanin, G. Confinement effects on diffusiophoretic self-propellers. *J. Chem. Phys.* **2009**, *130*.

[74] Das, S.; Garg, A.; Campbell, A. I.; Howse, J.; Sen, A.; Velegol, D.; Golestanian, R.; Ebbens, S. J. Boundaries can steer active Janus spheres. *Nat. Commun.* **2015**, *6*, 1–10.

[75] Bregulla, A. P.; Würger, A.; Günther, K.; Mertig, M.; Cichos, F. Thermo-Osmotic Flow in Thin Films. *Phys. Rev. Lett.* **2016**, *116*, 1–5.

[76] S.T.Milner, Polymer Brushes. *Science (80-.)*. **1991**, *251*, 905–914.

[77] Christau, S.; Thurandt, S.; Yenice, Z.; von Klitzing, R. Stimuli-responsive polyelectrolyte brushes as a matrix for the attachment of gold nanoparticles: The effect of brush thickness on particle distribution. *Polymers (Basel)*. **2014**, *6*, 1877–1896.

[78] Yang, W. J.; Neoh, K. G.; Kang, E. T.; Teo, S. L. M.; Rittschof, D. Polymer brush coatings for combating marine biofouling. *Prog. Polym. Sci.* **2014**, *39*, 1017–1042.

[79] Meng Chen, Wuge H. Briscoe, Steven P. Armes, J. K. Lubrication at physiological pressures by polyzwitterionic brushes. *Science (80-.)*. **2009**, *323*, 1698–1701.

[80] Chen, Q. Enhanced fluid flow through nanopores by polymer brushes. *Langmuir* **2014**, *30*, 8119–8123.

[81] Charrault, E.; Lee, T.; Easton, C. D.; Neto, C. Boundary flow on end-grafted PEG brushes. *Soft Matter* **2016**, *12*, 1906–1914.

[82] Wong, I.; Ho, C.-M. Surface molecular property modifications for poly (dimethylsiloxane)(PDMS) based microfluidic devices. *Microfluidics and nanofluidics* **2009**, *7*, 291.

[83] Ma, S.; Zhang, X.; Yu, B.; Zhou, F. Brushing up functional materials. *NPG Asia Mater.* **2019**, 1–39.

[84] De Groot, S. R.; Mazur, P. *Non-equilibrium thermodynamics*; Courier Corporation, 2013.

[85] Einstein, A. Über die von der molekularkinetischen Theorie der Wärme geforderte Bewegung von in ruhenden Flüssigkeiten suspendierten Teilchen. *Ann. Phys.* **1905**, *322*, 549–560.

[86] Brown, R. A brief account of microscopical observations made in the months of June, July and August 1827, on the particles contained in the pollen of plants; and on the general existence of active molecules in organic and inorganic bodies. *Philos. Mag.* **1828**, *4*, 161–173.

[87] Felderhof, B. Diffusion of interacting Brownian particles. *Journal of Physics A: Mathematical and General* **1978**, *11*, 929.

[88] Elgeti, J.; Winkler, R. G.; Gompper, G. Physics of microswimmersâsingle particle motion and collective behavior: a review. *Reports on progress in physics* **2015**, *78*, 056601.

[89] Toschi, F.; Sega, M. *Flowing Matter*; Springer Nature, 2019.

[90] Purcell, E. M. Life at low Reynolds number. *Am. J. Phys.* **1977**, *45*, 3–11.

[91] Najafi, A.; Golestanian, R. Simple swimmer at low Reynolds number: Three linked spheres. *Physical Review E* **2004**, *69*, 062901.

[92] Poon, W. From Clarkia to Escherichia and Janus: The physics of natural and synthetic active colloids. *Proc. Int. Sch. Phys. Enrico Fermi* **2013**, *184*, 317–386.

[93] Volpe, G.; Gigan, S.; Volpe, G. Simulation of the active Brownian motion of a microswimmer. *American Journal of Physics* **2014**, *82*, 659–664.

[94] Vutukuri, H. R.; Bet, B.; Van Roij, R.; Dijkstra, M.; Huck, W. T. Rational design and dynamics of self-propelled colloidal bead chains: from rotators to flagella. *Scientific reports* **2017**, *7*, 1–14.

[95] Anderson, J. L. Colloid Transport by Interfacial Forces. *Annu. Rev. Fluid Mech.* **1989**, *21*, 61–99.

[96] Platten, J. K. The Soret effect: a review of recent experimental results. **2006**,

[97] Piazza, R.; Parola, A. Thermophoresis in colloidal suspensions. *J. Phys. Condens. Matter* **2008**, *20*, 153102.

[98] Würger, A. Thermal non-equilibrium transport in colloids. *Reports Prog. Phys.* **2010**, *73*, 1–35.

[99] Gompper, G.; Bechinger, C.; Herminghaus, S.; Isele-Holder, R.; Kaupp, B.; Stark, H.; Winkler, R. *Microswimmers-From Single Particle Motion to Collective Behavior*; Schlüsseltechnologien/Key Technologies, 2015.

[100] Li, D. *Encyclopedia of microfluidics and nanofluidics*; Springer Science & Business Media, 2008.

[101] Stern, O. The theory of the electrolytic double-layer. *Z. Elektrochem* **1924**, *30*, 1014–1020.

[102] Peng, X.-H.; Qian, X.; Mao, H.; Wang, A. Y., et al. Targeted magnetic iron oxide nanoparticles for tumor imaging and therapy. *International journal of nanomedicine* **2008**, *3*, 311.

[103] Leary, S. P.; Liu, C. Y.; Apuzzo, M. Toward the emergence of nanoneurosurgery: part III–nanomedicine: targeted nanotherapy, nanosurgery, and progress toward the realization of nanoneurosurgery. *Neurosurgery* **2006**, *58*, 1009–26.

[104] Lee, S. H.; Jun, B.-H. Silver nanoparticles: synthesis and application for nanomedicine. *International journal of molecular sciences* **2019**, *20*, 865.

[105] Chen, H.; Zhen, Z.; Todd, T.; Chu, P. K.; Xie, J. Nanoparticles for improving cancer diagnosis. *Materials Science and Engineering: R: Reports* **2013**, *74*, 35–69.

[106] Brongersma, M. L.; Kik, P. G. *Surface plasmon nanophotonics*; Springer, 2007; Vol. 131.

[107] García, M. A. Surface plasmons in metallic nanoparticles: fundamentals and applications. *Journal of Physics D: Applied Physics* **2011**, *44*, 283001.

[108] Matyjaszewski, K.; Miller, P. J.; Shukla, N.; Immaraporn, B.; Gelman, A.; Luokala, B. B.; Siclovan, T. M.; Kickelbick, G.; Valiant, T.; Hoffmann, H.; Pakula, T. Polymers at interfaces: Using atom transfer radical polymerization in the controlled growth of homopolymers and block copolymers from silicon surfaces in the absence of untethered sacrificial initiator. *Macromolecules* **1999**, *32*, 8716–8724.

[109] A structural definition of polymer brushes. *J. Polym. Sci. Part A Polym. Chem.* **2007**, *45*, 3505–3512.

[110] Brittain, W. J.; Minko, S. A structural definition of polymer brushes. *Journal of Polymer Science Part A: Polymer Chemistry* **2007**, *45*, 3505–3512.

[111] Ataman, N. C.; Klok, H.-A. Degrafting of Poly (poly (ethylene glycol) methacrylate) Brushes from Planar and Spherical Silicon Substrates. *Macromolecules* **2016**, *49*, 9035–9047.

[112] Lilge, I. *Polymer Brush Films with Varied Grafting and Cross-Linking Density via SI-ATRP*; Springer, 2017; pp 27–36.

[113] Zoppe, J. O.; Ataman, N. C.; Mocny, P.; Wang, J.; Moraes, J.; Klok, H.-A. Surface-initiated controlled radical polymerization: state-of-the-art, opportunities, and challenges in surface and interface engineering with polymer brushes. *Chemical reviews* **2017**, *117*, 1105–1318.

[114] Harutyunyan, H.; Palomba, S.; Renger, J.; Quidant, R.; Novotny, L. Nonlinear dark-field microscopy. *Nano letters* **2010**, *10*, 5076–5079.

[115] Pedrotti, L. S. Basic geometrical optics. *Fundamentals of photonics* **2008**, 73–116.

[116] Taylor, S. A., et al. CCD and CMOS imaging array technologies: technology review. *UK: Xerox Research Centre Europe* **1998**, 1–14.

[117] Litwiller, D. Ccd vs. cmos. *Photonics spectra* **2001**, *35*, 154–158.

[118] Dunderdale, G.; Ebbens, S.; Fairclough, P.; Howse, J. Importance of particle tracking and calculating the mean-squared displacement in distinguishing nanopropulsion from other processes. *Langmuir* **2012**, *28*, 10997–11006.

[119] Laurent, P.; Souharce, G.; Duchet-Rumeau, J.; Portinha, D.; Charlot, A. 'Pancake' vs. brush-like regime of quaternizable polymer grafts: An efficient tool for nano-templating polyelectrolyte self-assembly. *Soft Matter* **2012**, *8*, 715–725.

[120] Fujie, T.; Park, J. Y.; Murata, A.; Estillore, N. C.; Tria, M. C. R.; Takeoka, S.; Advincula, R. C. Hydrodynamic transformation of a freestanding polymer nanosheet induced by a thermoresponsive surface. *ACS Appl. Mater. Interfaces* **2009**, *1*, 1404–1413.

[121] Zhuang, P.; Dirani, A.; Glinel, K.; Jonas, A. M. Temperature Dependence of the Surface and Volume Hydrophilicity of Hydrophilic Polymer Brushes. *Langmuir* **2016**, *32*, 3433–3444.

[122] Fang, Y.; Xu, W.; Meng, X. L.; Ye, X. Y.; Wu, J.; Xu, Z. K. Poly(2-hydroxyethyl methacrylate) brush surface for specific and oriented adsorption of glycosidases. *Langmuir* **2012**, *28*, 13318–13324.

[123] Tompkins, H.; Irene, E. A. *Handbook of ellipsometry*; William Andrew, 2005.

[124] Theeten, J. B.; Aspnes, D. E. Ellipsometry in Thin Film Analysis. *Annu. Rev. Mater. Sci.* **1981**, *11*, 97–122.

[125] Garcıa, R.; Perez, R. Dynamic atomic force microscopy methods. *Surface science reports* **2002**, *47*, 197–301.

[126] Deng, X. R.; Qian, Z. Y.; Zhou, Z. C. The Colloidal Probe Technique and its Application to Adhesion Force Measurements. *Part. Part. Syst. Charact.* **2002**, *19*, 129–143.

[127] Tolan, M.; Tolan, M. *X-ray scattering from soft-matter thin films: materials science and basic research*; Springer, 1999; Vol. 148.

[128] Clogston, J. D.; Patri, A. K. *Characterization of nanoparticles intended for drug delivery*; Springer, 2011; pp 63–70.

[129] Young, T. An essay on the cohesion of fluids. *Philos. Trans. R. Soc. London* **1805**, *95*, 65–87.

[130] Tanmay Ghonge, R. D., Jeevanjyoti Chakraborty; Chakraborty, S. Electrohydrodynamics within the electrical double layer in the presence of finite temperature gradients. *Phys. Rev. E* **2013**, *88*, 1–13.

[131] Lützenkirchen, J.; Zimmermann, R.; Preočanin, T.; Filby, A.; Kupcik, T.; Küttner, D.; Abdelmonem, A.; Schild, D.; Rabung, T.; Plaschke, M., et al. An attempt to explain bimodal behaviour of the sapphire c-plane electrolyte interface. *Advances in colloid and interface science* **2010**, *157*, 61–74.

[132] Kaper, H. J.; Busscher, H. J.; Norde, W. Journal of Biomaterials Science , Polymer Edition Characterization of poly (ethylene oxide) brushes on glass surfaces and adhesion of Staphylococcus epidermidis. *J. Biomater. Sci. Polym. Ed.* **2003**, *14*, 313–324.

[133] Breite, D.; Went, M.; Prager, A.; Schulze, A. The critical zeta potential of polymer membranes: How electrolytes impact membrane fouling. *RSC Adv.* **2016**, *6*, 98180–98189.

[134] Ebbens, S.; Tu, M. H.; Howse, J. R.; Golestanian, R. Size dependence of the propulsion velocity for catalytic Janus-sphere swimmers. *Phys. Rev. E - Stat. Nonlinear, Soft Matter Phys.* **2012**, *85*, 20401.

[135] Theers, M.; Westphal, E.; Qi, K.; Winkler, R. G.; Gompper, G. Clustering of microswimmers: Interplay of shape and hydrodynamics. *Soft Matter* **2018**, *14*, 8590–8603.

[136] Wheat, P. M.; Marine, N. A.; Moran, J. L.; Posner, J. D. Rapid fabrication of bimetallic spherical motors. *Langmuir* **2010**, *26*, 13052–13055.

[137] Jalilvand, Z.; Pawar, A. B.; Kretzschmar, I. Experimental Study of the Motion of Patchy Particle Swimmers Near a Wall. *Langmuir* **2018**, *34*, 15593–15599.

[138] Holterhoff, A. L.; Li, M.; Gibbs, J. G. Self-Phoretic Microswimmers Propel at Speeds Dependent upon an Adjacent Surface's Physicochemical Properties. *J. Phys. Chem. Lett.* **2018**, *9*, 5023–5028.

[139] Ye, Q.; Zhao, W.; Yang, W.; Pei, X.; Zhou, F. Grafting Binary PEG and Fluoropolymer Brushes from Mix-Biomimic Initiator as "Ambiguous" Surfaces for Antibiofouling. *Macromol. Chem. Phys.* **2017**, *218*.

[140] Gunkel-Grabole, G.; Car, A.; Naik, V. V.; Marot, L.; Ferk, G.; Palivan, C.; Meier, W. PEG Brushes on Porous, PDMS-Coated Surfaces and Their Interaction with Carbon Dioxide. *Macromol. Chem. Phys.* **2016**, *217*, 966–973.

[141] Cras, J. J.; Rowe-Taitt, C. A.; Nivens, D. A.; Ligler, F. S. Comparison of chemical cleaning methods of glass in preparation for silanization. *Biosens. Bioelectron.* **1999**, *14*, 683–688.

[142] Lou, S.-T.; Ouyang, Z.-Q.; Zhang, Y.; Li, X.-J.; Hu, J.; Li, M.-Q.; Yang, F.-J. Nanobubbles on solid surface imaged by atomic force microscopy. *J. Chem. Phys.* **2000**, *18*, 14706.

[143] Poynor, A.; Hong, L.; Robinson, I. K.; Granick, S.; Zhang, Z.; Fenter, P. A. How water meets a hydrophobic surface. *Phys. Rev. Lett.* **2006**, *97*.

[144] Steitz, R.; Gutberlet, T.; Hauss, T.; Klösgen, B.; Krastev, R.; Schemmel, S.; Simonsen, A. C.; Findenegg, G. H. Nanobubbles and their precursor layer at the interface of water against a hydrophobic substrate. *Langmuir* **2003**, *19*, 2409–2418.

[145] Shangjiong, Y.; Dammer, S. M.; Bremond, N.; Zandvliet, H. J.; Kooij, E. S.; Lohse, D. Characterization of nanobubbles on hydrophobic surfaces in water. *Langmuir* **2007**, *23*, 7072–7077.

[146] Arieli, R. Nanobubbles Form at Active Hydrophobic Spots on the Luminal Aspect of Blood Vessels: Consequences for Decompression Illness in Diving and Possible Implications for Autoimmune Disease-An Overview. *Front. Physiol.* **2017**, *8*, 591.

[147] Yang, J.; Duan, J.; Fornasiero, D.; Ralston, J. Very small bubble formation at the solid-water interface. *J. Phys. Chem. B* **2003**, *107*, 6139–6147.

[148] Wang, Y.; Bhushan, B. Boundary slip and nanobubble study in micro/nanofluidics using atomic force microscopy. *Soft Matter* **2010**, *6*, 29–66.

[149] Shen, Z.; Würger, A.; Lintuvuori, J. S. Hydrodynamic interaction of a self-propelling particle with a wall. *The European Physical Journal E* **2018**, *41*, 1–9.

[150] Crowdy, D. G. Wall effects on self-diffusiophoretic Janus particles: a theoretical study. *Journal of fluid mechanics* **2013**, *735*, 473.

[151] Brown, A.; Poon, W. Ionic effects in self-propelled Pt-coated Janus swimmers. *Soft matter* **2014**, *10*, 4016–4027.

[152] Balamurugan, S.; Mendez, S.; Balamurugan, S. S.; O'Brien, M. J.; López, G. P. Thermal response of poly (N-isopropylacrylamide) brushes probed by surface plasmon resonance. *Langmuir* **2003**, *19*, 2545–2549.

[153] Yim, H.; Kent, M. S.; Mendez, S.; Lopez, G. P.; Satija, S.; Seo, Y. Effects of grafting density and molecular weight on the temperature-dependent

conformational change of poly(N-isopropylacrylamide) grafted chains in water. *Macromolecules* **2006**, *39*, 3420–3426.

[154] Dharmasiri, M. B.; Mudiyanselage, T. K. Thermo-responsive poly (N-isopropyl acrylamide) hydrogel with increased response rate. *Polymer Bulletin* **2020**, 1–16.

[155] Idziak, I.; Avoce, D.; Lessard, D.; Gravel, D.; Zhu, X. Thermosensitivity of aqueous solutions of poly (N, N-diethylacrylamide). *Macromolecules* **1999**, *32*, 1260–1263.

[156] Milner, S. T.; Witten, T. A.; Cates, M. E. Theory of the grafted polymer brush. *Macromolecules* **1988**, *21*, 2610–2619.

[157] Yu, Y.; Kieviet, B. D.; Liu, F.; Siretanu, I.; Kutnyánszky, E.; Vancso, G. J.; de Beer, S. Stretching of collapsed polymers causes an enhanced dissipative response of PNIPAM brushes near their LCST. *Soft Matter* **2015**, *11*, 8508–8516.

[158] Philipp, M.; Müller, U.; Aleksandrova, R.; Sanctuary, R.; Müller-Buschbaum, P.; Krüger, J. K. Immense elastic nonlinearities at the demixing transition of aqueous PNIPAM solutions. *Soft Matter* **2013**, *9*, 5034–5041.

[159] Wu, C.; Wang, X. Globule-to-coil transition of a single homopolymer chain in solution. *Physical review letters* **1998**, *80*, 4092.

[160] Graziano, G. On the temperature-induced coil to globule transition of poly-N-isopropylacrylamide in dilute aqueous solutions. *International journal of biological macromolecules* **2000**, *27*, 89–97.

[161] Wagner, M.; Brochard-Wyart, F.; Hervet, H.; de Gennes, P. G. Colloid & Polymer Science - Collapse of polymer brushes induced by n-clusters. *Colloid Polym. Sci.* **1993**, *271*, 621–628.

[162] Zhang, Z.; Morse, A. J.; Armes, S. P.; Lewis, A. L.; Geoghegan, M.; Leggett, G. J. Effect of brush thickness and solvent composition on the friction force response of poly(2-(methacryloyloxy)ethylphosphorylcholine) brushes. *Langmuir* **2011**, *27*, 2514–2521.

[163] Svetushkina, E.; Puretskiy, N.; Ionov, L.; Stamm, M.; Synytska, A. A comparative study on switchable adhesion between thermoresponsive polymer brushes on flat and rough surfaces. *Soft Matter* **2011**, *7*, 5691–5696.

[164] Pan, Y.; Bhushan, B. Role of surface charge on boundary slip in fluid flow. *J. Colloid Interface Sci.* **2013**, *392*, 117–121.

[165] Bevan, M. A.; Prieve, D. C. Hindered diffusion of colloidal particles very near to a wall. *J. Chem. Phys.* **2000**, *113*, 1228–1236.

[166] Kihm, K. D.; Banerjee, A.; Choi, C. K.; Takagi, T. Near-wall hindered Brownian diffusion of nanoparticles examined by three-dimensional ratiometric total internal reflection fluorescence microscopy (3-D R-TIRFM). *Exp. Fluids* **2004**, *37*, 811–824.

[167] Christau, S.; Möller, T.; Yenice, Z.; Genzer, J.; Von Klitzing, R. Brush/gold nanoparticle hybrids: Effect of grafting density on the particle uptake and distribution within weak polyelectrolyte brushes. *Langmuir* **2014**, *30*, 13033–13041.

[168] Gao, X.; Kučerka, N.; Nieh, M. P.; Katsaras, J.; Zhu, S.; Brash, J. L.; Sheardown, H. Chain conformation of a new class of PEG-based thermoresponsive polymer brushes grafted on silicon as determined by neutron reflectometry. *Langmuir* **2009**, *25*, 10271–10278.

[169] Bechinger, C.; Di Leonardo, R.; Löwen, H.; Reichhardt, C.; Volpe, G.; Volpe, G. Active particles in complex and crowded environments. *Rev. Mod. Phys.* **2016**, *88*, 045006(50).

[170] Schachoff, R.; Sperling, E.; Mertig, M.; Selmke, M.; Bregulla, A.; Cichos, F.; Rings, D.; Chakraborty, D.; Kroy, K.; Günther, K., et al. Hot Brownian motion and photophoretic self-propulsion. *diffusion-fundamentals.org* **2015**, 1–19.

[171] Watson, S.; Dennington, S.; Wang, L.; Nie, M.; Hinder, S.; Stokes, K. Polymer brush lubrication of the silicon nitride-steel contact: A colloidal force microscopy study. *RSC Adv.* **2017**, *7*, 42667–42676.

[172] Al-Jaf, O.; Alswieleh, A.; Armes, S. P.; Leggett, G. J. Nanotribological properties of nanostructured poly(cysteine methacrylate) brushes. *Soft Matter* **2017**, *13*, 2075–2084.

[173] Desseaux, S.; Hinestrosa, J. P.; Schüwer, N.; Lokitz, B. S.; Ankner, J. F.; Kilbey, S. M.; Voitchovsky, K.; Klok, H. A. Swelling behavior and nanomechanical properties of (peptide-modified) poly(2-hydroxyethyl methacrylate) and poly(poly(ethylene glycol) methacrylate) brushes. *Macromolecules* **2016**, *49*, 4609–4618.

[174] Attili, S.; Richter, R. P. Combining colloidal probe atomic force and reflection interference contrast microscopy to study the compressive mechanics of hyaluronan brushes. *Langmuir* **2012**, *28*, 3206–3216.

[175] Tranchida, D.; Sperotto, E.; Staedler, T.; Jiang, X.; Schönherr, H. Nanomechanical properties of oligo(ethylene glycol methacrylate) polymer brush-based biointerfaces. *Adv. Eng. Mater.* **2011**, *13*, B369–B376.

[176] Dehghani, E. S.; Spencer, N. D.; Ramakrishna, S. N.; Benetti, E. M. Crosslinking polymer brushes with ethylene glycol-containing segments: Influence on physicochemical and antifouling properties. *Langmuir* **2016**, *32*, 10317–10327.

[177] Stan, G.; Delrio, F. W.; MacCuspie, R. I.; Cook, R. F. Nanomechanical properties of polyethylene glycol brushes on gold substrates. *J. Phys. Chem. B* **2012**, *116*, 3138–3147.

[178] Bao, Z.; Bruening, M. L.; Baker, G. L. Control of the density of polymer brushes prepared by surface-initiated atom transfer radical polymerization. *Macromolecules* **2006**, *39*, 5251–5258.

[179] Psarra, E.; KoÌnig, U.; Ueda, Y.; Bellmann, C.; Janke, A.; Bittrich, E.; Eichhorn, K.-J.; Uhlmann, P. Nanostructured biointerfaces: nanoarchitectonics of thermoresponsive polymer brushes impact protein adsorption and cell adhesion. *ACS applied materials & interfaces* **2015**, *7*, 12516–12529.

[180] Zimmermann, R.; Dukhin, S.; Werner, C. Electrokinetic measurements reveal interracial charge at polymer films caused by simple electrolyte ions. *J. Phys. Chem. B* **2001**, *105*, 8544–8549.

[181] Pashley, R. M. Hydration forces between mica surfaces in aqueous electrolyte solutions. *J. Colloid Interface Sci.* **1981**, *80*, 153–162.

[182] Lützenkirchen, J. Specific ion effects at two single-crystal planes of sapphire. *Langmuir* **2013**, *29*, 7726–7734.

[183] Würger, A. Thermal non-equilibrium transport in colloids. *Reports on Progress in Physics* **2010**, *73*, 126601.

[184] Kroy, K.; Cichos, F. *Diffusive Spreading in Nature, Technology and Society*; Springer, 2018; pp 127–145.

[185] Ketzetzi, S.; de Graaf, J.; Kraft, D. J. Diffusion-based height analysis reveals robust microswimmer-wall separation. *Physical Review Letters* **2020**, *125*, 238001.

[186] Dalstein, L.; Potapova, E.; Tyrode, E. The elusive silica/water interface: Isolated silanols under water as revealed by vibrational sum frequency spectroscopy. *Physical Chemistry Chemical Physics* **2017**, *19*, 10343–10349.

[187] Yang, S. C.; Fang, L. B. Effect of surface roughness on slip flows in hydrophobic and hydrophilic microchannels by molecular dynamics simulation. *Mol. Simul.* **2005**, *31*, 971–977.

[188] Patil, R. R.; Turgman-Cohen, S.; Šrogl, J.; Kiserow, D.; Genzer, J. Direct measurement of molecular weight and grafting density by controlled and quantitative degrafting of surface-anchored poly(methyl methacrylate). *ACS Macro Lett.* **2015**, *4*, 251–254.

[189] Patil, R.; Miles, J.; Ko, Y.; Datta, P.; Rao, B. M.; Kiserow, D.; Genzer, J. Kinetic Study of Degrafting Poly(methyl methacrylate) Brushes from Flat Substrates by Tetrabutylammonium Fluoride. *Macromolecules* **2018**, *51*, 10237–10245.

[190] Melzak, K. A.; Yu, K.; Bo, D.; Kizhakkedathu, J. N.; Toca-Herrera, J. L. Chain Length and Grafting Density Dependent Enhancement in the Hydrolysis of Ester-Linked Polymer Brushes. *Langmuir* **2015**, *31*, 6463–6470.

[191] Ataman, N. C.; Klok, H. A. Degrafting of Poly(poly(ethylene glycol) methacrylate) Brushes from Planar and Spherical Silicon Substrates. *Macromolecules* **2016**, *49*, 9035–9047.

List of Symbols and Abbreviations

PHEMA	Poly(2-hydroxyethyl methacrylate)
BTPAm	2-bromo-2-methyl-N-(3-(triethoxysilyl)propyl)propanamide
BMPUS	2-bromo-2-methyl-N-(11-(trichlorosilyl)undecyl) propanamide
PNIPAM	Poly(N-isopropylacrylamide)
POEGMA	Poly(ethylene glycol) methyl ether mathacrylate
LCST	Lower solution critical temperature
ATRP	Atom transfer radical polymerization
AFM	Atomic force microscopy
XRR	X-ray reflectometry
MSD	Mean square displacement
λ	Wavelength
n	Refractive index
k	Absorption constant
Q_z	Momentum transfer
Δ	Phase shift
Ψ	Amplitude ratio
ρ	Brush grafting density
N_A	Avogadro number
M_n	Average polymer molecular weight
v_{th}	Thermophoretic velocity
D_{T}	Translational diffusion coefficient
D_{r}	Rotational diffusion coefficient

Scientific Publications

Publications as the first author

- Self-propulsion of Janus Particles near a PNIPAM-functionalized Substrate. Mojdeh Heidari, Andreas Bregulla, Santiago Muiños Landin, Frank Cichos, and Regine von Klitzing. **Langmuir** (2020), 36: 7775-7780
- Non-monotonous Speed-dependence of Microswimmers on Wall Distance. Mojdeh Heidari, Franziska Jakob, Benno Liebchen, Regine von Klitzing. *submitted*

Publications as the co-author

- Decoupling of Dynamic and Thermal Glass Transition in Thin Films of a PVME/PS Blend. Sherif Madkour, Paulina Szymoniak, Andreas Hertwig, Mojdeh Heidari, Regine von Klitzing, Simone Napolitano, Michelle Sferrazza and Andreas Schönhals. **ACS Macro Letters** (2017), 6(10):1156-1161.
- Unveiling the Dynamics of Self-Assembled Layers of Thin Films of PVME by Nanosized Relaxation Spectroscopy. Sherif Madkour, Paulina Szymoniak, Mojdeh Heidari, Regine von Klitzing, and Andreas Schönhals. **ACS Applied Materials Interfaces** (2017) 9(8): 7535-7546.

Scientific Career

03.2017-now	Research assistant at the institute of solid state physics at TU Darmstadt in the group of Prof. Dr. Regine von Klitzing
05.2014-02.2017	Research assistant at the chemistry institute at TU Berlin in the group of Prof. Dr. Regine von Klitzing
10.2011-12.2013	Polymer Science (M. Sc.), joint program at TU, FU, HU, and UP in Berlin
	Thesis: Evaluation of polyether networks as drug depots for long term release systems
09.2006-09.2010	Textile Engineering (B. Sc.) at Isfahan University of Technology
	Thesis: Study on how to remove Phaomelanin which exists in Protein fibers